Spaceborne Microwave Instrument for High Resolution Remote Sensing of the Earth's Surface Using a Large-Aperture Mesh Antenna

E. Njoku, W. Wilson, S. Yueh, R. Freeland, R. Helms, W. Edelstein,
G. Sadowy, D. Farra, R. West, K. Oxnevad
Jet Propulsion Laboratory, California Institute of Technology
Pasadena, California

T. Campbell, W. Lawrence
NASA Langley Research Center, Hampton, Virginia

Y. Rahmat-Samii
University of California, Los Angeles, California

H. Feingold, G. Didinsky, J. Rauwolf
Science Applications International Corporation, Schaumburg, Illinois

M. Thomson
TRW Astro Aerospace, Carpinteria, California

G. Konicke
Spectrum Astro, Inc., Gilbert, Arizona

September 2001

ABSTRACT

This report describes a two-year study of a large-aperture, lightweight, deployable mesh antenna system for radiometer and radar remote sensing of the Earth from space. The study focused specifically on an instrument to measure ocean salinity and soil moisture. Measurements of ocean salinity and soil moisture are of critical importance in improving knowledge and prediction of key ocean and land surface processes, but are not currently obtainable from space. A mission using this instrument would be the first demonstration of deployable mesh antenna technology for remote sensing and could lead to potential applications in other remote sensing disciplines that require high spatial resolution measurements. The study concept features a rotating 6-m-diameter deployable-mesh antenna, with radiometer and radar sensors, to measure microwave emission and backscatter from the Earth's surface. The sensors operate at L and S bands, with multiple polarizations and a constant look angle, scanning across a wide swath. The study included detailed analyses of science requirements, reflector and feedhorn design and performance, microwave emissivity measurements of mesh samples, design and test of lightweight radar electronics, launch vehicle accommodations, rotational dynamics simulations, and an analysis of attitude control issues associated with the antenna and spacecraft. The goal of the study was to advance the technology readiness of the overall concept to a level appropriate for an Earth science mission.

The study was performed by the Jet Propulsion Laboratory and the NASA Langley Research Center, with participation by the University of California Los Angeles, Science Applications International Corporation, TRW Astro Aerospace, and Spectrum Astro, Inc. The study was sponsored by the NASA Earth Science Technology Office (ESTO) Instrument Incubator Program (IIP).

ACKNOWLEDGMENTS

CONTENTS

CONTENTS (Continued)

CONTENTS (Continued)

ILLUSTRATIONS

ILLUSTRATIONS (Continued)

ILLUSTRATIONS (Continued)

TABLES

xi

TABLES (Continued)

1. SUMMARY

1.1 RATIONALE

1.1.1 Motivation

This study addressed key technology issues related to the utilization of large aperture, lightweight, deployable mesh antennas for microwave remote sensing of the Earth from space. Recent advances in the design and construction of such antennas, and their history of successful operation in space telecommunications, have opened up potential new applications for high-resolution microwave Earth sensing. However, significant challenges exist in implementing these antennas for remote sensing applications. The primary applications are in ocean salinity and soil moisture measurement. Measurements of these parameters require large antennas, and cannot adequately be made from space using current systems. The overall objectives of this study were: (1) to investigate the feasibility and advance the technology readiness of deployable mesh antennas for ocean salinity and soil moisture sensing, and (2) to assess the potential of mesh antenna technology for other remote sensing measurements. Results of this study will be applicable to development of ocean salinity and/or soil moisture measurement missions that require large-aperture deployable antennas.

Ocean salinity and soil moisture measurements are needed to improve our understanding of and capability to predict key ocean and land surface processes, but no spaceborne measurements of these parameters currently exist. The science motivation for this study arose from a series of workshops conducted by NASA during 1998–99 to develop a strategy for its Earth Science Enterprise science missions in the post-2002 era. These workshops, and subsequent reviews, culminated in publication of NASA's Earth Science Enterprise (ESE) Strategic Plan (NASA, 2000). In this strategy, ocean salinity and soil moisture were identified as high priority measurements.

Previous studies have indicated that the best approach for remote measurement of ocean salinity and soil moisture is microwave sensing at low frequency (1–3 GHz) (Lagerloef et al., 1995; Njoku and Entekhabi, 1996). At low frequencies large antennas are needed to achieve adequate spatial resolution from Earth orbit. Deployable mesh reflectors are an attractive option for large antennas since they are lightweight, can be stowed compactly for launch, and can provide excellent antenna RF performance characteristics at low microwave frequency. Recent large antenna technology development has been driven primarily by the satellite telecommunications industry. However, these antennas have also been considered for remote sensing instruments. One such instrument was proposed for the Navy NROSS mission in the early 1980s. This instrument, the Low Frequency Microwave Radiometer (LFMR), utilized a 6-meter deployable antenna (Figure 1.1-1); the mission was later cancelled due to budgetary concerns. In relation to this mission and a general interest in the potential of large antennas for remote sensing, studies of these antennas were carried out for many years at the NASA Langley Research Center (Schroeder et al., 1994). Renewed interest in deployable mesh antennas has arisen in recent years as their maturity, mass, and cost have become acceptable for consideration in low-cost science missions.

1
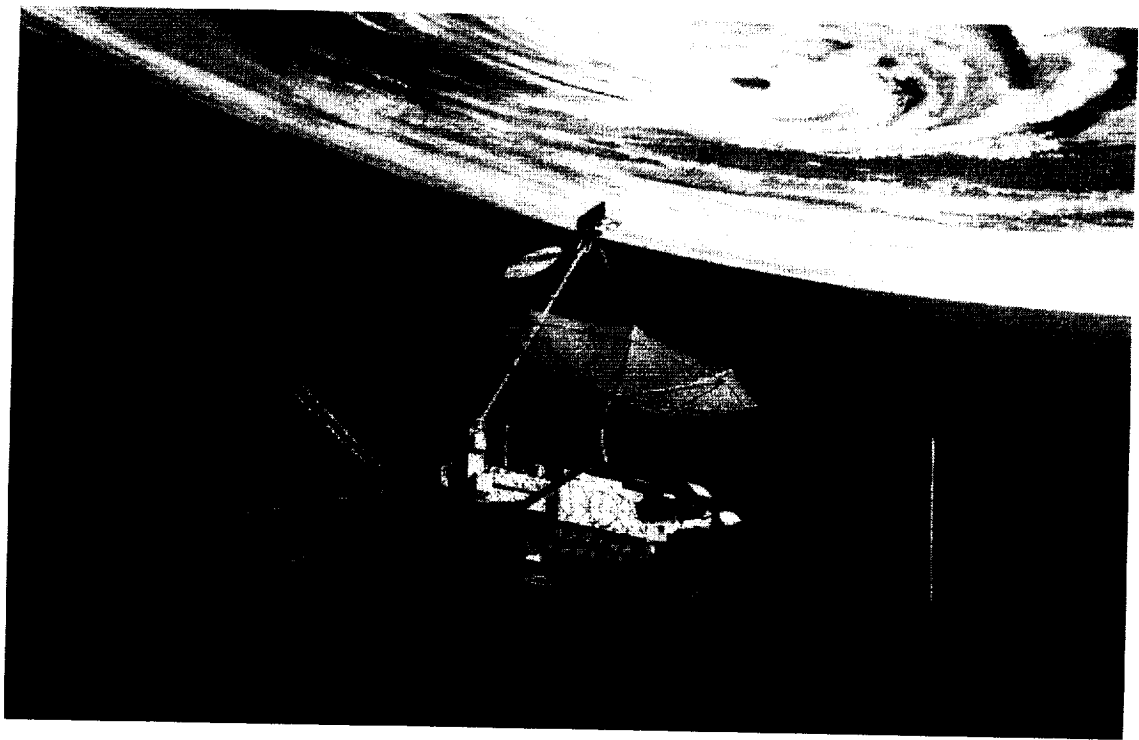
Figure 1.1-1. The NROSS mission concept.

1.1.2 Baseline System—OSIRIS

The baseline concept studied here is named the Ocean-salinity Soil-moisture Integrated Radiometer-radar Imaging System (OSIRIS) and is illustrated in Figure 1.1-2. The OSIRIS concept combines passive and active (real-aperture) sensing in the 1–3 GHz range, using a 6-m-diameter, lightweight, deployable mesh antenna. The antenna system consists of a rotating, offset-fed parabolic reflector with two multichannel feedhorns shared by radiometer and radar subsystems in one sensor package. The system measures microwave emission and backscatter from the Earth's surface at a fixed incidence angle, scanning conically across a wide swath at multiple frequencies and polarizations. The key technology in the system is the lightweight mesh deployable antenna. The reflector surface is a tensioned gold-plated molybdenum wire mesh supported by a mesh/net or cable system which in turn is supported by rigid ribs or a perimeter truss structure that can be folded compactly for launch and deployed on orbit. Large antennas of this construction, at sizes up to ~12 m, have been developed and launched successfully in the commercial sector (Miller, 1998). Their use for remote sensing requires careful study due to the unique requirements for radiometric precision and accuracy, and the demands on spacecraft attitude control imposed by large rotating antennas.

The rationale for considering combined passive and active sensors is that complementary information contained in the surface emissivity and backscattering signatures can provide enhanced accuracy in the retrieval of geophysical parameters. Over the ocean, passive (radiometric) measurements provide the primary information for estimating sea surface salinity (SSS) and sea surface temperature (SST) and can also provide information on wind-induced

2
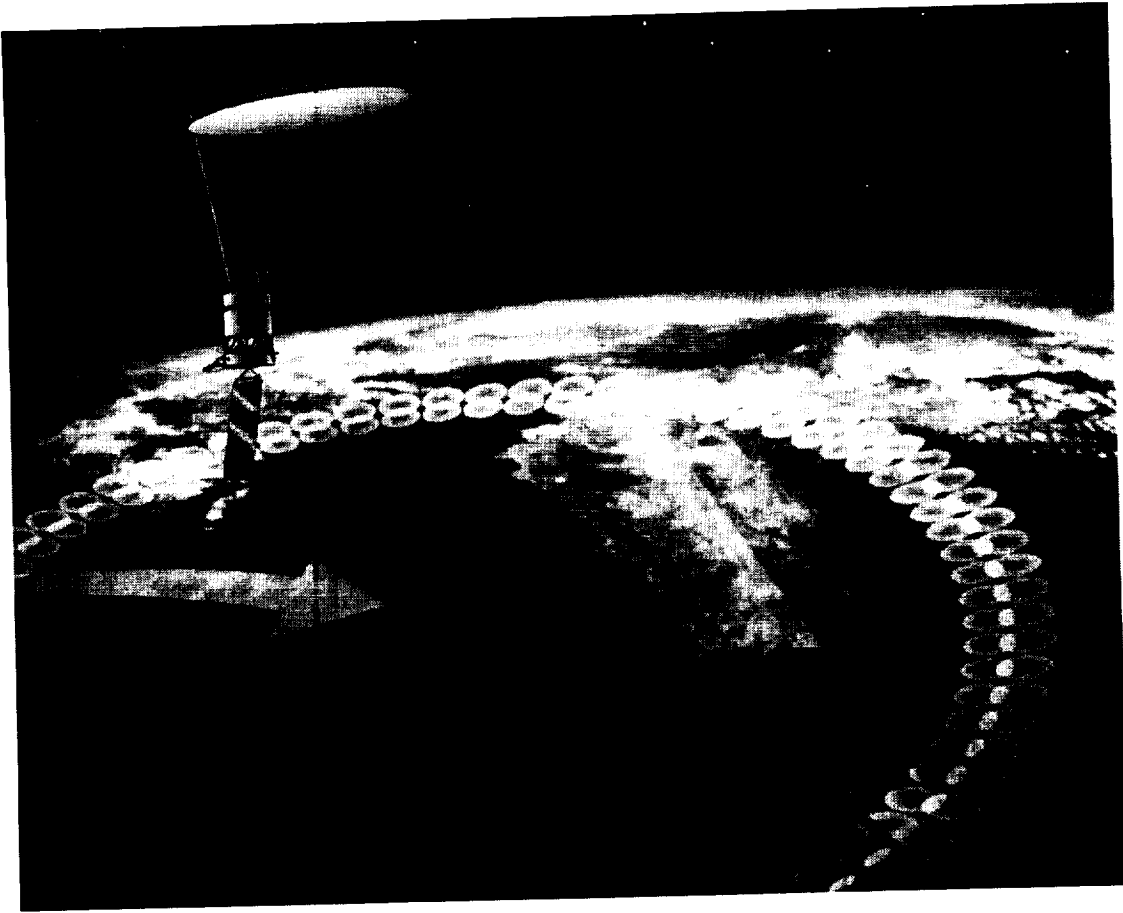
Figure 1.1-2. OSIRIS concept showing the offset-fed parabolic mesh reflector antenna and the footprint scan pattern at the surface. Two antenna beams are provided using identical dual feedhorns, allowing the reflector to spin at moderate rate while providing full mapping coverage.

surface roughness. Active (scatterometer) measurements provide primary information on wind-induced surface roughness, augmenting the radiometric measurements. Over land, radiometric measurements provide the primary information for estimating soil moisture, while scatterometer measurements are an additional source of information on surface roughness and vegetation. The simulations described in Section 3 indicate that a 6-m-antenna radiometer-scatterometer system is capable of providing SSS estimates with an accuracy of ~0.2 psu at 100-km spatial resolution. Prior simulations of a similar system (Njoku et al., 1999) have shown that soil moisture estimates of accuracy ~0.04 g cm^{-3} at 40-km spatial resolution are obtainable.

A feature of the scanning reflector concept is the feasibility of including multiple frequencies and polarizations in the feedhorns. Additional frequencies would extend the potential applications to include measurements of SST, ocean wind speed and direction, precipitation, sea-ice, snow, and other environmental parameters in addition to SSS and soil moisture. With a large antenna, these measurements can be made at much higher spatial resolutions than are currently feasible. Table 1.1-1 shows the heritage of conically-scanning spaceborne microwave sensors. A conical scan provides fixed incidence angle across the swath which is advantageous for obtaining accurate geophysical retrievals. The mesh antenna concept is a logical extension to larger-aperture

3

Table 1.1-1. Heritage and Characteristics of Conically-Scanning Scaceborne Microwave Sensors

Parameter	SMMR (Nimbus-7)	SSM/I (DMSP)	SeaWinds (Quickscat)	AMSR (ADEOS-II) (EOS) *	OSIRIS **
Sensor type	Radiometer	Radiometer	Radar	Radiometer	Radiometer and Radar
Frequencies (GHz)	6.6, 10.7, 18, 21, 37	19.3, 22.3, 37, 85.5	13.4	6.9, 10.7, 18.7, 23.8, 36.5, 89	1.2, 1.4, 2.7, (6.9), (10.7), (19)
Altitude (km)	955	860	803	705	600
Antenna size (m)	0.8	0.6	1.0	1.6	6
Incidence angle (deg)	50.3	53.1	46, 54	55	40–55
Footprint size (km)					
at ~ 7 GHz	140			65	<15
at ~ 13 GHz			30		
at ~19 GHz	55	68		23	(<6)
Swath width (km)	780	1400	1400, 1800	1445	~1000
Launch date	1978	1987—Series	1999	2002	

* EOS values are shown.

** Only 1–3 GHz frequencies are considered in the baseline study. However, the mesh antenna is expected to provide good performance at frequencies up to about 19 GHz.

systems, and provides a capability for new measurements and higher spatial resolution while keeping overall mission costs within acceptable bounds. The antenna configuration studied here is one of a number of candidate options. Alternate antenna configurations, such as parabolic-torus reflectors with scanning or pushbroom feeds, are also of interest. These designs do not require a rotating reflector, but require a much larger reflector diameter than considered here.

1.1.3 Objectives

The OSIRIS concept was the starting point to determine specifications and error budgets for the instrument and to evaluate the science performance. Key technology issues were identified to scope the study. The capability of a tensioned wire mesh to serve as a high-precision reflector surface at low frequencies is a key requirement. The emissivity must be low enough that uncertainties in the physical temperature of the mesh do not give rise to excessive thermal noise. The design of the reflector and feedhorns, and the surface shape and precision of the reflector, must provide antenna patterns of high beam efficiency, low sidelobes, and low cross-polarization. Mass and power requirements must be kept to a minimum, and the rotational dynamics of the antenna and the attitude control requirements and capabilities of the spacecraft must be well understood. A key objective was to develop an antenna design (reflector and boom) and select a spacecraft that would enable the volume of the combined antenna and spacecraft in the stowed configuration, and the total mass, to be within the capabilities of a low-cost launch vehicle. To address these issues, the specific objectives were as follows:

(1) Perform a requirements analysis to validate the baseline instrument design (measurement channels, sensitivities, beam-pointing, sampling, and other system and orbital characteristics) and to assess the geophysical retrieval accuracies and allowable error budgets for the instrument subsystems

4

(2) Perform laboratory measurements of wire mesh samples to determine their microwave emissivity, and evaluate the ability of mesh reflectors to meet the required brightness temperature precision and calibration stability

(3) Design lightweight, multifrequency, dual-polarized feedhorns and electronics subsystems, including passive and active channels at L- and S-band frequencies, for a rotating parabolic mesh reflector system, and analyze the antenna pattern characteristics and performance

(4) Perform an antenna and spacecraft configuration, integration, and optimization study, including deployable antenna, antenna/spacecraft interface, structure and mechanisms, mechanical and thermal modeling, and attitude control analysis of the antenna and spacecraft system.

1.2 TASK PLAN

1.2.1 Subtasks

The study was partitioned into the five interrelated subtasks listed below, each addressing a separate aspect of the system design and feasibility. A baseline system design was developed at the outset of the study to serve as the point of departure for concept validation, refinement, and analysis.

The five subtasks performed were:

(1) *Requirements Analysis*: Develop the baseline instrument specifications and design, including error budgets, to meet the combined ocean salinity and soil moisture requirements, and perform simulations and system trades to optimize the baseline configuration.

(2) *Mesh Radiometric Performance*: Perform laboratory measurements of mesh emissivity and predict the radiometric performance of the reflector in a simulated orbital thermal environment.

(3) *Antenna and Feed Design*: Design and optimize the reflector and feed configuration to achieve a compact lightweight design and evaluate the antenna beam performance under simulated spaceborne conditions.

(4) *Lightweight Radar Electronics*: Design a lightweight radar system with mass, volume, and power estimates that meet the requirements of a baseline low-cost science mission. (It was determined early in the study that the radiometer electronics were not a primary technology driver; hence, this subtask emphasized the radar electronics.)

(5) *Antenna, Spacecraft, and Launch Vehicle Configuration and Optimization*: Identify and evaluate deployable mesh antenna concepts and low-cost spacecraft and launch vehicles. Investigate the dynamics and attitude control of the antenna and spacecraft system and the ability of the overall system to meet the science requirements.

The key system characteristics are listed in Table 1.2-1. The system features a 6-m diameter offset-fed parabolic reflector antenna mounted on a small spacecraft bus. The antenna rotates about the nadir axis. The spacecraft can be either 3-axis-stabilized with the antenna mounted on a

Table 1.2-1. Summary OSIRIS System Parameters

• Deployable-mesh, parabolic reflector	• 1.2° pointing control (0.1° knowledge) (3σ)
• 6-m-diameter aperture	• Polar, 6am/6pm sun-synchronous orbit
• 36° offset angle beams	• 600-km altitude
• 6-rpm rotation rate	• 40-km spatial resolution
• 1.26 GHz radar; VV, HH, VH, HV	• 3-day global coverage
• 1.41 and 2.69 GHz radiometer; V, H (1.4 GHz polarimetric)	• Measurements of ocean salinity and soil moisture
• 2 multichannel feedhorns (each L- and S-band, V and H pol)	• Concept extendable to measurements of ocean winds, sea ice, and snow
• Feedhorn dimensions 0.6 x 0.6 x 0.9 m	• Explorer-class mission
• Approx. equal beamwidths all channels	• 3-year mission lifetime
• >90% beam efficiency; <-18 dB cross-pol	• Taurus-class launch vehicle

spun platform, or the spacecraft and antenna can rotate together as a rigid body. There are dual identical feedhorns providing two antenna beams, allowing the reflector to spin at a moderate rate (6 rpm) while providing overlapping 3-dB-footprint coverage at Earth's surface. With a polar Sun-synchronous orbit, at a nominal altitude of 600 km, the spatial resolution achieved is about 40 km and global repeat coverage at the equator is achieved in 3 days. The radiometer operates in protected frequency bands at 1.41 and 2.69 GHz while the radar operates at 1.26 GHz. Each feedhorn includes an identical set of radiometer and radar frequencies and polarizations. The rationale leading to this system design is provided in Section 3.

1.2.2 Technology Readiness

The task plan was developed with the intent of advancing the technology readiness of the OSIRIS concept to an acceptable level for an Earth science mission, and to organize the team contributions and subtask schedules to accomplish this intent. Based on the state of the technology, and the performance knowledge of each subsystem at the start of the task, the entry level for the overall system was estimated to be at technology readiness level (TRL) 4. At this level, analytic proofs-of-concept of individual components and subsystems have been performed, demonstrating a capability to meet the performance required of a potential flight mission. The desired exit level of the task was TRL 6-7. This level requires that all subsystems should have been demonstrated in a relevant (space or ground) environment, and thermal and mechanical modeling of all subsystems working together in a simulated space environment should have been done. The following step would be an actual flight of the system in a space mission.

1.2.3 Team Organization

The study was managed by the Jet Propulsion Laboratory (JPL) in collaboration with the NASA Langley Research Center (LaRC). Major parts of the study were performed through subcontracts with the University of California Los Angeles (UCLA), Science Applications International Corporation (SAIC), TRW and TRW Astro Aerospace, and Spectrum Astro. Table 1.2-2 shows the breakdown of the key team member responsibilities by subtask. Many other individuals also contributed to the study. Team-I is a concurrent design environment within the JPL Project Design Center that provided support to the OSIRIS team. The Advanced Radar Technology

Table 1.2-2. Team Member Roles and Responsibilities

Subtask	Team Member
0. Team Coordination	E. Njoku (JPL)
1. Requirements Analysis	E. Njoku (JPL), W. Wilson (JPL), S. Yueh (JPL)
2. Mesh Measurements	T. Campbell (LaRC), W. Lawrence (LaRC)
3. Antenna and Feed Design	Y. Rahmat-Samii (UCLA), W. Wilson (JPL)
4. Lightweight Radar Electronics	S. Yueh (JPL), W. Wilson (JPL), R. West (JPL), G. Sadowy (JPL), D. Farra (JPL), W. Edelstein (JPL/ARTP)
5. Antenna, Spacecraft, and Launch Vehicle Configuration and Optimization	R. Freeland (JPL), R. Helms (JPL), H. Feingold (SAIC), K. Oxnevad (JPL/Team-I), M. Thomson (TRW), G. Konicke (Spectrum Astro)

Program (ARTP) at JPL provided shared funding in support of the Lightweight Radar Electronics subtask.

1.3 REPORT OUTLINE

The organization of this report is as follows. Section 1 provides an outline of the study and conclusions of the work performed. Section 2 provides a brief background on mesh antenna issues relevant to the present study. Section 3 presents the science requirements for ocean salinity and soil moisture, the OSIRIS baseline design, and an analysis of the required accuracies and error budget. In Section 4 an evaluation of the baseline design is provided, and the selections of candidate antennas and spacecraft are described. The selected antenna and spacecraft were used in the analyses of the antenna/spacecraft rotational dynamics and attitude control (Section 8).

In Section 5 the design of the antenna and feedhorn configuration is described, and results of antenna pattern calculations are presented for the dual-feedhorn configuration. Results of the weight-reduction optimization of the feedhorns are described. Section 6 describes the methods and results of laboratory measurements performed to characterize the emissivities of mesh samples. An assessment is provided of the impact of mesh emissivity and orbital thermal environment on the OSIRIS measurement precision and stability. Section 7 describes the design and performance characteristics of a lightweight radar subsystem suitable for OSIRIS.

The studies reported in Sections 3 through 7 collectively defined the optimized OSIRIS baseline system. The specifications of this system were used as the basis for two industry studies, described in Section 8 of this report, that were carried out during the second year of the study. These studies evaluated the rotational dynamics and attitude control of the combined antenna/spacecraft system and the overall capabilities of the spacecraft to support the OSIRIS system requirements. The industry contract reports are included in the Appendices.

1.4 PUBLICATIONS

Two journal papers (Njoku et al., 2000a; Yueh et al., 2001) and four conference proceedings papers (Njoku et al., 2000b, 2001; Wilson et al., 2000; Lawrence and Campbell, 2000) have been published describing the OSIRIS concept, feasibility, and error analysis.

7

1.5 KEY RESULTS AND CONCLUSIONS

Sections 3 through 8 of this report document work performed and results obtained in this study. The key results and conclusions are presented below.

Our overall conclusion from this study is that the OSIRIS concept represents a challenging yet feasible and low-cost approach to the remote sensing of soil moisture and ocean salinity. This conclusion is based on the following. (1) The AstroMesh antenna design is flight proven, and a 12-m version has been launched and deployed successfully in geosynchronous orbit. Discussions with the manufacturer indicate that the operational antenna radiation patterns (gain and sidelobe levels) are better than expected. (2) Designs of the antenna feedhorn and radar electronics have been completed that lead to a lightweight instrument system with antenna pattern characteristics and calibration stability that meet the science requirements. (3) Existing catalog spacecraft have been evaluated that are capable of supporting and controlling the instrument to within the desired pointing accuracy with only minor modifications to the spacecraft. The study included simulations of the spin dynamics of the spacecraft/antenna system and design of the antenna balancing scheme and spacecraft attitude control systems. The entire payload can be launched to the desired orbit with a Taurus-92 launch vehicle. (4) Laboratory measurements of vendor-provided mesh samples show that the reflector mesh emissivity is low enough to provide sufficient calibration stability for soil moisture measurements and, with careful modeling of the temperature variations of the reflector surface in orbit, sufficient calibration stability for ocean salinity measurements.

1.5.1 Requirements Analysis

Science requirements for ocean salinity and soil moisture, derived from recent NASA workshops, were used to develop the baseline OSIRIS instrument concept including a detailed set of performance characteristics. A retrieval analysis for sea surface salinity (SSS) using these performance characteristics showed that the system is capable of achieving the required 0.2 psu SSS accuracy if the stringent requirements imposed on instrument sensitivity and calibration stability can be met and a detailed accounting of geophysical error sources is included in the retrievals. The key requirement for SSS is a radiometric error, including instrument noise, geophysical modeling error, and calibration error, of better than ~0.3 K at 50-km resolution. The non-zero emissivity of the mesh reflector may cause the calibration error to exceed the feasibility limit for salinity sensing if the physical temperature of the mesh cannot be characterized adequately in orbit. For soil moisture, the system is more than capable of meeting the required 0.04 g cm^{-3} accuracy since the required radiometric error is ~1 K.

1.5.2 Concept Definition

The TRW AstroMesh antenna and Harris DTS antenna were both identified as viable mesh antenna candidates. The AstroMesh antenna was selected for this study based on the deployed stiffness advantage due to the perimeter truss design for a spinning configuration and the ready availability of data on this antenna from the manufacturer (TRW Astro). Spacecraft buses from TRW and Spectrum Astro, available in the RSDO catalog, were identified as viable candidates for the rigid-spinner or 3-axis-stabilized configurations. The Taurus (92-inch fairing) was identified as the lowest cost launch vehicle with sufficient payload volume and mass performance to the required orbit. The configuration with the antenna above the spacecraft was determined to

be optimal. Configuration drawings of the antenna reflector, interface boom, and satellite bus within the Taurus 92-inch fairing, and a proposed deployment sequence were developed to show feasibility. A preliminary attitude control system (ACS) analysis was done. The momentum storage requirement was determined to be in the range of 120 N-m-s (3-axis) to 200 N-m-s (spinner). A preliminary structural analysis of the reflector and boom was performed by Team-I to determine the boom stiffness required for minimal rotational deflection of the reflector. Based on recommendations resulting from the initial SAIC and Team-I studies, two parallel approaches for the OSIRIS spacecraft were subsequently pursued.

1.5.3 Antenna and Feed Design

A compact, offset-fed, parabolic reflector antenna system (f/D = 0.6) was designed to produce from Earth orbit dual-beam mapping coverage of the Earth's surface. A compact (minimum-length) corrugated horn feed was designed, and the effects of feed displacement for the dual-beam application were examined. The radiation performance of the reflector antenna system was studied in detail in terms of key radiation characteristics, including far-field patterns, beam contour patterns, and reflector surface distortions. The effects of anticipated random distortions of the reflector surface were included. Taking into account the multifrequency, offset, dual-beam requirement, it was shown that the design would provide antenna patterns with good symmetry, sidelobe, and cross-polarization characteristics. The required 90% beam efficiency would be met provided the random surface error was below 1.4 mm (imposed at the 2.7-GHz frequency). At 1.4 GHz the required surface error is 3.9 mm. It was assumed that a suitable feeding network would be developed for the horns to separate the signals at the three different operating frequencies and two polarizations. The return loss of this network was not included in the analysis.

The corrugated feedhorn design was optimized for weight reduction using brute-force and genetic algorithm (GA) approaches. Significant weight reductions were realized by careful choice of the number and thickness of the corrugations while maintaining the radiation pattern performance. Genetic algorithms are a powerful tool in the optimization of corrugated horns, and in this case proved effective in reducing the horn length by 12.3%. The GA-optimized horn also provides superior reflection loss (13-dB improvement) over the brute-force design. The estimated weight of the feedhorn is about 15 lb. The manufacture, testing, and space qualification of the feedhorn design should be carried out as part of a subsequent flight program.

1.5.4 Mesh Measurements

A Materials Emissivity Measurement System (MEMS) facility was developed at the NASA LaRC to perform precision radiometric and vector network analyzer measurements of the emissivity of commercial mesh samples. The measurement system improved on an earlier system developed at LaRC in the 1980s for similar purposes. The measured emissivities were ~0.003 (±0.001) and 0.008 (±0.002) for meshes of 20 and 10 openings per inch (opi), respectively. The denser weave (20 opi) exhibited lower emissivity. The effects of varying tension or temperature on the mesh emissivity were not measurable within the accuracy of the measurement system.

A thermal analysis of the reflector mesh was performed using a membrane model with appropriate materials characteristics and in-orbit simulated heating inputs (Sun and Earth). The results showed an average mesh temperature of 380 K, and peak-to-peak deviations of ±20 K for

the vernal equinox (best case) and ±122 K for the winter solstice (worst case). For the 20 opi mesh these 'uncorrected' temperature variations give rise to peak-to-peak errors of ±0.06 and ±0.37 K for the best and worst cases, respectively. This is acceptable for measurement of soil moisture but not for salinity measurement. For a Sun-synchronous orbit, however, given the repeatability of the mesh temperature variability from orbit to orbit, the variability should be predictable to at least 20% or better. In this case the 'corrected' temperature variations would give rise to peak-to-peak errors of ±0.012 and ±0.074 K, respectively (a factor of five improvement). These errors are acceptable for salinity measurement, particularly since the worst case (winter solstice) results are due to eclipse periods that are of short duration compared to the annual cycle, such that the measurements are degraded for a limited period of time. It should be noted that an in-orbit calibration bias and variability correction, as described above, is usually necessary in microwave radiometry. For instance, Wentz et al. (2001) describe the method used for correcting the Tropical Rainfall Measuring Mission Microwave Imager (TRMM/TMI) data, which had much larger antenna calibration bias variations than anticipated for OSIRIS.

1.5.5 Radar Electronics

It is important to keep the overall mass low for a mechanically scanning instrument to reduce the requirement for spacecraft momentum compensation. Advanced technology radar designs were explored in this study for the radio frequency subsystem (RFS), command/data/timing subsystem (CDTS) and power subsystem. MMIC designs were considered for the radar receivers, and solid state amplifiers for RF power transmitters, to reduce the size and weight of the RF subsystem. Information was drawn from prior studies conducted under the JPL Advanced Radar Technology Program (ARTP) over the past few years.

A detailed design of the radar electronics subsystem was performed. The radar is a dual-polarized, L-band (1.25 GHz), slow-chirp system. The projected sensitivity of the system as designed was calculated and found to agree with the performance specifications. Power, volume and mass estimates were made using components mostly with proven space heritage. A laboratory breadboard polarimetric radar for ocean wind and salinity sensing was built and tested using contributed funding. The breadboard system demonstrated the required gain and phase stability and performance of the radar calibration loop.

1.5.6 Antenna, Spacecraft and Launch Vehicle Configuration

Based on recommendations resulting from the initial SAIC and Team-I system studies, two parallel approaches for the OSIRIS spacecraft were subsequently pursued. One design focused on a rigid-body spinner spacecraft, while a second design focused on a three-axis-stabilized spacecraft. Both were based on low-cost, previously flown spacecraft from TRW and Spectrum Astro, respectively.

TRW Astro developed a concept and structural design to interface the 6-m AstroMesh reflector antenna with both the Spectrum Astro Coriolis and TRW T-200 candidate spacecraft. The interface structure (a) supported the stowed antenna during boost, (b) articulated the stowed antenna to its operational position, and (c) supported the deployed antenna for the mission duration. Stowed and deployed configurations for both spacecraft were developed. Stowed configurations were shown to fit within the fairing constraints of the Taurus launch vehicle.

10

Configuration designs were developed for the full complement of necessary structural and mechanical elements including the reflector, boom (struts, actuators, deployment drive, balance mass), and tie-downs. Structural analysis was done using the AstroMesh antenna finite element model (FEM) to determine the dynamic characteristics of the deployed antenna and the quasi-static deflection of the antenna/boom, and to show that a 6-meter AstroMesh antenna and support boom can be made sufficiently stiff, and dynamically balanced, to satisfy the OSIRIS mission pointing requirements. The AstroMesh antenna had a successful first flight and deployment (non-spinning) on the Thuraya mission in November 2000.

The rigid body spinner proposed by TRW for the OSIRIS mission was based on their T-200 bus but differed substantially from the rigid spinner configuration considered earlier. The deployed configuration had the antenna feedhorns mounted on the side of the spacecraft rather than the top. The TRW launch configuration oriented the spacecraft with the spin axis perpendicular to the launch axis. Advantages of this configuration included simplified ACS accommodation, simplified deployment of antenna and solar array, and reduced volume requirements. Issues associated with this configuration include the need for an inertial product adjustment device to fine tune the spacecraft center of gravity on orbit, a root damper or higher frequency design of the solar panels to eliminate potential problems related to their rotation at rates near their natural frequency, and augmentation of the power subsystem to accommodate the payload requirements. TRW concluded that the rigid body spinner using their T-200 bus was a feasible approach, with available margins on payload weight and pointing accuracy. Further analysis is needed, however, before pursuing the rigid body spinner option in an actual mission.

The Spectrum Astro study was based on the three-axis-stabilized bus used in the Coriolis program. Like OSIRIS, the Coriolis mission required a rotating antenna (smaller, but with a much higher rotation rate) mounted to a spin table atop a nadir pointing, three-axis-stabilized spacecraft in Sun-synchronous orbit. Documentation of the Spectrum Astro study was provided in a set of reports including: (1) a technical summary, identifying the needed changes and modifications to the Coriolis spacecraft and providing the required set of spacecraft metrics; (2) results of the FEM analyses; (3) an attitude control study addressing the ACS design and spacecraft control issues; and (4) a set of spacecraft configuration drawings. The results of the Spectrum Astro study support the conclusion that the spacecraft design represents a feasible, low risk approach.

2. BACKGROUND

2.1 ANTENNA STRUCTURE

Key technology aspects of mesh antennas include deployment reliability, deployed stiffness, and radio-frequency (RF) performance. They include the design of the structural elements, which control deployment and surface shaping, and the characteristics of the wire mesh materials, weave and density (openings per inch), which affect the antenna radiation pattern and surface emissivity. At the beginning of this study, a survey was done of existing mesh antenna designs and their heritage and technology status. The results of the survey are reviewed in Section 4. The three designs of primary interest are the radial rib, double-articulated radial rib, and perimeter truss. All three structural types can be configured as offset-fed parabolic reflectors as required for OSIRIS. The basic structural elements common to these concepts are discussed below.

2.1.1 Basic Elements

The deployable support structure functions to (1) support the stowed reflector structure, (2) release the stowed reflector structure on orbit and provide tension to the cable system in order to bring it to the deployed configuration, and (3) provide on-orbit stiffness and thermal stability. There are a number of different configurations used for these types of structures. The mesh reflector surface is typically fabricated from 1.2-mil gold-plated molybdenum wire, woven in a diamond shaped pattern. The required density of the wires is dictated by the wavelength of operation. Typically, a 10-openings-per-inch (opi) knit density has been used, which provides excellent reflectivity up to X-band. Denser weaves (20 opi and higher) are being introduced that can provide improved RF performance. The flexible nature of the knit allows the individual wires to shift relative to each other when not under tension. This characteristic allows the mesh to be stowed compactly and then tensioned to the deployed configuration with minimal short wavelength surface error. The reflectivity and transmission loss characteristics of these wire meshes have been studied in detail (Rahmat-Samii and Lee, 1985; Imbriale et al., 1991). The reflector surface shaping system is used to shape the mesh reflector surface, and is a function of the specific structural design concept. The most commonly used technique is a network of tensioned cables or webbing that provides a tie-down structure for the large number of flexible ties that interface with the mesh surface. The larger the number of ties, the higher the resulting surface precision.

2.1.2 Structural Concepts

Three generic types of deployable mesh antennas were considered for this study, representing the most mature and applicable designs suited to the OSIRIS requirements. All these designs have been launched and deployed in space.

(a) Radial Rib Concept. The radial rib is kinematically one of the simplest structural concepts used for mesh deployable antennas. The best example of this concept is the TDRSS antenna manufactured by Harris Corp. This structure utilizes graphite epoxy ribs that are hinged at their base with one simple articulation for deployment. The stowed configuration is a narrow shaped cylinder. The ribs support the mesh reflecting surface and the network of cables and ties used to form and maintain the precision reflector surface. The ribs provide the basic support structure for

the mesh net system and orbital thermal stability and do not have to be high precision themselves. The disadvantage of this concept is the length of the stowed antenna structure.

(b) Double Articulated Radial Concept. The basic difference between the radial rib and the double articulated radial rib is that the latter concept utilizes a second hinge located at the midpoint of the rib. This enables the rib to be double folded to reduce the length of the stowed structure. This approach is kinematically much more complicated than the simple radial rib due to the addition of the cables, actuators and mechanisms needed to implement the double fold of the ribs. Deployed stiffness of the ribs is achieved by using standoffs at the center hinge in conjunction with tensioned cables to achieve a truss type support structure. The mesh reflector structure and its surface shaping network of cables and ties is supported by the rib structure. The two best examples of this concept are the TRW PAMS and the Harris Corp. DTS antennas. Two 12-meter DTS antennas were developed and launched on the geosynchronous mobile communication satellite Garuda-1 in 2000 (Figure 2.1-1(a)). The TRW PAMS antenna has been developed to the point of flight readiness at the 10-meter size. The deployed stiffness and orbital thermal stability for both concepts is high. This structural concept has potential for antenna sizes up to 20 meters in diameter.
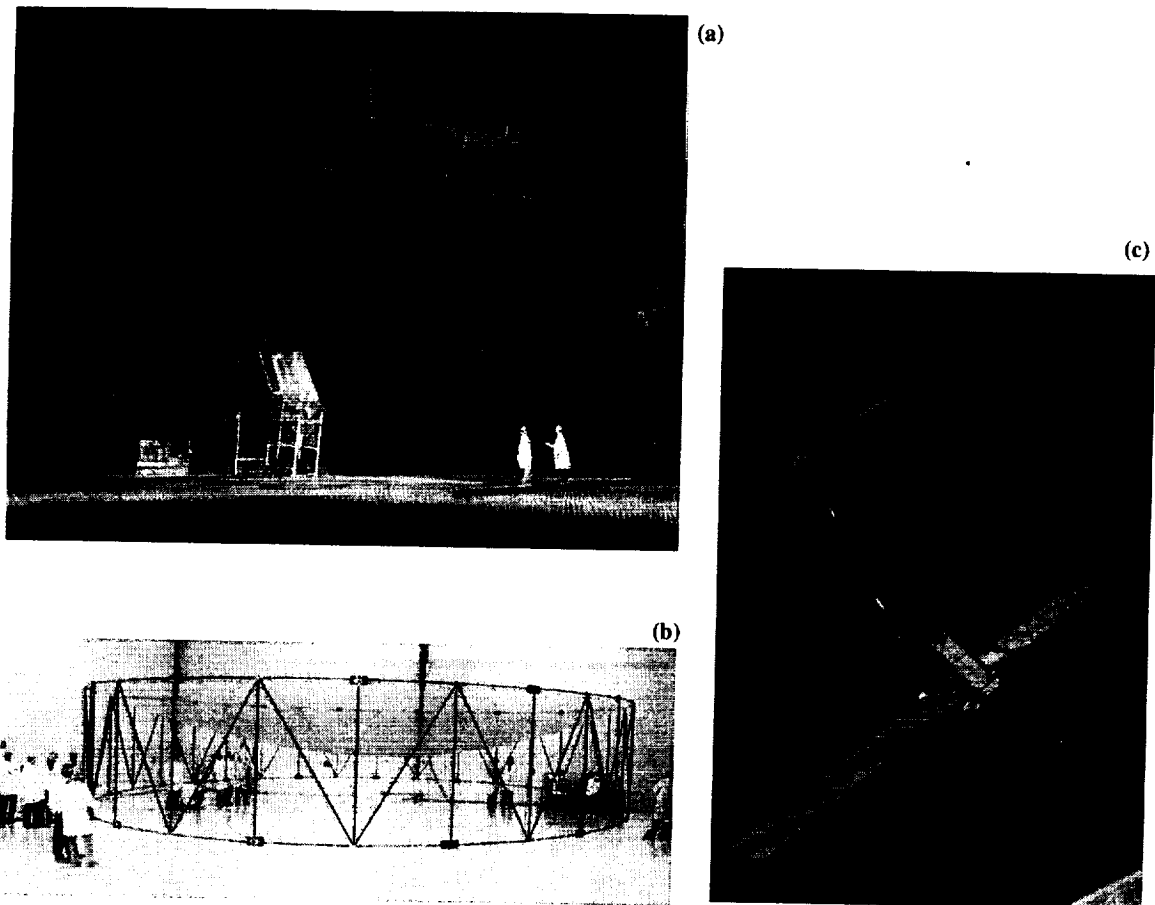
Figure 2.1-1. (a) Harris Corp. 12-m radial-rib antenna in test facility. (b) TRW Astro 12-m AstroMesh perimeter-truss antenna. (c) Artist's concept of AstroMesh antenna. ((a) Courtesy of Harris Corp.; (b) and (c) courtesy of TRW Astro.)

(c) Perimeter Truss Concept This relatively new structural concept is based on a toroidal-shaped truss structure that supports the mesh reflector and its surface-shaping network of cables and ties at their outer perimeter. The toroidal structure consists of a series of deployable truss bays that are deployed in a synchronized manner with cables located at the top and bottom of the bays. The stowed structural configuration is in the shape of a cylinder that expands radially to form the toroidal-shaped truss that stretches the mesh over the open cavity. As with radial rib concepts, the toroidal truss structure provides deployed stiffness and orbital thermal stability to the antenna. The best example of this new type of structure is the TRW Astro AstroMesh reflector. A 12-meter AstroMesh antenna was launched on the geosynchronous mobile communication satellite Thuraya in 2000 (Figure 2.1-1(b), (c)). This concept has potential for antenna sizes up to 25 meters in diameter and possibly larger. Additional information on the AstroMesh antenna is provided in Appendix I.

2.1.3 Performance

A significant mechanical issue associated with large mesh antennas is deployment reliability. As mentioned above, the antenna concepts considered in this study (DTS and AstroMesh) have both been launched and deployed recently in orbit. The orbital performances of these antennas will undergo continuing evaluations, while additional launches of these types of antennas are scheduled to take place during the coming years.

The DTS and AstroMesh antennas were designed initially for applications that require surface shape precision of 0.5 mm rms. This precision provides a $\lambda/40$ performance or better at frequencies up to 15 GHz, and more than meets the OSIRIS requirement. The orbital thermal stability of the reflector shape for these antennas is also excellent, since composites with extremely stable thermal materials are used for the support structures. Additionally, the surface shaping cables and ties use thermally-stable materials such as carbon, kevlar, quartz and others.

2.2 RADIOMETRIC PERFORMANCE

The RF performance of mesh antennas is determined not only by their antenna radiation pattern characteristics but also by their noise performance and calibration stability. The latter are influenced primarily by the microwave emission characteristics of the mesh surface. These characteristics must be assessed so that their contributions to the overall system noise and calibration error can be predicted, and accurate brightness temperature (T_B) measurements made. This is particularly important for ocean salinity, which requires a T_B measurement precision and calibration stability of better than 0.2 K. Knowledge of the mesh emissivity and the on-orbit physical temperature variability of the mesh are necessary to determine the calibration stability. Designing a radiometer for precision measurements from space places stringent requirements on all components of the radiometer and antenna system, and also on the laboratory methods used to characterize these components.

In the early 1980's the Langley Research Center (LaRC) and the Naval Research Laboratory (NRL) collaborated to investigate the suitability of a mesh reflector for a Low Frequency Microwave Radiometer (LFMR) instrument that was proposed for the Navy Remote Ocean Sensing Satellite (NROSS) program (Figure 1.1-1). In this effort LaRC developed several experimental measurement systems based on radiometric principles, and determined the emissivities of typical mesh materials, metallized membranes, and coatings. The emissivity of

the mesh materials was measured directly by using a laboratory radiometer to determine the brightness temperature variations of the mesh samples over a known temperature range. The accuracy of this method was maintained by using a very stable cryogenic load as a reference source for the radiometric sensor. The results of this study indicated that mesh materials were acceptable for radiometer applications but knowledge of the mesh properties would be necessary for accurate calibration. These studies have been continued in the present work. Section 6 describes the advances made in the LaRC mesh emissivity measurement system as part of this study and the new measurement results obtained.

3. REQUIREMENTS AND BASELINE CONCEPT

3.1 OUTLINE

As a first step in the OSIRIS study top-level system requirements were defined and a baseline design concept was developed that could be used in subsequent analyses and trade-offs. The design process included development of an error budget that could be used to specify requirements for the instrument subsystems and assess the in-orbit operation of the system. The requirements analysis subtask addressed the following objectives:

(1) Review the requirements for ocean salinity and soil moisture as science drivers for the spaceborne deployable mesh antenna system. Considerations include retrieval accuracy, spatial and temporal resolution and coverage, orbit characteristics, mission duration, data system, and system cost.

(2) Design an instrument and spaceborne implementation to meet the science requirements. System specifications include antenna type and size, scanning mode, radiometer and radar characteristics, and data sampling. These specifications depend on the physics of ocean microwave emission and scattering, instrumentation options, and desired orbit, spatial resolution and coverage characteristics.

(3) Develop an error budget and perform retrieval simulations to show the capability of the baseline system relative to the science requirements. The error budget leads to requirements on antenna pointing (control and knowledge), radiometer and radar calibration, and antenna beam characteristics that have implications on mesh emissivity requirements, receiver design, reflector and feed design, spacecraft integration, and attitude control. These requirements form the starting point for other subtasks of the study.

3.2 REQUIREMENTS

An earlier concept for soil moisture and ocean salinity sensing using a large inflatable antenna was described by Njoku et al. (1999). That concept used a 10-m effective aperture conical-pushbroom system and dual-polarized L- and S-band frequencies. An analysis of the soil moisture science requirements and retrieval method was presented in that paper as a basis for determining the instrument and mission system requirements. In the present study the soil moisture analysis is not repeated. The analysis here focuses on ocean salinity as the driver for the instrument and mission requirements. Salinity sensing requires better radiometric precision, calibration stability, and correction for geophysical perturbations than soil moisture sensing, although the spatial resolution requirements (at least for open ocean) are less demanding than for soil moisture.

Science requirements for sea surface salinity (SSS) and soil moisture were developed independently in a series of workshops organized as part of NASA's strategic planning process (Lagerloef, 1998; Jackson, 1999; NASA, 2000). The requirements are summarized in Table 3.2-1.

The salinity requirements are based on improving seasonal-to-interannual El Niño Southern Oscillation (ENSO) climate predictions, improving ocean rainfall estimates and global hydrologic

Table 3.2-1. Science Requirements for Sea Surface Salinity and Soil Moisture from Space

(a) Sea surface salinity (Lagerloef, 1998)

Application	Accuracy	Spatial Resolution	Temporal Resolution
ENSO Variability	0.2 psu	100 km	1 week
Water Budget	< 0.1 psu	200 km	1 month

(b) Soil moisture (Jackson, 1999)

Application	Accuracy	Spatial Resolution	Temporal Resolution
Hydroclimate	0.04 g cm^{-3}	40 km	3 days
Hydrometeorology	0.04 g cm^{-3}	10 km**	3 days

** Not considered in the present study

budgets, and monitoring large-scale salinity anomalies, such as tracking interannual SSS variability in the Nordic Seas. The accuracy requirements depend on the space and time scales of the phenomena to be resolved. The signal for the ENSO problem is estimated to have a length scale of >100 km, a weekly time scale, and a strength of 0.05 to 1 psu. The accuracy requirement for surface water flux has been estimated as ~0.05 psu, at 2° × 2° lat-lon and monthly resolution in low to mid latitudes, while the high-latitude salinity variability signal is ~0.01 psu at ~100 km. This latter signal will be difficult to detect using remote sensing. To address the first two objectives an accuracy goal of 0.2 psu, at 100-km, 1-week space and time scales is adequate. Depending on the correlation scales of the measurement errors, and the ability to assimilate in situ data for calibration, improved accuracy may be achievable at larger space and time scales.

The soil moisture applications require spatial resolutions that are determined by the scales at which variations in soil moisture affect the local weather (~10 km) and intraseasonal climate (~40 km). These are the hydrometeorology and hydroclimate scales, respectively. The 10-km resolution, using real-aperture sensing, requires a larger antenna (~25 m) than studied here. The 6-m antenna OSIRIS baseline concept will thus not meet the hydrometeorology requirement. In a subsequent study a modification of the OSIRIS concept to include a synthetic aperture radar has been investigated that can meet the hydrometeorology requirement in low-vegetated areas (Njoku et al., 2001). Follow-on studies are also being conducted as a continuation of this IIP task to investigate the feasibility of scaling the OSIRIS concept to larger antenna diameters to provide a 10-km radiometric resolution. The soil moisture accuracy requirement of 0.04 g cm^{-3} provides approximately ten levels of soil moisture discrimination between dry and saturated.

The requirements for ocean salinity were combined with those for hydroclimate soil moisture as the joint set of requirements for this study. This was considered an appropriate approach for a technology feasibility study. Some of the requirements can be relaxed for a discipline-focused salinity or soil moisture mission.

3.3 BASELINE SYSTEM

3.3.1 Physics Basis

At frequencies below ~3 GHz, an increase in SSS causes a significant increase in sea water conductivity and dielectric constant magnitude, decreasing the surface emissivity and brightness temperature (Swift, 1980). SSS can thus be inferred from observations of ocean brightness temperature in this frequency range. Other geophysical factors also affect the brightness temperature, such as SST, wind-induced roughness, atmospheric attenuation, sun glint, Faraday rotation, and galactic noise. Correction or avoidance of these factors is necessary to estimate SSS accurately. Figure 3.3-1 shows the computed sensitivities of brightness temperature (T_B) to SSS, sea surface temperature (SST), and wind speed as functions of frequency in the range 1–20 GHz, at 50° incidence angle, for vertical and horizontal polarizations. The curves were computed as described in Njoku et al. (2000a). The sensitivity is defined as $\partial T_B / \partial p$, where p is SST, SSS, or wind speed. The frequency and polarization dependencies shown in Figures 3.3-1(a) and (b) are representative of typical ocean parameter values. The magnitude of the sensitivity to SSS decreases rapidly as frequency increases. The sensitivity to SST increases from a negative value to a peak in the broad range of 4–10 GHz. The sensitivity to wind speed increases with frequency until atmospheric effects reduce the sensitivity above ~17 GHz. The sensitivities to SSS and SST are greater at V than at H polarization, while the converse is true for wind speed.
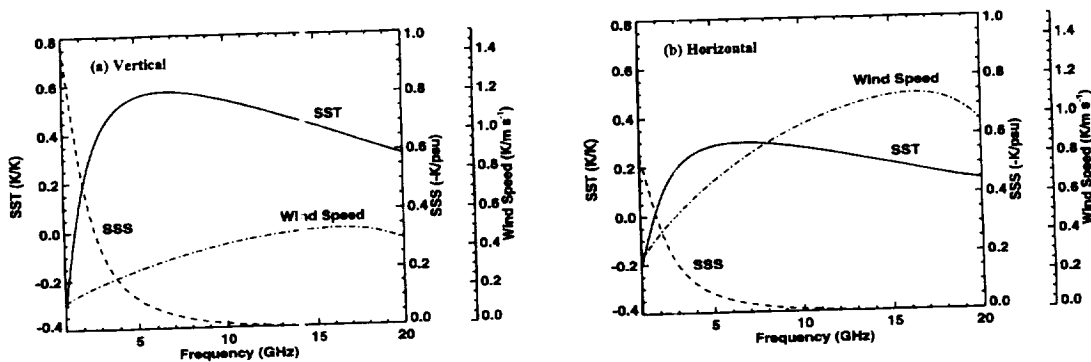
Figure 3.3-1. Modeled sensitivity $(\partial T_B / \partial p)$ of brightness temperature T_B to geophysical parameters p (SSS, SST, and wind speed) as functions of frequency, at 50° incidence angle, for: (a) vertical and (b) horizontal polarizations. Baseline values used are: SSS = 35 psu, SST = 25 °C, wind speed = 10 m s⁻¹, and precipitable water = 3 cm.

The differences in sensitivity to SST, SSS, and wind speed as functions of frequency and polarization allow these parameters to be estimated independently using multifrequency, dual-polarized measurements. L-band (~1.4 GHz) is the optimum frequency range for sensing SSS, since the brightness temperature sensitivity to SSS is high, and the sensitivities to SST and wind speed are low in this range. Dual-polarized measurements at S-band (~2.7 GHz) or C-band (~6 GHz) have higher sensitivities to SST and wind speed than at L-band, and lower sensitivities to SSS, and hence can be used to correct for the effects of SST and wind speed in estimation of SSS. To provide additional sensitivity and accuracy for the wind-induced roughness correction it is advantageous to include scatterometer (radar backscatter) measurements at L-band. Backscatter is more sensitive to surface roughness than emissivity and is relatively insensitive to

approximately the same frequencies and spatial resolutions so that similar roughness and spatial scales are sensed.

In this paper we have evaluated an integrated radiometer-scatterometer system that includes radiometers operating at 1.41 (L-band) and 2.69 GHz (S-band) with V and H polarizations, and a scatterometer operating at 1.26 GHz (L-band) with VV and HH polarizations. The frequencies at L- and S-bands were chosen to fall within the spectrum allocations for passive and active remote sensing. We have not optimized the selection of measurement channels, for example, by minimizing the SSS retrieval error as a function of different multichannel combinations. However, the simulations described below indicate the benefits of including radar channels in addition to the radiometric channels. The two key issues addressed in the simulations were: (1) determining how well SSS could be measured using the baseline system; and (2) determining the performance specifications required of the sensor subsystems for such SSS measurements.

3.3.2 System Design

A traceability matrix is shown in Table 3.3-1 indicating the derivation of the baseline system characteristics. The design was derived from the science requirements listed in Table 3.2-1. A low cost (less than about $120M as of FY99) and duration of 3 years were assumed as guidelines for an explorer-class science mission. The space/time resolution for SSS of 100 km/1 week can be obtained by acquiring raw data samples at a spatial resolution of 40 km with wide-swath global coverage every 3 days. An antenna diameter of 6 m is required to achieve 40-km spatial resolution from an orbit altitude of 600 km. The SSS accuracy requirement of 0.2 psu leads to requirements for radiometric precision of 0.1 K and calibration stability of 0.2 K, radar precision and stability of 0.2 dB, incidence angle of >40°, and a conical-scan (such that the incidence angle remains fixed across the swath). The corresponding precision and stability requirements for soil moisture are 0.7 K. A beam-pointing knowledge of 0.1° is required to keep the corresponding brightness temperature uncertainty to less than 0.15 K. Pointing control to within about half a 3-dB beamwidth is necessary for accurate geolocation. A polar, 6 am/6 pm Sun-synchronous orbit is required to obtain global coverage and to minimize Faraday rotation. This orbit is also advantageous from the point of view of thermal stability of the instrument and utilization of solar power.

Two configurations were initially considered for the OSIRIS application: (a) Conical-Scan—in which a wide swath is generated by rotating an offset-fed parabolic reflector with a small number of feeds about a vertical axis; and (b) Conical-Pushbroom—in which the swath is generated by a large number of feeds, or a few scanning feeds, at the focus of a non-scanning parabolic-torus antenna. The conical-pushbroom concept has the advantage that the reflector itself does not scan. However, the overall diameter of the reflector must be significantly larger, and the feed system and deployment are more complex. The conical-scan configuration on the other hand is conceptually simpler and cheaper, but the rotating reflector places increased demands on the spacecraft attitude control system. On balance, considering technology readiness, cost, and risk, the conical-scan configuration was adopted for the OSIRIS baseline design. A 6-m antenna was considered adequate to meet the science requirements. Due to the limitations on mission cost, compact low-mass and low-power designs are required for the radiometer and radar electronics and feeds. Corrugated horns allow a more compact feedhorn design. Equal beamwidths at all channels are desirable so that all channels view approximately the same surface footprint. This improves the accuracy of the geophysical retrievals. The requirements on beam efficiency,

20

Table 3.3-1. OSIRIS Requirements and Design Traceability Matrix

Science and Mission Requirements	Instrument and System Requirements	Instrument and System Design Elements
Accuracy	*Radiometers*	*Radiometers and Radar*
0.2 psu (salinity)	1.41 and 2.69 GHz, H & V	Compact, low mass, low power design
0.04 g cm⁻³ (soil moisture)	(1.41 GHz polarimetric)	
	0.1 K precision, 0.2 K stability (salinity)	*Antenna*
Space-time resolution of product		Offset-fed parabolic reflector, 6-m aperture, deployable-mesh, offset angle ~36°
100 km, 1 week (salinity)	0.7 K precision, 0.7 K stability (soil moisture)	
40 km, 3 days (soil moisture)	*Radar*	Rotation rate ~6 rpm
	1.26 GHz	Two corrugated-horn multichannel feeds
	VV, HH, VH, HV	
Space-time resolution of raw data	0.2 dB precision and stability	Equal beamwidths all channels
40 km, 3 days	*Antenna*	>90% beam efficiency, >35 dB gain, <-18 dB cross-polarization
	6-m aperture	
Mission duration		*Orbit*
3 years	*Pointing*	Altitude 600 km
	Fixed-incidence-angle beams	
	>40° incidence	*Spacecraft*
	Control: 0.5x beamwidth (3σ)	Full-spinner or 3-axis-stabilized with spinning platform
	Knowledge: 0.1° (3σ)	
		System Calibration
	Swath Width	Cold-space view, in-situ data
	~1000 km	
		Launch Vehicle
	Orbit	Taurus class
	Polar, sun-synchronous, 6 am/6 pm equator crossing	

antenna gain, and cross-polarization provide good sensitivity for the retrievals and avoid the need for antenna pattern corrections. Absolute calibration of the entire system in orbit, including the antenna reflector calibration and pointing control, can be accomplished by occasionally rotating the entire system to provide a cold-space view and by calibration against stable in situ targets on the surface.

A number of configurations were considered for the orientation of the antenna and the position of the antenna relative to the spacecraft. Stability considerations dictated that the center of mass of the spinning system be on the vertical rotation axis. Due to the requirement to minimize the amount of solar radiation entering the feedhorns and reflector sidelobes during a full rotational scan of the antenna, a configuration with the feedhorns below the reflector was chosen. A preliminary analysis indicated that, for this configuration, positioning the spacecraft below rather than above the antenna would result in a system that was simpler to deploy and control in orbit, and would place the radar and radiometer electronics close to the feeds and the spacecraft data system. Hence, this configuration was adopted for the baseline system. An artist's depiction of this configuration is shown above in Figure 1.1-2.

3.3.3 Instrument Characteristics

The complete set of derived system characteristics is summarized in Table 3.3-2. The antenna system is a rotating, offset-fed, parabolic-mesh reflector, with two identical multichannel feedhorns. The two feedhorns provide separate beams that provide increased sampling and allow the antenna system to rotate half as fast as would be necessary with a single beam. The combined antenna and feed system rotates about the vertical axis, with antenna beams offset at ~36° from nadir, providing a wide-swath conical scan. As the spacecraft moves, the 3-dB antenna footprints provide overlap along and across track in a helical coverage pattern. The rotation rate of 6 rpm with two beams provides overlapping contiguous footprints at the surface. At an orbit altitude of 600 km, the 6-m antenna provides about 40-km spatial resolution, an incidence angle of about 40°, and a swath width of 900 km. (At an altitude of 800 km, the corresponding parameters are 56-km spatial resolution, 42° incidence angle, and 1200 km swath width.) A low orbit is preferred from the point of view of improved spatial resolution. However, at orbit altitudes lower than about 600 km atmospheric drag becomes a concern, requiring more attitude control and orbit maintenance and increased fuel.

Mission cost constraints require that the stowed volume of the instrument and spacecraft fit within a Taurus-class or smaller launch vehicle. The spinning antenna requires a spacecraft that either rotates with the antenna as a rigid body or is 3-axis stabilized and has a spinning platform on which the antenna is mounted. As discussed in Section 4, the large spinning antenna places demands on the spacecraft attitude control system to meet the requirements for pointing control and knowledge. The instrument mass and power estimates (obtained as discussed in Sections 5, 7, and 8 for the feedhorns, radar, and reflector/boom) are shown in Table 3.3-3. The mass and power estimates used by Spectrum Astro in their analysis (Appendix II) differ slightly from these due to additional S/C interface, margin, and uncertainty assumptions.

3.3.4 Data System

For a mapping system it is required that the antenna footprints of adjacent samples overlap at least at the 3-dB level both along and across track. This requirement determines the sensor sampling rate and the antenna scan rate for a given orbit altitude, antenna diameter, and number of beams. A preliminary analysis indicated that no more than two feedhorns could be easily accommodated on a small spacecraft since each feedhorn at L-band has a diameter of about 0.64 m. Figure 3.3-2 shows the design for the positions of the feedhorns, placed adjacent to each other with centers offset by 12 cm to either side of the scan line.

This feed placement provides the antenna footprint spacing shown, with centers offset by 17.25 km to either side of the scan line and a designed 25% overlap of the 3-dB footprints in the along-track direction. The footprints are shown as approximately circular since the radiometer integration time smears out the short dimension of the elliptical footprint in the cross-track direction to make the effective footprint shape of each sample approximately circular.

OSIRIS is a coarse-resolution system with a relatively low data rate. It is advantageous for the radiometer and radar data system to sample at a higher rate than required for 3-dB footprint overlap in the cross-track direction. The samples can then be averaged to obtain approximately co-registered footprints at all channels. Given these sampling design characteristics, the required antenna spin rate, sensor integration times and data rates were computed. The spin rate was determined as 6 rpm. The data rate calculation is shown in Table 3.3-4, giving a total data rate for the system of 25.6 Kbps.

22

Table 3.3-2. Key Baseline System Characteristics

Radiometer frequencies	1.41 and 2.69 GHz
Radiometer polarizations	H, V (1.41 GHz polarimetric, U)
Radar frequency	1.26 GHz
Radar polarizations	VV, HH,VH, HV
Antenna type	Offset-fed, parabolic, deployable mesh reflector
Aperture diameter	6 m
Nadir offset angle	36°
Number of feedhorns	2 (each L/S-band, V/H-pol)
Beamwidths	2.6° (approx. equal in all channels)
Antenna gain	> 35 dB
Beam efficiency	> 90%
Cross-polarization	< -18 dB
Orbit type	Polar, sun-synchronous, 6 am/6 pm
Altitude	600 km
Spatial resolution	35 × 45 km
Swath width	900 km
Rotation rate	6 rpm
Global coverage	3 days
Pointing control/knowledge	1.3°/0.1° (3σ)
Radiometer rms noise per pixel**	0.1 K
Radiometer calibration stability	0.2 K
Radar precision/stability	0.2 dB
Data rate	25 Kbits/sec
Launch vehicle	Taurus class
Mission duration	3 years

** Over ocean, 100 MHz bandwidth, averaging forward- and rear-view pixels. Over land, the bandwidths are reduced to 25 MHz and 10 MHz, respectively, to minimize radio-frequency interference.

Table 3.3-3. OSIRIS Baseline Instrument Mass and Power Summary[++]
(3-Axis-Stabilized Option)

	Mass (kg)	Power (W)
Mesh antenna and boom[+]	45	
Feedhorns[+] (2)	15	
Radiometer (front-end)[+]	5	24
Radiometer (back-end)*	10	20
Radar RF subsystem (front end)[+]	5	81
Radar digital subsystem (front-end)[+]	10	18
Radar digital subsystem (back end)*	10	30
Spin assembly**	50	20
Total	150	193

[++] Margin and uncertainy not included

[+] Spun side

* De-spun side

** Includes feed and electronics support structure and spin mechanism, but not momentum wheel assembly

Dual Feedhorn Array
Horn Diam ~64 cm

Focus at 36°
Pointing Angle

**OSIRIS 6-m Antenna Feeds
And Scan Pattern**
(for 40° Incidence Angle)

Footprint Pattern on Ground
Footprint Size = 46 x 49 km
Repeat Track Distance = 69 km
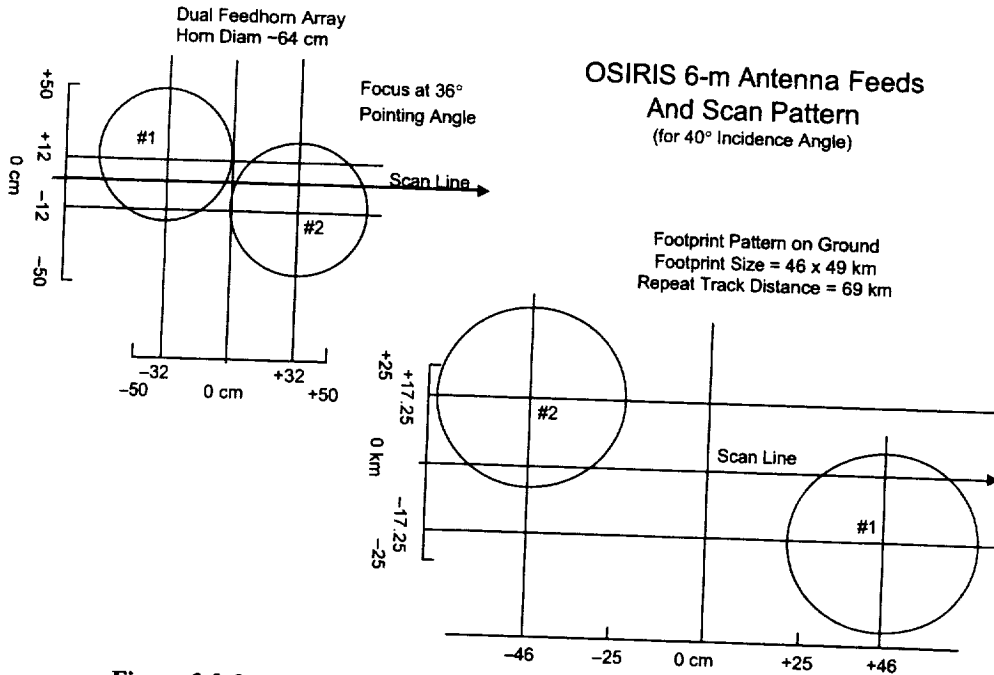
Figure 3.3-2. OSIRIS feedhorn placement and footprint spacing.

Table 3.3-4. Data Rate Calculation

Antenna spin rate	6 rpm
Sampling rate	100 Hz
Sample spacing along scan	2.83 km
Integration time per footprint	124 ms
Word length (includes overhead)	2 bytes
Number of radiometer channels	6
Number of radar channels	4
Number of beams	2
Radiometer data rate	19.2 Kbps
Radar data rate*	6.4 Kbps
Total data rate	25.6 Kbps (2.2 Gbit/day)

* Radar uses one beam only

Various scenarios were investigated to determine the data downlink and onboard storage requirements for the baseline system. The scenarios considered the OSIRIS orbit, data rate, and a desire to consider data latency as low as 6 hours, requiring as many as four downlinks per day. Three of these scenarios involved use of the NASA Wallops and Alaska ground stations. A fourth scenario considered use of Universal Space Network (USN), a commercial company that supplies tracking and operations services[1]. Table 3.3-5 summarizes the storage and telecommunications information for each of the scenarios.

---

[1] http://www.uspacenetwork.com

24

Table 3.3-5. Data Downlink Scenarios

	NASA/GSFC (4 pass/day)	NASA/GSFC (2 pass/day)	NASA/GSFC (1 pass/day)	USN (4 pass/day)
Data volume/day	2.2 Gbit	2.2 Gbit	2.2 Gbit	2.2 Gbit
Onboard data storage	0.6 Gbit	1.2 Gbit	2.2 Gbit	0.6 Gbit
Onboard bus data rate	1.2 Mbps	2.3 Mbps	4.6 Mbps	1.2 Mbps
Downlink data rate	1.2 Mbps	2.3 Mbps	4.6 Mbps	1.2 Mbps
Downlink frequency band	S-Band	S-Band	X-Band	S-Band
Data latency	6–7 hours	12–14 hours	24 hours	6–7 hours
Size of ground antenna	5 m	5 m	11.3 m	5 m

Figure 3.3-3 shows the downlink timing, and build-up and playback of data on the spacecraft solid-state recorder (SSR) for the 4-pass-per-day scenario. The top bar illustrates the continuous data acquisition by the radiometer and radar sensors. Each tick mark on the downlink bar indicates an available overpass of either the Wallops or Alaska ground station. There are more passes available than shown. Only the selected passes, spaced approximately 6 hours apart, are shown. The vertical axis on the lower graph shows the volume in Kbits. For this scenario, an onboard SSR storage of 0.6 Gbit and a 1.2 Mbps S-band link to a 5-m ground station antenna is sufficient. The cost is lower for a 2-pass-per-day scenario, but increases again at 1 pass per day due to the need to go to an X-band downlink for higher transmission rates. The cost of using the commercial USN system is comparable to the NASA system. The USN system uses ground stations in Alaska, Hawaii, or Perth, with backups through collaborative station partners in Kiruna, Santiago and South Africa. The study shows that there are 30–40 opportunities a day to track the OSIRIS spacecraft with the USN system.

3.4 ERROR ANALYSIS

3.4.1 Retrieval Simulations

Retrieval simulations were performed for SSS to verify that the system design could meet the stringent salinity accuracy requirements. The error analysis was based on a performance simulation tool that simulates L- and S-band radiometer and radar measurements for given satellite orbit characteristics, instrument design, and system performance, including antenna rotation rate, antenna beam pointing accuracy, and spacecraft attitude errors. Measurement errors include geophysical and system modeling errors, radiometer and radar signal detection noise, and sensor calibration errors. The key steps in the approach and the main results are presented here. Additional details are provided in Njoku et al. (2000) and Yueh et al. (2001).
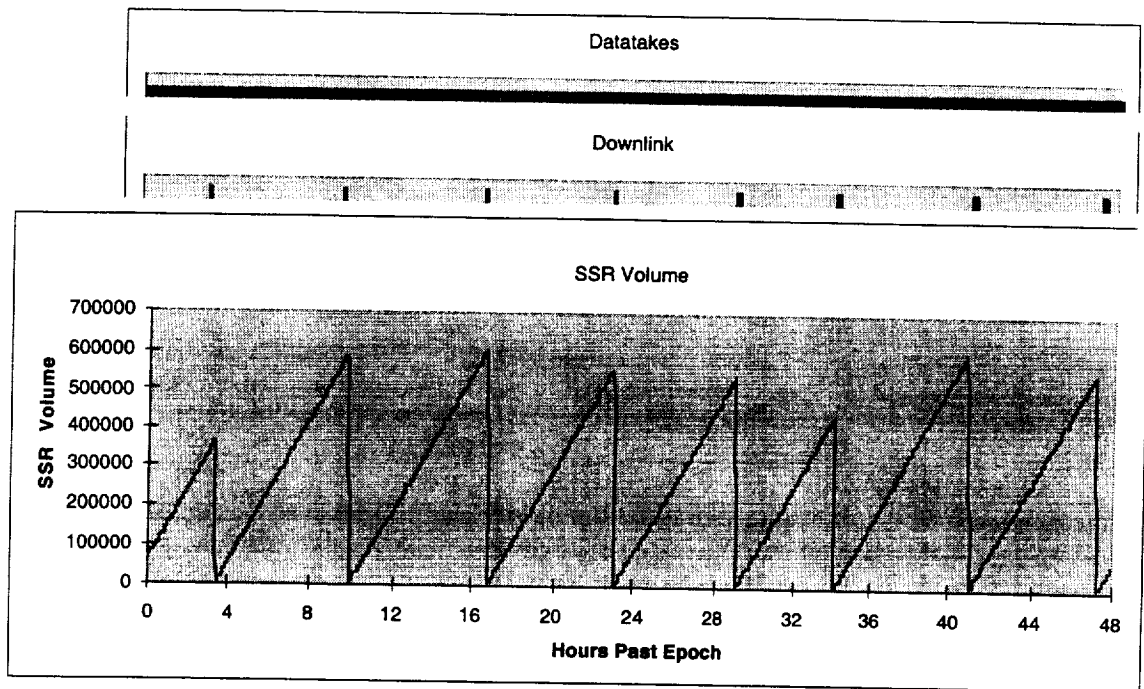
Figure 3.3-3. Data downlink and storage volumes for 4 passes/day scenario.

Using climatologies of SSS and SST, wind speeds from ECMWF (European Centre for Medium-range Weather Forecasting) analyses, and SSM/I (Special Sensor Microwave/Imager) monthly-averaged atmospheric water vapor and cloud liquid water paths as input fields, simulated radiometer and radar measurements were computed for incidence angles of 40° and 45°. The errors assumed in the analysis are given in Table 3.4-1. These are target values based on best estimates of what is achievable using current technology and the OSIRIS sampling approach. The errors for the radiometer data consist of three terms including the noise equivalent delta-T (ΔT_n), the geophysical modeling error (ΔT_m), and the calibration error (ΔT_r). The radiometer design under consideration is a total power radiometer with ΔT_n determined by the system noise temperature normalized by the square root of the time and bandwidth product. The geophysical modeling error ΔT_m includes errors in modeling the effects of sea surface roughness, atmospheric attenuation, and the ionosphere. ΔT_r represents the time-varying portion of the system calibration errors. Similarly, there are three error terms considered in the simulated radar data, including signal detection noise (Kp_c), geophysical modeling error (Kp_m), and the calibration error (Kp_r). These Kp terms are defined as the percentage errors in the radar backscattering coefficients.

All the error terms were assumed to be Gaussian with zero mean. Constant calibration bias offsets were assumed to be removable by adjustment to in situ calibration data. To account for the time-varying characteristics of the calibration errors, ΔT_r and Kp_r were modeled as first-order Markov random processes with correlation time τ. Assuming a nominal orbit altitude of 600 km, the spacecraft travels about 1600 km in 4 minutes. Thus, for a correlation time of 4 minutes or greater, the fore- and aft-look measurements of any pixel within the swath are correlated. For our analysis, we assumed a correlation time of 4 minutes for ΔT_r and Kp_r. Should a smaller

26

Table 3.4-1. Error Characteristics Assumed in the SSS Retrieval Simulations

(a) Radiometer errors

Spatial Resolution	ΔT_n (K)	ΔT_m (K)	ΔT_r (K)	RSS ΔT (K)
50 km	0.07	0.2	0.2	0.29
100 km	0.035	0.1	0.2	0.23

(b) Radar errors

Spatial Resolution	Kp_c (dB)	Kp_m (dB)	Kp_r (dB)	RSS Kp (dB)
50 km	0.2	0.2	0.2	0.35
100 km	0.1	0.1	0.2	0.24

ΔT_n = radiometer instrument noise, ΔT_m = radiometric geophysical modeling error, ΔT_r = radiometer calibration error. Kp_c = radar instrument noise, Kp_m = radar geophysical modeling error, Kp_r = radar calibration error. Cases for two spatial resolutions, 50 and 100 km, are shown.

correlation time be assumed, such that the fore- and aft-look calibration errors are uncorrelated, then the contribution of these errors will be reduced by averaging the two independent estimates. ΔT_m and Kp_m were treated as spatial random processes with correlation length of 50 km. The terms ΔT_n and Kp_c were assumed to be random from sample to sample. The magnitudes of the simulated errors are summarized in Table 3.4-1 for data averaged within 50- and 100-km square bins.

The simulated noisy sensor data were processed using a conjugate-gradient method to retrieve SSS and SST by minimizing a normalized least-square measure. The error measure is defined as the weighted sum over the measurement channels of the squared differences between the simulated noisy sensor data and the noise-free model data, with the weights determined by the total variance of the sensor and geophysical noise. The method was implemented to find the set of geophysical parameters that minimized the error measure. The retrieved parameters were averaged over a 7-day (weekly) period on a $1° \times 1°$ lat-lon grid (~100 km spatial resolution) for one set of input fields for the month of May.

The weekly-averaged retrieval results are shown in Figure 3.4-1 as a set of color maps showing the global distributions of SSS and SST. The figure shows the input ("true") fields, the retrieved fields, and the differences ("delta") between the fields, for a 40° incidence angle. (The errors are similar at 40° and 45° incidence angles.) Comparing the retrieved fields with the true fields, it is seen that the main features of the SSS and SST fields are correctly retrieved. The difference maps exhibit vertical striations that reflect the effects of the assumed noise and calibration errors in the data (which consist of several overlapping swaths). There is a combination of the effects of time-correlated errors within each swath and error-reduction by averaging of data with uncorrelated errors where different swaths overlap.

27
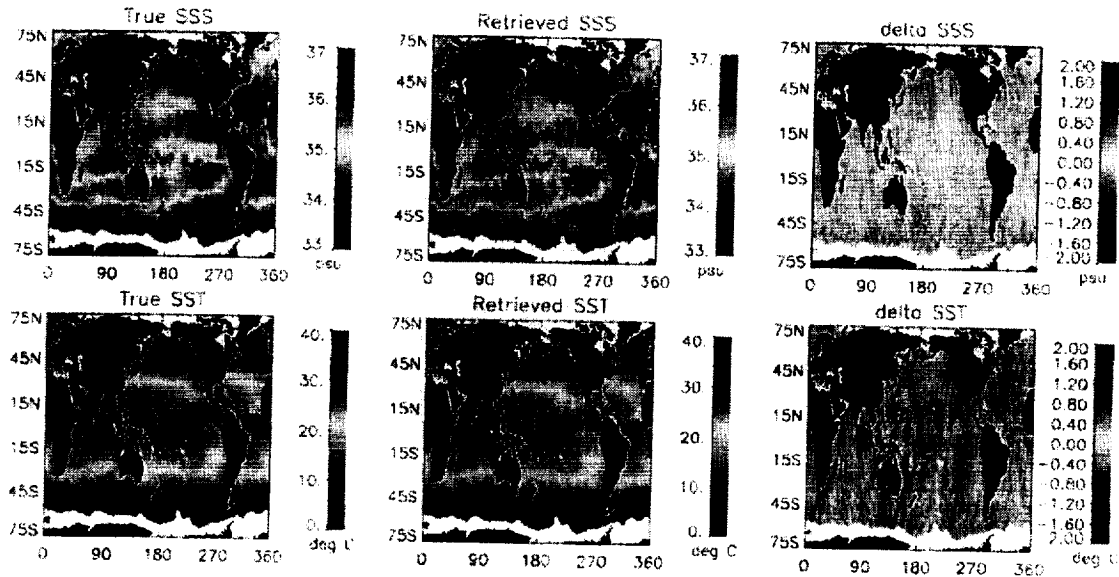
Figure 3.4-1. Weekly-averaged retrieval results showing global distributions of SSS and SST.

The SSS rms retrieval errors are shown in Figure 3.4-2 for 20° latitude bands at a 40° incidence angle. At higher latitudes the retrieval errors are greater because the sensitivity to SSS decreases as SST decreases. Including the L-band radar in the retrieval reduces the rms error by 0.05–0.1 psu. The improvement comes from the enhanced correction for surface roughness. The improved accuracy and extra capabilities contributed by the radar must, however, be traded against the increased cost of the system. The results of these simulations show that for 100 km spatial resolution and 1-week averaging the salinity measurements are expected to have errors of ~0.15 psu in the tropics and sub-tropics and ~0.3 psu in sub-polar regions. It is expected that additional accuracy can be realized with further space-time averaging, and by co-analysis with in situ surface data, to resolve weaker signals on longer time scales. This suggests that this instrument concept can meet the target measurement requirements if the assumptions for instrument noise and calibration errors of Table 3.4-1 are reasonable. Thus, we find that to achieve the required accuracy for SSS, a radiometer with rms noise (ΔT) of 0.1 K per pixel and calibration stability of 0.2 K is adequate. In addition, a radar backscatter calibration stability of ~0.2 dB is required. These requirements have been derived for an incidence angle in the range of 40–45°. It is assumed that bias effects on the geophysical retrievals due to absolute accuracies of ~1 K and ~1 dB for the radiometer and radar, respectively, can be removed by post-launch adjustments to in situ calibration references.

Also shown in Figure 3.4-2 are the simulated rms errors for an L/S-band cross-track-scanning radiometer. Only the two outer 300–600 km portions of the swath (corresponding to approximately 25°–45° from nadir) were used in the simulations. This is because closer to nadir the difference between horizontal and vertical polarized emission decreases, and the polarization

28

Salinity Retrieval Simulation (7 Days of Data)
L-/S-Band Radiometer and L-band Radar
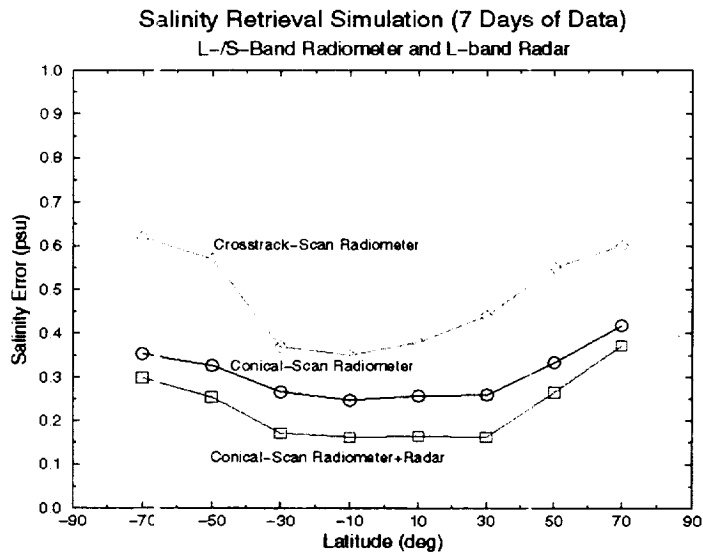
Figure 3.4-2. SSS rms retrieval errors for 20° latitude bands
at a 40° incidence angle.

difference provides less information for correcting surface roughness. Even by restricting the swath to these angles, the retrieval error is significantly degraded over the conical-scan case. This indicates the significant benefit of the conical-scan configuration for salinity sensing.

A simulation was also performed to determine the sensitivity of the retrievals to characteristics of the sensor calibration errors. This simulation assumed a calibration error correlation time of 8 seconds as compared with the earlier assumed correlation time of 4 minutes. The shorter correlation time resulted in a significant reduction of retrieval error due to the increased number of independent samples in each 1° × 1° box within a given swath. This suggests that estimating and reducing time-correlations in the calibration error will be of major benefit to salinity sensing.

3.4.2 Error Budget

To assess how the assumed calibration accuracies could be realized in practice, a calibration budget was developed as shown in Table 3.4-2. It is assumed that the absolute calibration bias can be corrected by empirical comparisons of radiometer and radar observations with in situ data through adjustment of the geophysical model functions. The geophysical retrieval performance is then limited by the temporal stability of the calibration. Errors due to non-ideal antenna patterns can be limited to less than 0 1 K for beam efficiencies of greater than 90%. The mesh reflector shaping and support structures are constructed of composite temperature-insensitive materials that are thermally stable in orbit. An antenna beam-pointing error of 0.1° should be feasible. (Note that in Tables 3.3-1 and 3.3-2 this requirement is expressed as a 3σ value to provide margin. It can be relaxed to a 1σ requirement, however.) The accuracy of 0.01° for spacecraft attitude can be achieved using star trackers.

An internal reference load and highly stable noise diode source are used for the radiometer calibration. An internal calibration loop is used for the radar. The stability of noise diodes for

29

Table 3.4-2. Calibration Requirements Summary

Parameter	Stability (1 sigma)			Bias (3 sigma)		
	Parameter Error	Radiometer (K)	Radar (dB)	Parameter Error	Radiometer (K)	Radar (dB)
Antenna beam gain and pattern		0.1	0.15		2	0.7
Antenna beam pointing	0.1°	0.15	0.1	0.3°	0.45	0.3
S/C attitude	0.01°	0.02	0.01	0.03°	0.05	0.03
Calibration noise source	0.1 K	0.1	0	1 K	1	0
Radar calibration loop	0.05 dB	0	0.05	1	0	1
Waveguide/coax cable loss	0.05 dB	0.05	0.01	0.1 dB	0.1	0.1
RSS		0.2	0.19		2.5	0.9

radiometer calibration has been demonstrated as part of the JASON (TOPEX follow-on) microwave radiometer development. The stability of the radar calibration loop has been demonstrated by testing of the SeaWinds/Quikscat scatterometer (NSCAT follow-on) launched in June 1999. Taking only the above factors into account, the RSS calibration stability requirements of 0.2 K and 0.19 dB for the radiometers and radar, respectively, appear challenging but feasible.

The effects of additional losses in the antenna reflector and feed horns must be considered, however. As shown in Section 6, the finite (non-zero) emissivity of the reflector mesh, and the uncertainty in the physical temperature of the mesh in orbit, will give rise to a small but significant noise term of a few tenths K. The implications of this for the OSIRIS salinity and soil moisture measurements are discussed further in Section 6.

3.4.3 Geophysical Errors

The geophysical modeling error of $\Delta T_m = 0.2$ K assumed in Table 3.4-1 is also a challenging target. This is a requirement on relative and not absolute error, and is related to the error in modeling geophysical variability. To estimate the feasibility of this target for salinity sensing, the contributing geophysical error sources and their impact on the retrievals must be considered. A detailed analysis of the error sources performed in this study has been published in the paper by Yueh et al. (2001).

Table 3.4-3 lists the major geophysical variability effects on the relationship between brightness temperature and SSS at L-band. The symbols indicate which effects can potentially be corrected in retrieving SSS. The effects on retrieving soil moisture are also listed. Minor effects influence the brightness temperature by less than a few Kelvins and can be modeled and removed accurately using ancillary data or climatological knowledge. Major effects require either multichannel information or ancillary data from other sources to implement a correction in the retrieval algorithm.

Table 3.4-3. Geophysical Effects on the Relationship Between Brightness Temperature and Sea Surface Salinity and Soil Moisture

Effect	Salinity	Soil Moisture
Rain	x	x
Solar radiation	x	x
Radio-frequency interference	x	x
Galactic emission	x	+
Atmospheric gases	+	
Clouds	+	
Faraday rotation	o	o
Surface temperature	o	o
Surface roughness	o	o
Vegetation		o
Soil texture		+

x   Major effect, uncorrectable. Flag and reject.
+   Minor effect, correctable using ancillary data.
o   Major effect, correctable using multichannel retrieval or ancillary data.

Rain, solar radiation (either entering the antenna sidelobes directly or reflected off the ocean surface), radio-frequency interference (RFI), and galactic-center emission have large L-band brightness temperature signatures which cannot be modeled or measured accurately enough for correction. The presence of these interferences can be detected (or inferred from geometrical considerations in the case of solar and galactic radiation) so that the contaminated data can be rejected from the data stream. Only a small fraction of the data should require rejection due to these causes. RFI is likely to cause the most data rejection over land, while reflected solar radiation will likely be the cause for most data rejection over ocean. The effects of atmospheric water vapor and most clouds on brightness temperature at L-band are small and can be estimated using ancillary data from operational weather satellites. The residual uncertainty in brightness temperature due to these effects is estimated as less than 0.1 K. Ancillary data can also be used to identify and reject the small percentage of cases where clouds of very high liquid water content, extending over a large fraction of the footprint, may be contaminating the data to an unacceptable degree.

Uncertainties in the surface emissivity model affect the accuracy with which surface temperature and surface roughness effects can be corrected. However, for the ocean surface at L-band the effects of wind-induced roughness and foam are small. In the multi-polarization L-band (passive and active) retrieval approach, where the appropriate roughness scale is being directly sensed and corrected, an uncertainty of 0.15 K is considered reasonable. This uncertainty is expected to be significantly larger if ancillary data on wind speed or roughness, such as from a K-band satellite radar measurement, has to be used instead of a multichannel L-band correction. K-band radar measures a smaller capillary-wave roughness scale that is not directly related to the longer L-band roughness scale (being dependent also on fetch and duration) and may introduce additional error.

The effects of Faraday rotation have been evaluated for the orbit and scan configuration described here. A pre-dawn equator crossing and Sun-synchronous orbit are desirable to minimize the

ionospheric effects. By using the sum of the vertically and horizontally polarized channels (which is insensitive to Faraday rotation) or by providing an additional polarimetric channel in the radiometers, it should be possible to reduce the uncertainty due to Faraday rotation to less than 0.1 K (Yueh, 2000). Combining the effects of uncertainties due to atmospheric variability, surface emissivity, and Faraday rotation, the RSS target of $\Delta T_m = 0.2$ K appears achievable.

3.5 CONCLUSIONS

Science requirements for ocean salinity and soil moisture were derived from recent NASA workshop reports and planning documents and used to develop the baseline instrument concept. A set of detailed system characteristics were derived, including antenna geometry and rotation rate, frequencies, polarizations, antenna beam specifications, feedhorns, orbit type, altitude, swath width and coverage, pointing control, receiver sensitivity and calibration accuracy, and data rate. These system parameters were used as the baseline for the other subtasks of the study. The antenna design included positioning of the two feedhorns to achieve the required footprint scan pattern overlap. A data downlink study was performed to investigate the trade-offs between data latency, on-board storage, bus data rate, and the cost of tracking and level 0 processing.

A detailed retrieval analysis was done for ocean salinity to determine the requirements on measurement sensitivity and accuracy of the radiometer and radar, antenna beam characteristics, and pointing knowledge and control. An error budget was developed for use in other parts of the study. The retrieval analysis showed that the system is capable of achieving the required 0.2 psu SSS accuracy (at a weekly, 100-km scale) if the stringent requirements imposed on instrument sensitivity and calibration stability can be met, and a detailed accounting of geophysical error sources is included in the retrievals. The key requirement for SSS is a radiometric error, including instrument noise, geophysical modeling error, and calibration error of better than ~0.3 K at 50-km resolution. The non-zero emissivity of the mesh reflector (discussed in Section 6) may cause the calibration error to exceed the feasibility limit for salinity sensing if the physical temperature of the mesh cannot be characterized adequately in orbit. For soil moisture, the system is more than capable of meeting the required 0.04 g cm^{-3} accuracy since the required radiometric error for soil moisture is ~1 K.

4. CONCEPT DEFINITION

As part of the first phase of the project, Science Applications International Corporation (SAIC) was tasked to assist in the development of the OSIRIS flight system based on the identification and system-level evaluation of candidate antennas, spacecraft and launch vehicle configurations. It was clear that development of such an "optimized" system design must give consideration to numerous key attributes/functional characteristics of each of the system elements, and consequently the SAIC effort was partitioned into the following task functions in which these various items were addressed:

- Identification and Evaluation of Deployable Mesh Antenna Concepts – including a review of mission-driven antenna requirements as well as a review and evaluation of the functional and physical characteristics of candidate mesh antennas regarding their suitability to the mission requirements. These characteristics include antenna size and geometry (both stowed and deployed), mass, deployment technique and envelope, compatibility with potential spacecraft and feed interfaces, and maturity of the antenna technology. (Evaluation of other antenna reflector characteristics such as surface precision, thermal stability and the impact of the desired rotation rate on surface and alignment accuracy were addressed in other parts of the task.)

- Identification and Evaluation of Low-Cost Candidate Spacecraft and Launch Vehicles – including a survey of available spacecraft and launch vehicle services that, with minimal modification to accommodate the candidate antennas, feeds and mission requirements, might be purchased at costs that do not force the mission to exceed the given budget constraints. The spacecraft survey examined the configuration, dimensions, interfaces, power, communications and other pertinent resources of small commercial satellite buses identified in the catalog of the Rapid Spacecraft Development Office (RSDO) of NASA Goddard Space Flight Center. The launch vehicle survey examined low-cost options for delivery of the OSIRIS payload to Sun-synchronous orbit and focused on launch vehicle payload-to-orbit capacity, shroud size, and dynamic envelope.

- Development of "Optimized" Antenna, Spacecraft, and Launch Vehicle Configuration – including the definition of criteria and the analyses required to compare different candidate system configurations and options. These analyses included an examination of trades associated with spin rate and orbital coverage, and a comparison of ACS requirements for two different OSIRIS configurations (rigid body spinner and three-axis-stabilized).

The antenna/configuration selection criteria are presented below in roughly prioritized order. Developed jointly by the OSIRIS team, they provided SAIC with a set of basic guidelines for arriving at a preferred system configuration.

- Low Total Mission Cost
- Compatibility of Stowed Antenna, Spacecraft Bus and Launch Vehicle
- Adequate Spacecraft Controlability
- Satisfies Constraints on Reflector Distortion and Feed Alignment
- Satisfies Resolution, Accuracy, Coverage Requirements.

Not all of the listed criteria were addressed fully by SAIC during the first-year study period. The development of dynamic simulations of candidate configurations (to demonstrate sufficient

spacecraft stability and control) was deferred to the industry studies performed during the second year (Section 8). A report of the SAIC study covering the period March 17 to September 30, 1999 was provided to JPL. The main parts of the report are reproduced below.

4.1 ANTENNA

Information on candidate deployable-mesh antennas was obtained from a survey of antennas manufactured by the two leading industrial vendors, TRW and Harris Corporation. From this survey, the current sizes, scalability, and estimated technology readiness levels (TRLs) (see Appendix III) of the antennas were estimated, and are listed in Table 4.1-1. Examples of these antennas are shown in Figure 4.1-1. The TDRSS antenna as shown is center-fed, and has unacceptable blockage of the main beam for radiometric applications. However, all three structural types (radial rib, double-articulated radial rib, and perimeter truss) can be configured as offset-fed parabolic reflectors as required for OSIRIS.

Table 4.1-1. Deployable Mesh Antennas

	Type	Manufacturer	Diameter (m)	Scalability (m)	TRL
TDRSS	Radial Rib	TRW	5	10	4/5
PAMS	Double Articulated Radial Rib	TRW	10	25	5
AstroMesh	Perimeter Truss	TRW	12.25	25+	8
PTR Concept	Perimeter Truss	TRW	2	25+	2/3
TDRSS	Radial Rib	Harris	5.5	25	6
DTS	Double Articulated Radial Rib	Harris	12–15	25	8
Heritage	Radial Rib	Harris	15	25+	9

Of the antennas listed, three were identified as being of primary interest based on design maturity. These were the AstroMesh perimeter truss, the TDRSS/Heritage radial rib, and the DTS double-articulated radial rib. Stowage length concerns eliminated the simple radial rib design. Although the Harris DTS appeared to be a viable concept, detailed models and other information on this antenna, for evaluation of potential thermal and mechanical distortions, was not readily available from the vendor. On the other hand, detailed information on the AstroMesh antenna was readily obtainable. Being a perimeter-truss design, the AstroMesh antenna has the stiffness required for a spinning configuration, and was in fact designed originally for a spinning application. For these reasons, subsequent analyses in the study were limited to the AstroMesh antenna.

The AstroMesh perimeter-truss design stows in a compact volume, has been flight qualified, and a 12.25-m version was launched and deployed successfully on the geosynchronous telecommunications satellite Thuraya-1 in November 2000. TRW provided detailed information on their 6-m AstroMesh design regarding the stowed configuration, the stowed cradle, and the deployment sequence. Based on the information provided, the AstroMesh perimeter truss appeared to be the lowest risk option for this study, and is the most compatible antenna given the volume constraints.
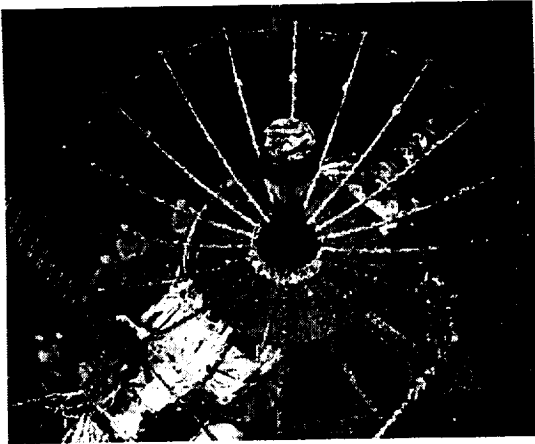
(a) Harris TDRSS radial rib
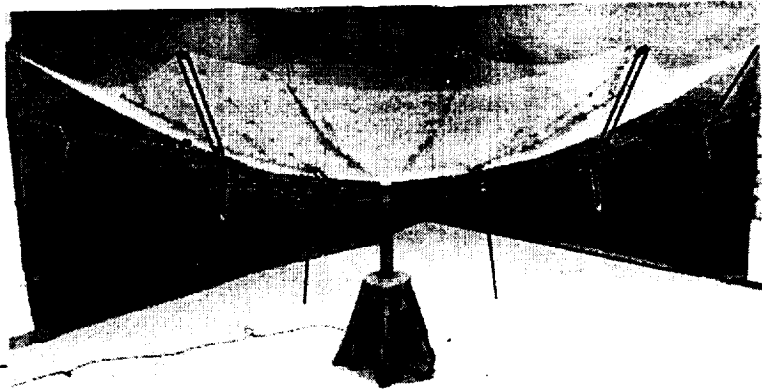
(b) Harris DTS double-
articulated radial rib
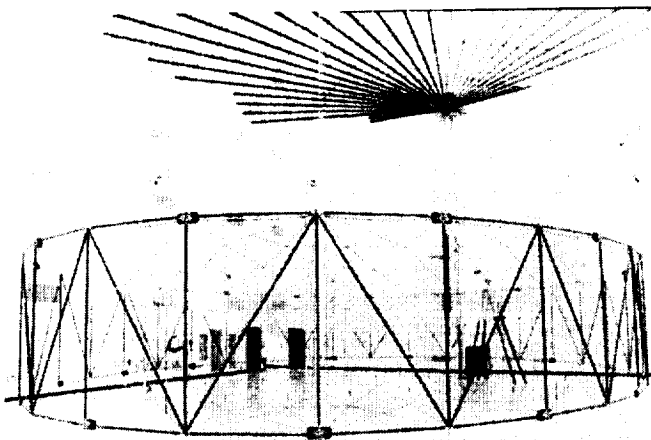
(c) TRW AstroMesh perimeter truss

Figure 4.1-1. Deployable mesh antenna designs (courtesy of Harris Corp. and TRW Astro).

35

4.2 SPACECRAFT AND LAUNCH VEHICLE

With low-cost future mission considerations in view, a low-cost, lightweight, nearly off-the-shelf spacecraft bus was required to accommodate the relatively unique OSIRIS instrument. The spacecraft bus must be small enough to allow the payload, especially the 6-m antenna, to be stowed within the launch vehicle usable envelope, and yet it must be capable of rotating the payload at the nominal spin rate of 6 rpm. The bus may spin itself, or may be 3-axis-stabilized and spin the payload on a platform.

A survey of potential launch vehicles confirmed the selection of a standard Taurus with a 92-in. fairing as the most feasible and cost-effective. Available launch vehicles were compared based on mass performance to a 600-km Sun-synchronous orbit, available payload volume within the fairing, and cost. Only the Delta and Taurus (92-in. fairing) vehicles demonstrated sufficient mass performance and fairing size for this mission. Of these two choices, the Taurus is nearly 30% cheaper, and therefore was the launch vehicle selected for further study.

Spacecraft bus candidates were evaluated based on payload requirements and launch vehicle constraints. The choice of antenna (AstroMesh) was an important step toward bus selection because it determined the bus volume capable of being accommodated on the launch vehicle. Most of the bus candidates were selected from the NASA RSDO catalog which contained 23 spacecraft buses from eight manufacturers. Additionally, a Hughes 376-Class Spinner was considered. Of these 24 potential candidates, seven were considered in some detail. These are listed in Table 4.2-1.

Table 4.2-1. Evaluation of OSIRIS Bus Candidates

Spacecraft Bus	LV Compatibility	Payload Compatibility	Flight Heritage
RS2000	Too Heavy	With Modifications	Significant
HS-376	Too Large	Very Compatible	Excellent
LM100	Too Large	Very Compatible	Very Good
LS-400S	Compatible	Significant Modifications	Some
LEOStar	Compatible	Significant Modifications	Significant
SA-200	Compatible	With Modifications	Significant
SSTI Core	Compatible	With Modifications	Significant

Launch vehicle constraints eliminated the LM100, HS-376, and RS2000 buses. The HS-376 and the LM100 had diameters that would not fit in the fairing and the RS2000 bus was too heavy for the launch vehicle given our mission. The LS-400 and LEOStar were eliminated because of the constraints implied by the instrument payload. Both buses would have required significant modifications and it was determined, based on the remaining candidates, that the risks associated with these modifications were excessive.

The remaining candidates were from TRW and Spectrum Astro. The TRW SSTI Core bus was considered a primary candidate. It was presented as a three-axis bus but had been modified previously to fly as a spinner and was less expensive as a spinner. Therefore, it was capable of performing as the bus for OSIRIS regardless of the decision to fly as a spinner or not. It had a structure that could be easily modified for the payload shelf and was narrow enough to allow the antenna to be stored in a cradle on the side of the structure. Figure 4.2-1 shows the SSTI Core Bus with the payload shelf and deployed antenna. The stored configuration is demonstrated in

36
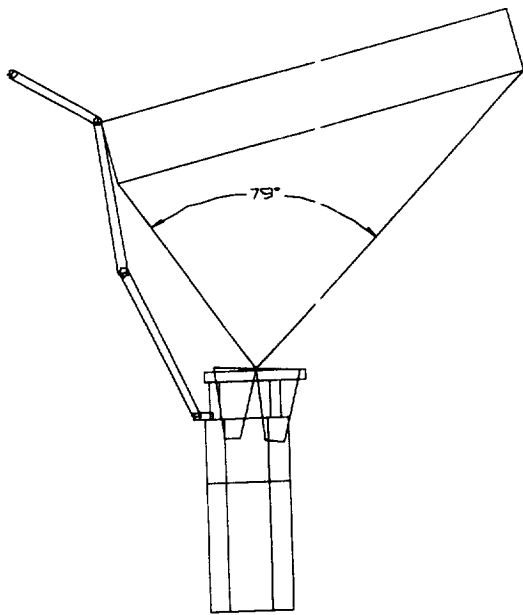
Figure 4.2-1. SSTI Core bus and payload shelf fully deployed.
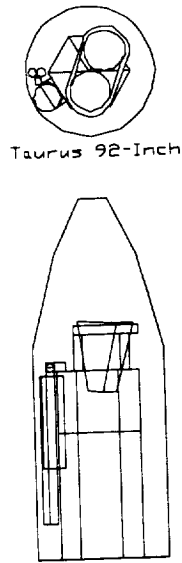
Figure 4.2-2. SSTI Core bus and payload stowed within Taurus fairing.
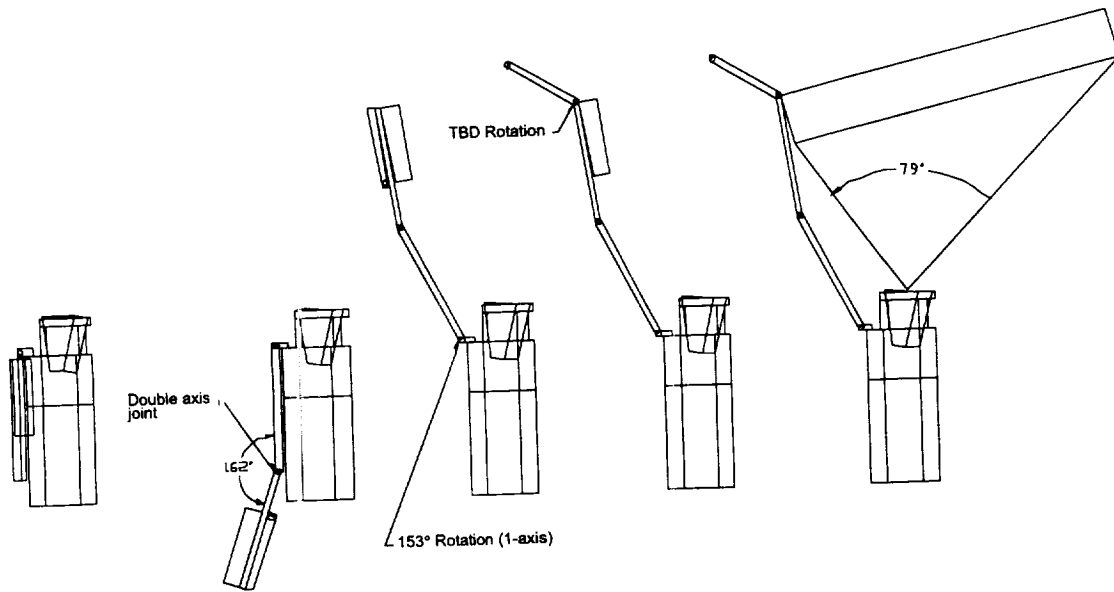
Figure 4.2-3. Proposed deployment sequence.

Figure 4.2-2. Figure 4.2-3 shows the deployment sequence. The Spectrum Astro SA-200 class spacecraft bus was also considered very capable in the three-axis mode. This type of bus is performing a similar mission for the Coriolis program. The SA-200 was considered a solid choice as a three-axis-stabilized bus.

37

4.3 SYSTEM CONFIGURATION

Several trade studies and analyses were performed to support the development of a preferred configuration for the OSIRIS flight system. These included trades relating to orbital coverage and spin rate, alternative spacecraft/antenna configurations, analysis of attitude control system (ACS) requirements for both rigid body spinner and 3-axis-stabilized configurations, estimation of spacecraft and mission costs, and a qualitative comparison of both candidate configurations with respect to a full range of subsystems and design criteria.

4.3.1 Orbital Coverage Analysis

An analysis was performed to evaluate the effects of the many space system options on mission success. A spreadsheet tool was developed to perform the analysis, incorporating orbit parameters and payload design options, utilizing a non-spherical Earth model. The primary output parameters of interest included the lowest possible spacecraft spin-rate for a particular configuration, the expected spacecraft eclipse periods, and the footprint and coverage characterizations. Additionally, simulations were run to demonstrate the footprint motion in relation to the sub-satellite point, and these simulations identified coverage gaps for several of the scenarios studied. The spreadsheet generated accurate descriptions of the footprints of the payload used by OSIRIS. The footprint size and shape were documented, along with the distance from the sub-satellite point to the center of the footprint. Important parameters such as the range of the beam and the incidence angle of the beam were presented for further analysis. Many of these parameters were used to create simulations of the footprint motion.

Several simulations were run in Matlab to characterize the relative motion of the footprints with the sub-satellite point. Figure 4.3-1 shows a typical simulation result for the two-beam configuration. Both forward and reverse sweeps are shown and the blue (darker) ellipses represent the outermost beam. The simulation begins with the sub-satellite point at the origin and progresses in a positive direction down the x-axis. Other simulations were run to evaluate the impact of varying antenna spin rates on the footprint overlap and coverage. The 6-rpm rate was confirmed as optimum. However, slowing the spin rate by as much as 0.7 rpm, with significant momentum savings, resulted in only small gaps in coverage that could most likely be tolerated in an actual science mission.

4.3.2 Spacecraft and Antenna Configuration

In the preliminary design (Section 3) the OSIRIS baseline configuration placed a 6-m TRW AstroMesh antenna above the spacecraft and used a 3-axis-stabilized spacecraft bus with antenna and feeds placed on a spinning platform. SAIC reopened the spacecraft configuration trade space by examining all workable configurations, i.e., any configurations were allowed that satisfied the following properties:

- The antenna must be either horizontal or vertical to the ground. Given the required incidence angle and the fact that antenna spins about nadir, there are only two possible ways to orient the antenna with respect to the ground.

- There are three optimum locations for the spacecraft relative to the antenna/feed/boom geometry. To keep spacecraft inertia balanced about the spin axis, the bus should lie on the eigenlines from the antenna/feed/boom center-of-gravity.
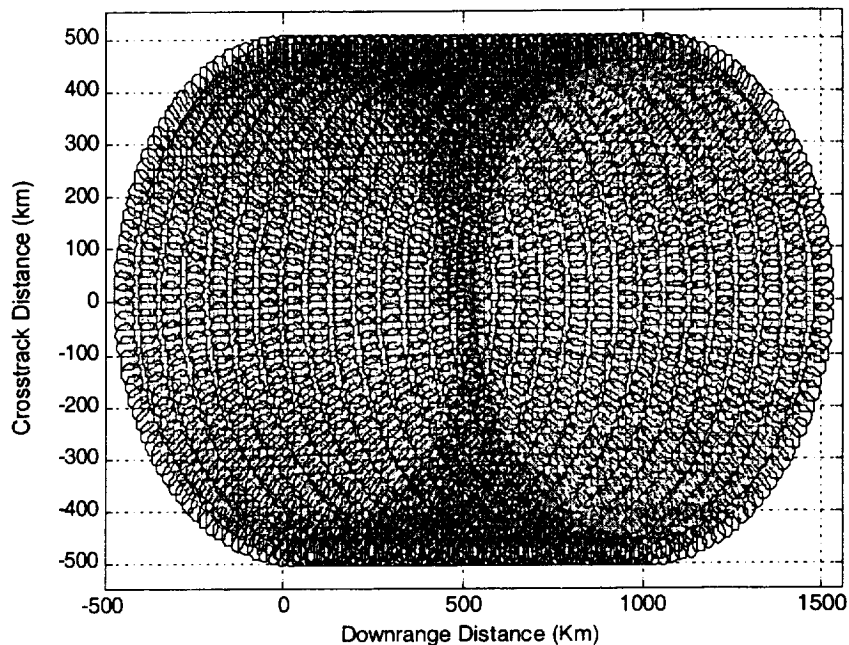
Figure 4.3-1. Simulation of beam footprint motion.

- The spacecraft bus can be either a rigid spinner or 3-axis-stabilized with antenna and feed mounted on a rotating platform. We did not allow separate spinning platforms for the antenna and feeds due to the unreasonable complexity of that design.

Given the above properties it was straightforward to identify 12 possible configuration options as shown in Table 4.3-1. The following criteria were then used to eliminate all but two of the configurations.

- Design simplicity, i.e., minimum number of deployment articulations, simple deployment mechanisms, naturally balanced spacecraft design, etc.

- Minimum ACS requirements, i.e., minimizing spacecraft inertia, minimizing spin axis inertia, passively stable design.

- Design flexibility, i.e., a preferred antenna/feed/bus layout should be flexible to future decision changes. These decisions can include using or not using a spinning platform, for example.

- Environmental impacts, i.e., mesh temperature, solar leakage to feed horns, environmental momentum.

- Relative comparison, i.e., we compared remaining designs in order to eliminate designs that passed all of the above criteria but were overall inferior to another design.

39

Table 4.3-1. Summary of Spacecraft Configuration Trades

Decision Criteria	Criterion Components	3-axis stab.	rigid spinner	3-axis stab.	rigid spinner	3-axis stab.	rigid spinner	3-axis stab.	Rigid spinner	3-axis stab.	rigid spinner	3-axis stab.	rigid spinner
Design simplicity	Number of deployments	✓	✓				✓		✓	✓	✓		✓
	Simplicity of feed horn mounting	✓	✓				✓		✓	✓	✓		✓
	Number of mechanisms	✓	✓	✓			✓		✓	✓	✓		✓
	Naturally balanced spacecraft design	✓	✓	✓			✓		✓	✓	✓		
Minimum ACS requirements	Minimizing spin axis inertia	✓	✓	✓	✓					✓	✓		
	Minimizing spacecraft inertia	✓	✓	✓	✓				✓	✓	✓		
	Control authority	✓	✓	✓	✓					✓	✓		
Design flexibility	Flexibility of the antenna/ feed/ bus layout to future decision changes (e.g., using or not using a spinning platform)	✓	✓	✓	✓		✓		✓		✓		
Environmental impacts	Solar leakage to feed horns	✓	✓	✓	✓		✓		✓	✓			✓
	Environmental momentum	✓	✓										
Relative Comparison		Yes	Yes										
Final Decision		Yes	Yes	No	No	No	No	No	No	No	No	No	No

40

Table 4.3-1 summarizes the configuration down-selection process. The two designs that appear most promising place the antenna above the spacecraft and oriented horizontally to the ground. They differ only in the spacecraft—one using a rigid body spinner and the other a non-spinning, 3-axis-stabilized bus with a spinning platform.

4.3.3 Attitude Control Requirements

SAIC performed a first-order attitude control system analysis for the OSIRIS system to identify potential ACS issues. The ACS requirements are listed in Table 4.3-2. Preliminary error budgets were also prepared for both the rigid spinner and 3-axis-stabilized designs. Preliminary torque and momentum analyses were performed independently by both SAIC and by Dr. Don Wang of JPL. The OSIRIS spacecraft needs to operate around zero-net momentum, otherwise the ACS would have to expend 55.44 kg/day of propellant. To operate at zero net momentum, the OSIRIS spacecraft must carry a large momentum wheel to counteract the 6-rpm rotation of the spacecraft and antenna in the rigid spinner configuration, or antenna only in the 3-axis-stabilized case. The momentum storage requirement is most likely to be in the range from 120 N-m-s (3-axis) to 200 N-m-s (spinner).

Table 4.3-2. OSIRIS ACS Requirements

Requirement	Description[1]
Pointing Accuracy	*1.2 deg beam radial angle accuracy*
	Beam radial displacement from the nadir should be controlled to 1.2 degrees (3σ).
	0.1 rpm spin rate accuracy
	Beam spin rate should be controlled to 0.1 rpm (3σ) with respect to the inertial frame.
Pointing Knowledge	*0.1 deg attitude knowledge*
	Beam attitude should be known to 0.1 degrees (3σ) with respect to the orbit frame.
Torque Authority	Spacecraft ACS actuators shall have enough torque authority to counteract environmental torque (GG, solar radiation, magnetic, aerodynamic), internal torque (flexible modes, thermal gradients), and dynamic torque (gyroscopic).
Momentum Storage	ACS momentum wheel shall be capable of storing all rotational momentum, making the overall spacecraft zero-momentum biased nominally.
	ACS reaction wheels and momentum wheel shall be capable of storing environmental torque and absorb momentum due to spacecraft geometry and mass property uncertainties.

[1]The pointing accuracy and knowledge requirements were to-be-reviewed (TBR). Their values would be reviewed in Phase A studies.

Analysis of environmental forces (i.e., solar pressure and aerodynamic torque) showed that a large amount of momentum would be dumped into the momentum control system, basically the momentum wheels. This is due to a large separation between the center of pressure and the spacecraft center of gravity. Using magnetic torquers to continuously dump momentum would still leave about one-fourth of the orbit momentum. For the rigid spinner configuration, this implies that the reaction wheels must have a large torque authority (0.3–0.6 N-m) to precess

accumulated momentum at 6 rpm. For the 3-axis-stabilized spacecraft, the precession rate is the orbit rate, i.e., 1/90 rpm. Hence, the required torque authority is smaller.

Whereas the ACS issue for the rigid body spacecraft centers on the tight momentum control and control authority, the 3-axis-stabilized configuration is likely to have ACS issues associated with the spinning platform. These will include reduced pointing knowledge performance, pointing accuracy, and safety and operational issues.

4.4 STRUCTURAL ANALYSIS

At the outset of the study, SAIC was tasked to perform a system engineering role, with JPL/Team-I performing supporting analysis. However, except for an initial site visit and a few subsequent teleconferences, there was a limited interaction between SAIC and Team-I. This was partly due to the remoteness of SAIC from JPL and Team-I's busy schedule. Also, Team-I worked independently of SAIC with models provided internally at JPL. Team-I provided preliminary structural analysis of the OSIRIS system, as described below, as a precursor to the more detailed industry studies conducted during the second phase of the project (Section 8). Team-I also provided a thermal analysis of the mesh reflector that is discussed in Section 6, in connection with the mesh emissivity and radiometric performance analyses.

The OSIRIS microwave instrument uses an AstroMesh antenna developed by TRW Astro. The AstroMesh antenna is a deployable microwave reflector with a nominal diameter of 6 meters. The mesh is comprised of gold-coated molybdenum wire stretched into a parabolic shape. The parabolic shape is created by a truss structure composed of graphite tubes around the perimeter, flat kevlar ribbons forming a top and bottom web, and tension tie assemblies connecting the two kevlar webs at each node. In operation, the perimeter truss anchors the top and bottom web, while the tension ties deform the web into the desired parabolic shape. The mesh itself is stretched across the top web, essentially acquiring whatever shape the web has been deformed into. In orbit, this antenna assembly is connected to the spacecraft with an articulated tubular arm. In the 3-axis-stabilized case, the antenna, arm, and top portion of the spacecraft spin at 6 rpm, with the nadir direction parallel to the spin axis. The bottom part of the spacecraft is despun.

TRW Astro provided a NASTRAN finite element model of the reflector to JPL for incorporation into the Team-I analysis. The antenna reflector is supported on one side, and in the configuration and boundary conditions delivered to JPL, had a first mode structural frequency of 3.77 Hz. In the model analysis the reflector was attached to the spacecraft support structure using a mast made of aluminum tubing, 5 inches in diameter and 0.05 inch in wall thickness. The geometry of the mast was taken from the CAD design supplied by SAIC. The spacecraft was not modeled since it is rigid compared to the reflector and the mast. The spacecraft end of the mast was fixed since the design has the center of rotation going through the spacecraft axis. The primary loading considered was the loading due to rotation at 6 rpm. With this loading applied, the maximum deflection of the system was 0.305 inch at the tip of the reflector. In addition to the static deflection caused by the rotational velocity, the mast also results in low natural frequencies for the antenna. The tubing for the mast was changed to increase its stiffness by increasing the wall thickness from 0.05 inch to 0.25 inch. Results of this analysis were fed back to SAIC and TRW Astro, and used as the basis for the TRW study described in Section 8.

42

4.5 CONCLUSIONS

The TRW AstroMesh antenna and Harris DTS antenna were identified as viable mesh antenna candidates. The AstroMesh antenna was selected for further study based on the stiffness advantage of the perimeter truss design for a spinning configuration and the ready availability of data on this antenna from the vendor. Spacecraft buses from TRW and Spectrum Astro, available in the RSDO catalog, were identified as viable candidates for the rigid-spinner or 3-axis-stabilized configurations. The Taurus (92-inch fairing) was identified as the cheapest launch vehicle with sufficient payload volume and mass performance to the required orbit. The configuration with the antenna above the spacecraft was confirmed as optimal. Configuration drawings of the antenna reflector, boom, and satellite bus within the Taurus 92-inch fairing, and a proposed deployment sequence were developed. A preliminary attitude control system analysis was done. The momentum storage requirement was determined to be in the range 120 N-m-s (3-axis) to 200 N-m-s (spinner). A preliminary structural analysis of the reflector was preformed by Team-I.

Based on recommendations resulting from the initial SAIC and Team-I studies, two parallel approaches for the OSIRIS spacecraft were subsequently pursued. One design focused on a rigid body spinner spacecraft, while a second design focused on a three-axis-stabilized spacecraft. These studies were based on low-cost, previously-flown spacecraft from TRW and Spectrum Astro, respectively, accommodating a 6-meter diameter AstroMesh antenna along with the other OSIRIS requirements. To carry out the design analyses needed to determine the performance and feasibility of both design options, JPL procured the services of the spacecraft vendors, TRW and Spectrum Astro, as well as the antenna manufacturer, TRW Astro. TRW Astro was directed to work with both vendors to provide them with structural data on the AstroMesh antenna and the interface information needed to incorporate the antenna system in the spacecraft designs. These studies are described further in Section 8.

43

5. ANTENNA AND FEED DESIGN

An advantage of reflector antennas is the ability to use multi-frequency, dual-polarization feeds with minimum cost and complexity. Multi-frequency, dual-polarization feedhorns have been developed for previous spaceborne instruments including the SMMR, SSM/I, and AMSR. The challenge in this study was to design a feedhorn with good performance over the frequency range 1.26–2.7 GHz and to reduce the feedhorn mass by using an optimized feedhorn geometry.

The OSIRIS baseline design described in Sections 3 and 4 was used to analyze the antenna configuration and feedhorn design from an electromagnetic performance point of view. In the first phase of the study this included determining characteristics of the antenna patterns, i.e., sidelobe levels, gain, beam efficiency, and the impact of surface rms errors and mechanical and thermal distortions on this performance. In the second phase, design studies of various lightweight feeds were carried out. These studies were performed through a contract with the University of California, Los Angeles.

5.1 APPROACH

In Table 5.1-1, specifications for the radiation characteristics of OSIRIS are summarized as derived from the baseline system design. BW_E and BW_H denote the 3-dB beamwidths in the E- and H-planes, respectively.

Table 5.1-1. Requirements for OSIRIS Antenna Pattern Performance

Operating Frequencies (GHz)		Design Requirements	
Radar (L-band)	1.26	Beam tilt from boresight	4.25°
Radiometer (L-band)	1.41	Beam efficiency (radiometer)	> 90%
Radiometer (S-band)	2.69	Beam symmetry at L- and S-band*	$BW_E \approx BW_H$

* BW = beamwidth

The approach to analyzing the radiation characteristics of the OSIRIS antenna can be itemized as follows:

- The radiation characteristics of the reflector surface are evaluated using Physical Optics (PO) (Rahmat-Samii, 1993; Duan and Rahmat-Samii, 1995). The electrical reflector diameter is between 25 λ at 1.26 GHz and 54 λ at 2.69 GHz; hence, a high-frequency technique such as PO yields very accurate results.

- The radiation characteristics of the horn feeds are computed using a mode-matching technique to describe the propagation through the cylindrical horn structure, and an aperture integration at the horn aperture to determine the scattered fields.

- The incident field at the reflector surface is determined from the horn scattered fields. The magnetic horn far-field patterns H^{inc} are discretized in their principal cuts, fed into the reflector analysis program, and the electric currents $J = 2\hat{n} \times H^{inc}$ on the reflector surface are determined by interpolation of these far-field data points.

- The design was optimized for the radiometer L-band performance, which is the most critical for SSS measurement.

45

5.2 Antenna Geometry and Feed Design

5.2.1 Reflector Design

Figure 5.2-1 shows a vertical cross-section through the OSIRIS reflector antenna. The reflector diameter, focal length, and offset height are 6 m, 3.6 m, and 3 m, respectively. The feed is rotated to the bisect angle A = 39.8°. At this angle, which is the reflector subtended half-angle, the feed taper is required to be approximately 15 dB, which yields the best compromise between high aperture efficiency and beam efficiency (Zimmermann, 1991; Shen and Stutzman, 1995; Rahmat-Samii et al., 1998).
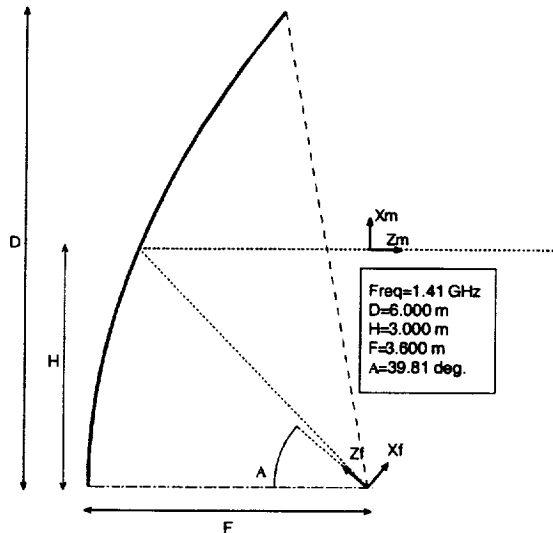
Figure 5.2-1. Vertical cross-section through the OSIRIS reflector, showing the key geometrical parameters.

5.2.2 Corrugated Feedhorn Design

In the evaluation of conical horn and conical-corrugated horn feeds, a variety of numerical methods can be applied. If a standard conical horn feed is evaluated, it is often sufficient for a first estimate of the far-field patterns to assume that the aperture distribution of the horn is equal to the transverse field distribution inside the feeding waveguide. An additional factor accounts for the quadratic phase distribution in the aperture due to the flare angle of the horn (Balanis, 1997). If a corrugated horn is considered, the same spherical phase term can be applied, while the amplitude distribution now becomes uniform due to the influence of the corrugations (Clarricoats and Olver, 1984; Olver et al., 1994). This method, however, lacks the capability to account for non-standard corrugated horn geometries such as specialized tuning sections or multi-frequency responses.

In evaluation of corrugated horns, the mode-matching method has been applied successfully. In this method, the corrugated horn is simulated as a series of cylindrical waveguides. The S-matrix for each of the sections is established, as well as for the junctions between the sections. Finally, the S-matrix of the total horn is calculated as a product of the individual matrices, and the reflection and transmission of the individual waveguide modes at the horn input section can be traced to the aperture of the horn.

46

In Figure 5.2-2, the parameters of the corrugations, and the geometry of conical, conical-corrugated, and profiled-corrugated horns are shown. Several conical and conical-corrugated horns have been designed and analyzed using the mode matching technique. If the horn aperture is electrically large enough, a slot depth of S = λ/4 produces balanced hybrid conditions. For electrically smaller apertures the slot depth must be increased toward the horn aperture. The slot-width to ridge-width ratio was chosen as b/T = 1. At higher frequencies, requiring small values of b and T, the fabrication of very narrow slots becomes difficult and the ratio b/T has to be increased. However, very wide slots (b>2T) lead to numerical instability. The profiled or compact horn was found to have the most suitable performance over the large frequency band desired in the design. Contrary to the linearly flared horns, the profiled-horn design maintains an approximate beam symmetry without bifurcation.
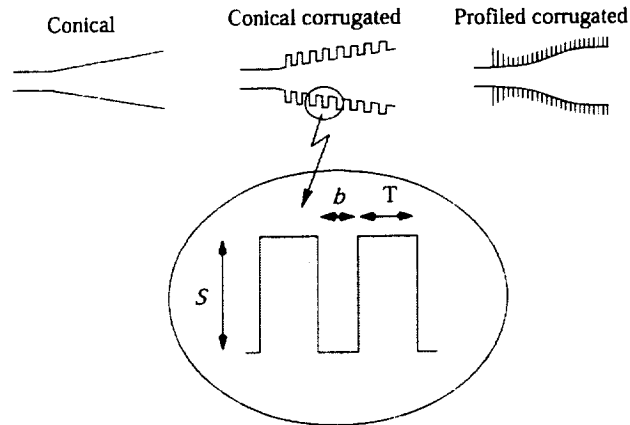
Figure 5.2-2. Geometrical parameters of the corrugations in a conical corrugated horn; T and b are the respective widths of the ridge and the slot, and S is the slot depth.

The radiation characteristics of selected horns studied are summarized in Table 5.2-1. For each of the horns, the reflection coefficient (r = S_{11}), the VSWR (s = (1 + r)/(1 − r)), and the return loss (a = 20 log (1/r)) are given. Throughout this design and analysis, it has been assumed that there exists a suitable feeding network that is capable of separating the signals coming in at the three different operating frequencies and two polarizations. The return loss of this feeding network has not been included in the results shown in Table 5.2-1. Investigations into the realization of such a feeding network are a subject of ongoing research.

Table 5.2-1. Characteristics of Horn Feed Designs at OSIRIS Operating Frequencies

Horn model	S_{11} (%)	VSWR	a (dB)
Radiometer, L-band			
Conical horn	5	1.12	25
Corrugated horn, model #1	6	1.14	24
Corrugated horn, model #2	1	1.03	37
Radiometer, S-band			
Conical horn	2	1.04	34
Corrugated horn, model #1	1	1.02	40
Corrugated horn, model #2	1	1.02	40
Radar, L-band			
Corrugated horn, model #2	12	1.27	18

In Figures 5.2-3 (a)–(c) the geometries of the horns are shown. The conical horn exhibited strongly asymmetric L- and S-band far-field patterns. This pattern asymmetry, and its expected effect on the secondary pattern of the reflector, eliminated the conical horn type as a possible feed candidate. The far-field patterns of the profiled corrugated horn (model #2) are shown in Figure 5.2-4 (a)–(c). This horn produced the best far-field patterns of the three horn types shown in Figure 5.2-3. Within the figures, both the reflector subtended half-angle ($\approx 40°$) as well as the necessary edge taper (15 dB) are shown as straight lines to help identify the system requirements on the horn design. The design meets the specifications of low return loss at all the frequencies as well as the far-field pattern requirements of having approximately a 15-dB edge taper within the subtended half angle of the reflector. This horn is also compact, having the shortest length of the designs considered.

In Figure 5.2-5 the compact corrugated horn geometry is displayed, including a feed input section. The total horn length including this input section is approximately 1 m. In the actual implementation of this design, another small waveguide section would be appended to the left of the feed input section adding approximately 65 mm to the total length of the horn. In the corrugated section of this horn, the tooth width and gap width are equal at 10.6 mm; i.e., 10 corrugations per wavelength at 1.414 GHz. With respect to this frequency, the depth of the gap varies from $\lambda/2$ (106.1 mm) to $\lambda/4$ (53 mm).

Figure 5.2-6 shows schematically, two corrugated horns (of the type shown in Figure 5.2-5) offset from the focal axis in the focal plane of the reflector antenna. With an estimated outer horn radius of about 300 mm at the aperture of the horn, the horns are displaced by 320 mm in the y-direction and 120 mm in the x-direction. This displacement yields the desired footprint of the secondary pattern, tilted from the boresight direction by 4.25°. This off-axis placement is needed to achieve the footprint coverage on the ground of the two beams as described in Section 3.

5.3 ANTENNA PERFORMANCE

The secondary patterns of the reflector antenna were computed for both on-axis and off-axis feedhorn locations.

5.3.1 Feed at Focus

The key radiation parameters are summarized in Table 5.3-1 in terms of directivity (D), antenna efficiency (AE), the half-power beamwidth in the two principal cuts (BW), and the beam efficiency (BE). The profiled-corrugated horn design (model #2) yields the secondary far-field patterns shown in Figure 5.3-1. At 1.41 GHz the far-field patterns exhibit excellent symmetry, while the far-field patterns at 2.7 GHz have a slight but still acceptable asymmetry. In particular, the first sidelobes on either side of the main beam are more pronounced and not completely incorporated into the main beam. The beam efficiency achieved at both frequencies is approximately 96% (as shown in Table 5.3-1) with an average beamwidth of 2.6° and 2.0° at 1.41 GHz and 2.7 GHz, respectively. Note also that the beam efficiency at 1.26 GHz is 88.6% which is acceptable for the radar. This horn achieved the overall design requirements, and was used for subsequent studies.
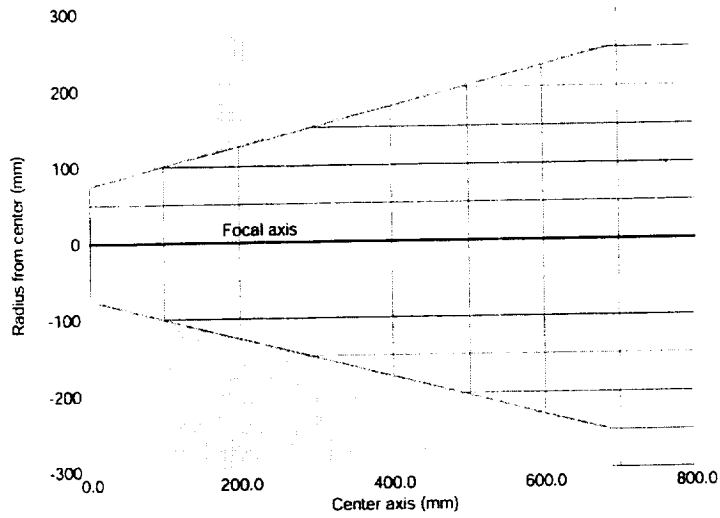
Figure 5.2-3 (a). Conical horn geometry.
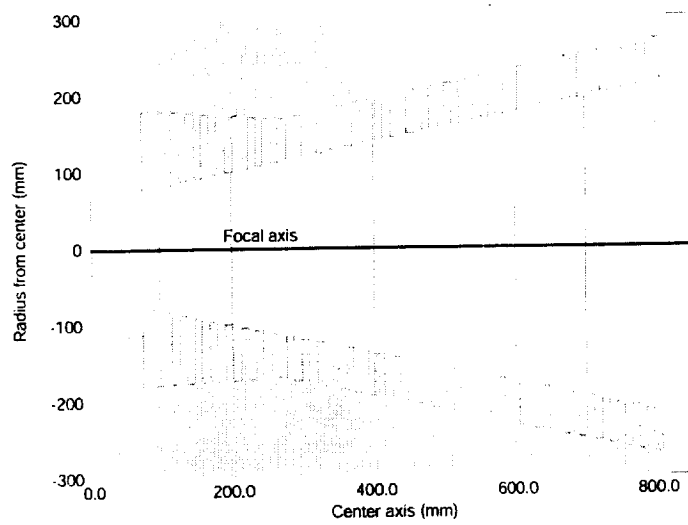
Figure 5.2-3 (b). Conical corrugated horn geometry (model #1).
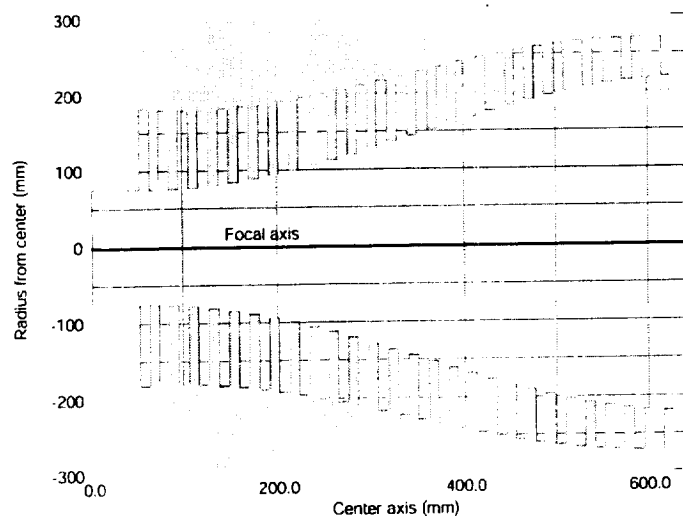
Figure 5.2-3 (c). Profiled corrugated horn geometry (model #2).

49

(a) 1.414 GHz

(b) 2.69 GHz

(c) 1.26 GHz
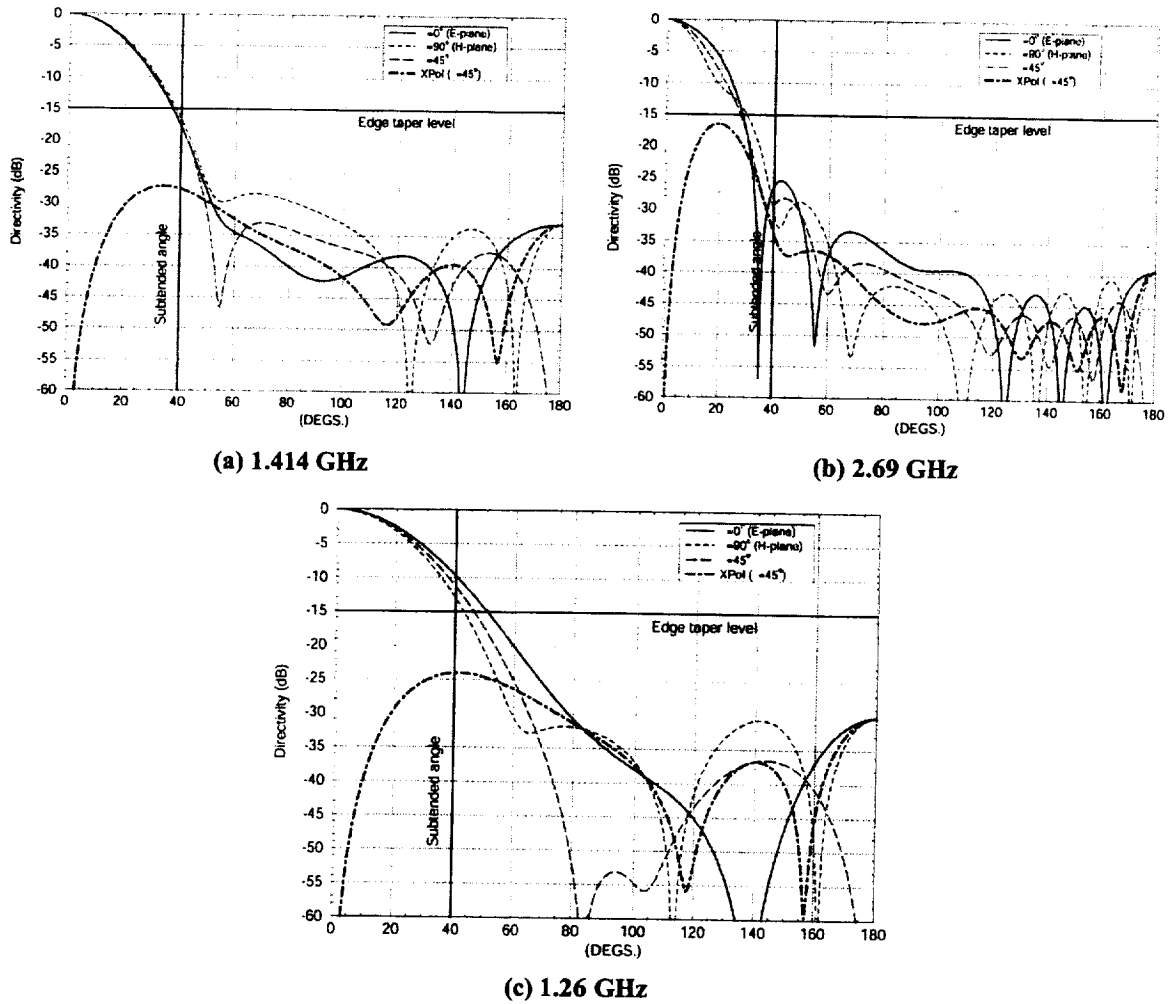
Figure 5.2-4. Far-field pattern of profiled corrugated horn (model #2).

**Table 5.3-1. Radiation Performance of OSIRIS Reflector Antenna
With Corrugated Feed Model #2**

	D (dBi)	AE (%)	BW_E (deg.)	BW_H (deg.)	BE (%)
Radiometer, 1.414 GHz	37.4	69.5	2.6	2.6	96.2
Radiometer, 2.69 GHz	39.3	29.5	1.7	2.3	95.7
Radar, 1.26 GHz	36.7	75.1	2.6	2.8	88.6

(Feed at focus.) (D = directivity, AE = antenna efficiency, BW_E and BW_H = half-power beamwidths in the two principal cuts, BE = beam efficiency)

50
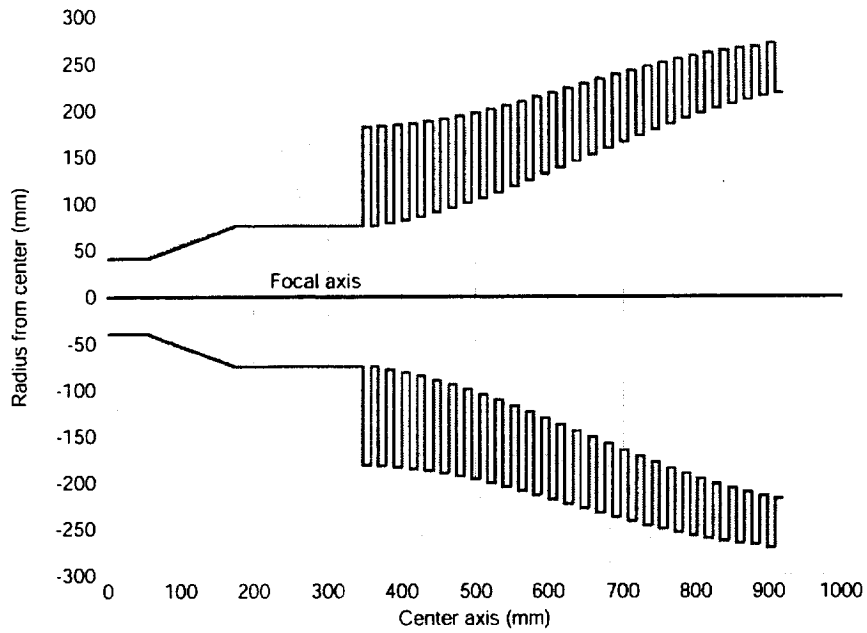
Figure 5.2-5. Detailed geometry of compact corrugated feed horn including a candidate feeding section.
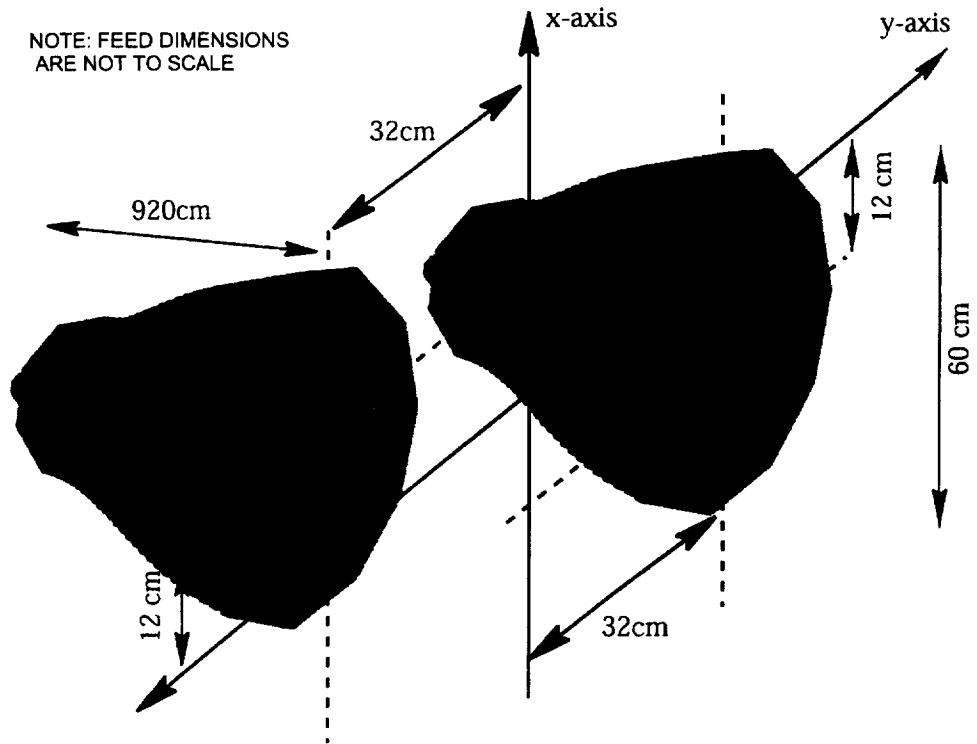
Figure 5.2-6. Schematic layout of the two corrugated feedhorns at the focal plane of the reflector antenna.

51

5.3.2 Feed off Focus

The main reflector antenna patterns were also computed with feeds placed off-focus in the reflector focal plane as shown in Figure 5.2-6. In Figure 5.3-2 the secondary far-field patterns at 1.41 and 2.69 GHz are shown for a single feed placed off-focus. Due to the displacement, the beam efficiency of the reflector antenna deteriorates slightly to 94.3% and 92.1% for L-band and S-band, respectively. The cross-polarization level at L-band remains almost unchanged, while the S-band cross-polarization level increases slightly. The greater degradation at S-band can be credited to the larger feed displacement in terms of wavelength.

(a) 1.41 GHz.   (b) 2.69 GHz.
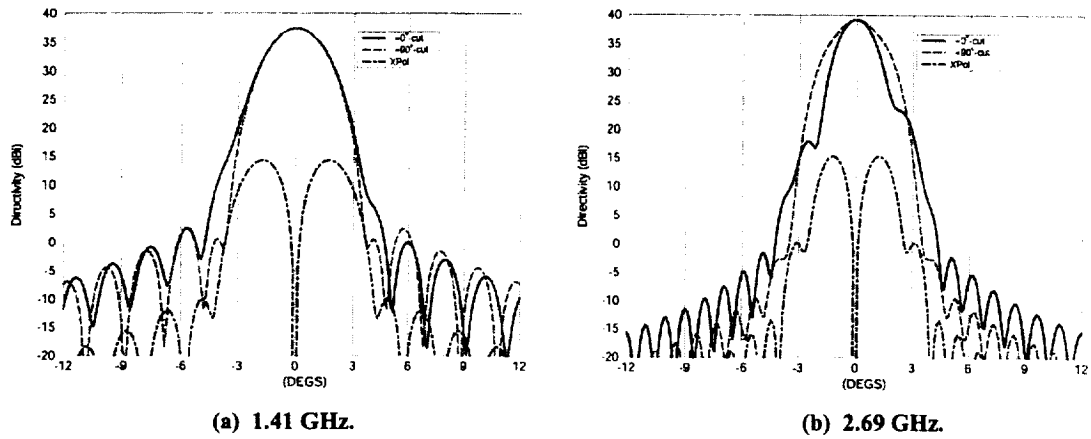
Figure 5.3-1. Far-field reflector antenna pattern (feedhorn model #2); feed at focus.

(a) 1.41 GHz.   (b) 2.69 GHz.
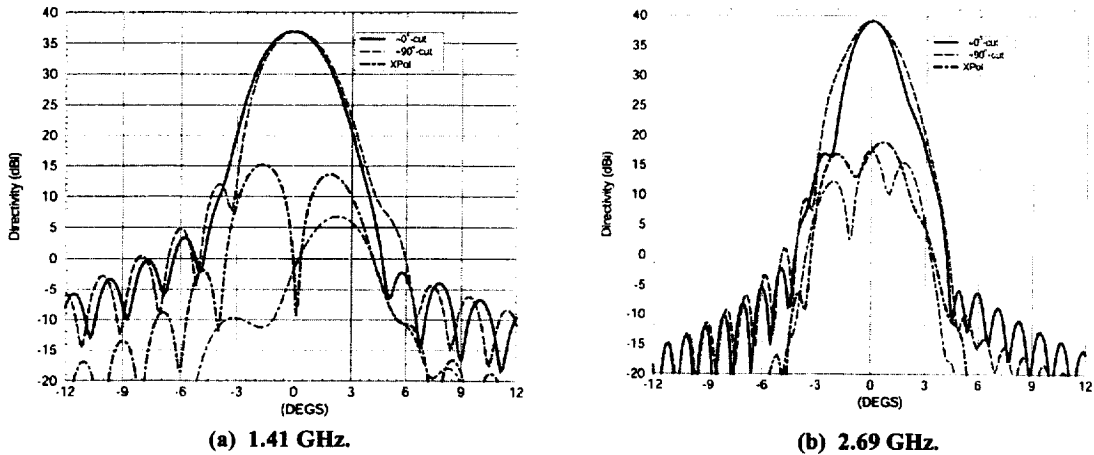
Figure 5.3-2. Far-field reflector antenna pattern (feedhorn model #2); feed off focus.

In Figure 5.3-3, the beam contour patterns at 1.41 GHz for co-polarization and cross-polarization are displayed. Both main beams are clearly separated. The directivity level between the beams is about 24 dB below the main peaks. The cross-polarization level is about 23 dB below the main peak. Similarly, Figure 5.3-4 displays the beam contour patterns at 2.69 GHz. The co-polarization beams are further isolated because of the increased focusing properties of the electrically-larger reflector. The cross-polarization level is approximately 18 dB below the main peak level.

(a) Co-polarization

(b) Cross-polarization
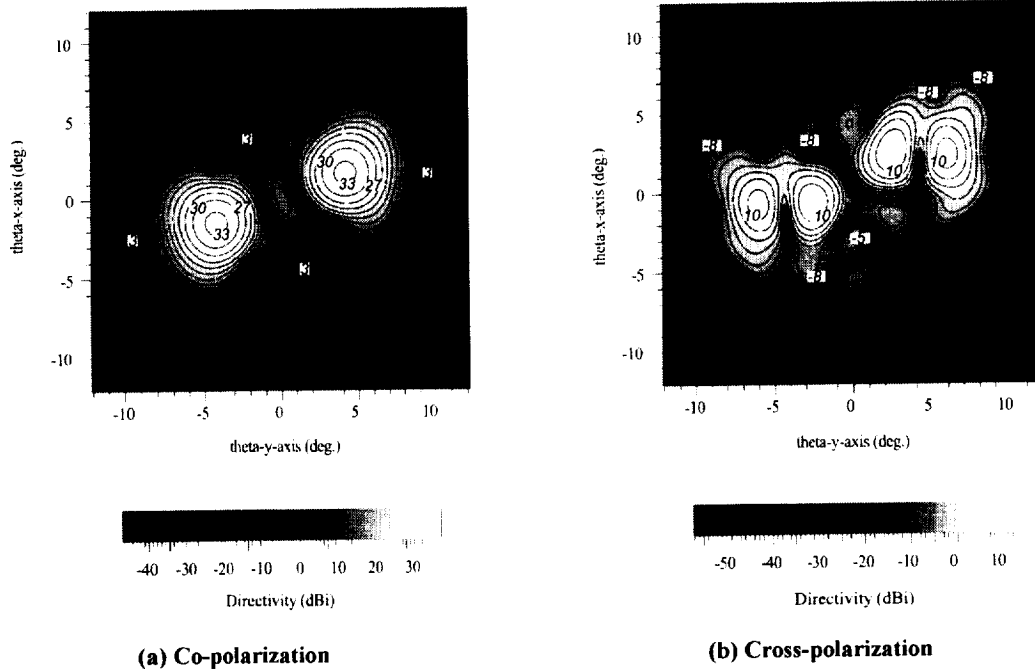
Figure 5.3-3. Beam contour pattern of the reflector antenna; feed off focus; 1.41 GHz.

(a) Co-polarization

(b) Cross-polarization
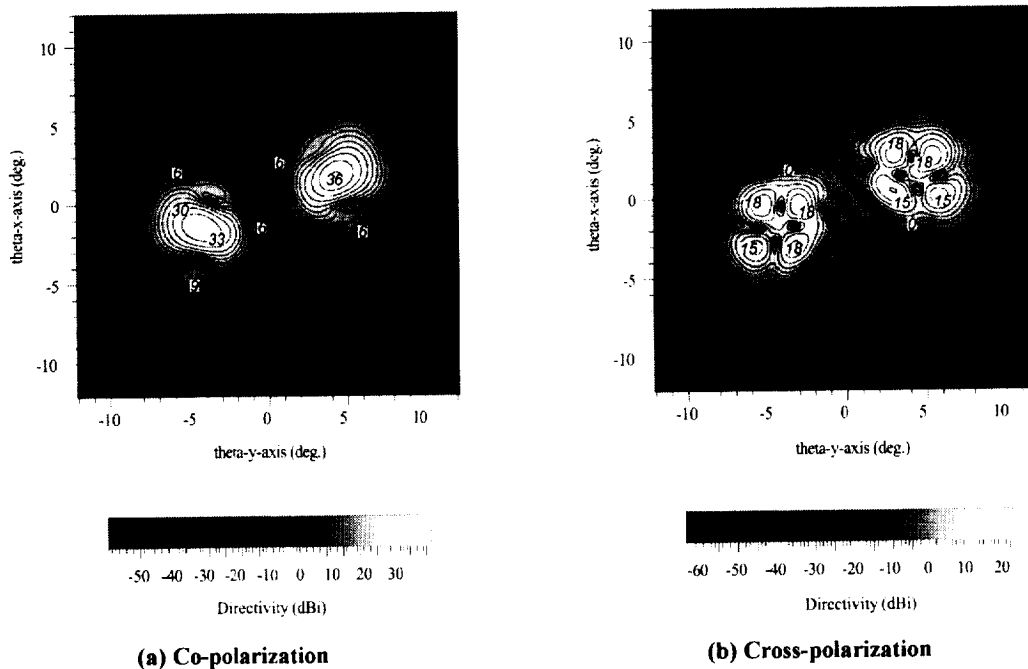
Figure 5.3-4. Beam contour pattern of the reflector antenna; feed off focus; 2.69 GHz.

The reflector surface currents due to the first feed (right horn in Figure 5.2-6) at 1.41 and 2.69 GHz are displayed in Figure 5.3-5. The magnitude of the total surface currents is shown. Similarly, Figure 5.3-6 shows the reflector surface currents due to the second feed (left horn in Figure 5.2-6). The maximum of the surface current magnitude is clearly shifted due to the off-focus illumination, resulting in the beam offsets shown in Figures 5.3-3 and 5.3-4. Note also that, as expected, the 2.69-GHz surface currents are slightly elongated in elevation, and yield therefore slightly asymmetric far-field patterns as displayed in Figure 5.3-2.

(a) 1.41 GHz

(b) 2.69 GHz
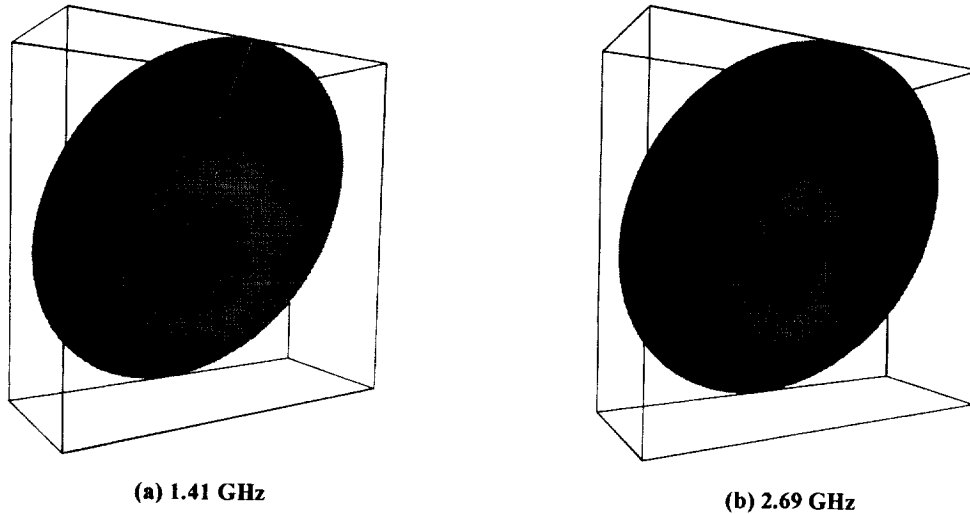
Figure 5.3-5. **Reflector surface currents due to feedhorn #1. The magnitude of the total currents is shown.**

(a) 1.41 GHz

(b) 2.69 GHz
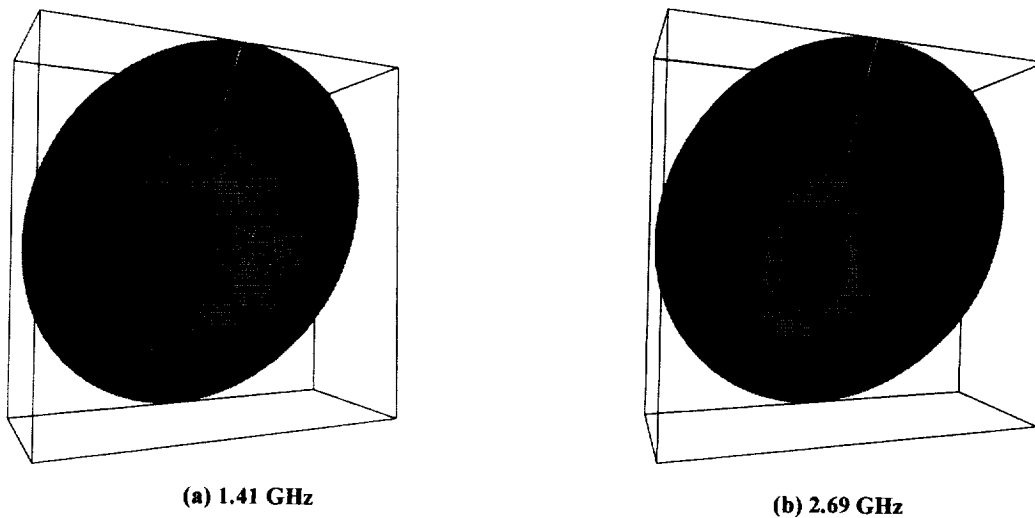
Figure 5.3-6. **Reflector surface currents due to feedhorn #2; the magnitude of total currents is shown.**

5.4 REFLECTOR SURFACE TOLERANCE

Feed displacement reduces the beam efficiency of the reflector antenna due to the induced phase distortion in the aperture plane. Another cause of performance degradation in reflector antennas is reflector surface errors. These errors are commonly described in terms of a zero mean,

Gaussian distribution with a standard deviation of σ (Ruze, 1966; Rahmat-Samii, 1985; Rahmat-Samii, 1993). In a recent paper, the effect of surface distortions on the beam efficiency, given in terms of the Gaussian distribution, was described (Rahmat-Samii et al., 1998).

It has been shown, that, for a given beam efficiency of a reflector antenna, the effect of reflector surface distortion can be described with a multiplicative factor of the form

$$\eta = \exp\left[-\left(4\pi\kappa\frac{\sigma}{\lambda}\right)^2\right]$$

(5.1)

where σ/λ denotes the rms surface distortion normalized to wavelength and κ can be estimated from

$$\kappa = 4\frac{F}{D}\sqrt{\log\left[1+1/\left(4\frac{F}{D}\right)^2\right]}$$

(5.2)

to be $\kappa = 0.96$ for this particular reflector geometry. Given the beam efficiencies for the off-focus configuration at L-band and S-band to be 94.3% and 92.1%, respectively, the effect of a random surface distortion is investigated and summarized in Tables 5.4-1 (for L-band) and 5.4-2 (for S-band).

A beam efficiency of 90% was required for the OSIRIS performance that incorporates the losses due to feed displacement and random surface errors. With this, the maximum surface error becomes for L-band $\sigma/\lambda = 1/55 = 3.9$ mm. Its distortion efficiency is $\eta_L = 95.3\%$ and the beam efficiency of the reflector antenna becomes 89.9%. At S-band, however, a distortion efficiency of $\eta_S = 97.8\%$ is required to keep the beam efficiency at ~90%, which in turn demands a surface error of $\sigma/\lambda = 1/80 = 1.4$ mm.

To achieve these beam efficiency requirements, the more stringent surface error tolerance at S-band must be followed, i.e., $\sigma = 1.4$ mm. If this surface error is achieved, the beam efficiency at L-band in turn becomes, with a distortion efficiency of $\eta_L = 99.4\%$, an almost perfect 93.74%.

Table 5.4-1. Surface Distortion Efficiency (η) for the Reflector Antenna at L-Band (Feed Off Focus)

rms (λ_L)	Efficiency, η (%)	rms (mm)	BE_L (%)
1/10	23.3	21.2	22.0
1/20	69.5	10.6	65.5
1/30	85.1	7.1	80.2
1/40	91.3	5.3	86.1
1/50	94.3	4.2	89.0
1/55	95.3	3.9	89.9
1/60	96.0	3.5	90.6
1/70	97.0	3.0	91.6
1/80	97.8	2.7	92.2
1/90	98.2	2.4	92.7
1/152	99.4	1.4	93.7
0	100	0	94.34

Table 5.4-2. Surface Distortion Efficiency for the Reflector Antenna at S-Band (Feed Off Focus)

rms (λ_L)	Efficiency (%)	rms (mm)	BE_L (%)
1/10	23.3	11.2	21.4
1/20	69.5	5.6	63.9
1/30	85.1	3.7	78.3
1/40	91.3	2.8	84.0
1/50	94.3	2.2	86.8
1/55	95.3	2.0	87.7
1/60	96.0	1.9	88.4
1/70	97.0	1.6	89.3
1/80	97.8	1.4	89.9
1/90	98.2	1.2	90.4
	100	0	92.09

5.5 LIGHTWEIGHT FEEDHORN OPTIMIZATION

Corrugated horns are suitable as feeds for reflector antennas due to their high beam efficiency and low cross-polarization levels. For spaceborne applications, there is always a need to minimize weight without sacrificing overall performance of the antenna. The first phase of this study focused on the design of a profiled horn, which shortens the total length of the horn, creating a lighter horn with good performance characteristics. Most of the weight from a corrugated horn comes from the horn's teeth. One way of minimizing weight is to have the teeth as thin as possible and have as few of them as possible while still maintaining high performance.

The objectives in the second phase of this study were to find the lightest possible horn antenna with best performance in meeting the OSIRIS requirements. The horn feed needs to produce an edge taper of about -15 to -17 dB, the 3-dB beamwidth should be about 34 degrees, and the cross-polarization should be minimized. Two different methodologies were used to design the feedhorn. The first method applies a brute-force method of examining the radiation characteristics of various horn configurations in order to determine the best result. The second method uses a genetic algorithm (GA) optimization technique (Rahmat-Samii and Michielssen, 1999) to find the optimum design of the horn antenna. The computer generates different designs and rates them based on their overall performance. The rating system is a user-defined cost function devised to evaluate horn performance and pick out the best design.

5.5.1 Design Considerations

In the mid-1960's, Simmons and Kay introduced scalar horns or, as we call them today, corrugated horns (Simmons and Kay, 1966). Later studies revealed that advantages of corrugated horns were not limited to having only low sidelobes and spillover power. Corrugated horns are capable of producing a nearly axially-symmetric radiation pattern, low sidelobe levels, well-defined phase center, nearly-constant beamwidth over a large frequency band, low loss, low VSWR (Caldecott et al., 1973), and low cross-polarization (Olver et al., 1994). These properties of corrugated horns make them the best choice for feeding reflector antennas. Many different techniques have been developed for analyzing corrugated horns with arbitrary flare angles (Olver et al., 1994; Love, 1976). Nevertheless, little effort has been made in studying the effects of corrugation width and wall thickness on the radiation performance of corrugated horns. Perhaps the best conceptual treatment of this problem can be found in Mentzer and Peters (1973). Results

56

of that study can be used to deduce that, at a given frequency, decreasing the number of corrugations and thickness of the teeth decreases the metallic surface loss and does not appreciably affect the desired radiation behavior of the corrugated horn but could degrade the input match.

Currently, it is convenient to explain the EM performance of corrugated horns using the concept of a hybrid balance condition which assumes that both E and H fields satisfy similar boundary conditions over the internal boundary of the horn, which is defined as the envelope of the corrugation teeth. This implies that the corrugation width cannot exceed $\lambda/4$, where λ is the free space wavelength at the upper limit of the operating frequency range. On the other hand, it is assumed that the slots are so narrow that only a single non-propagating TM mode is capable of existing in them (Caldecott et al., 1973). This condition again demands corrugation width to be kept reasonably small. A similar discussion applied to H fields at the top of the teeth implies that the corrugation thickness t (Figure 5.5-1) should not exceed $\lambda/4$. These observations give lower limits for the number of corrugations and wall thickness. The results of Mentzer and Peters (1973) imply that within the above-specified range, the number of corrugations and thickness of walls can be decreased without degrading the radiation performance. Undesirable effects of such a modification on the input match can be minimized by introducing a linear variation in the depth of corrugations which provides a gradual transition from the Perfect Electric Conductor (PEC) boundary condition at the horn throat to the hybrid balance condition at the horn aperture.

From the above discussion, an upper limit for groove width of around $0.2\ \lambda$ is obtained with a safety margin of 20%, with very thin walls $t/w \ll 1$; i.e., $w \cong 0.2\ \lambda$ (Figure 5.5-1). A final design value for corrugation thickness t is dictated by fabrication limitations. With the current state of the art in composite material technology, a wall thickness of as little as 1 mm can be fabricated. These physical limitations put a lower bound on the weight of the corrugated horn.

5.5.2 Brute Force Design Results

A cylindrical mode matching technique was used to analyze the geometry of Figure 5.5-1 for obtaining the aperture fields. The far field pattern was then obtained from radiation of the equivalent aperture sources in free space. The calculated radiation patterns for the original design (design #1) at L- and S-bands are given in Figures 5.5-2(a) and 5.5-2(b), respectively. With $w = \lambda/10$ at 1.414 GHz (L-band), and $r = t/w = 0.5$, the calculated total weight is around 53 lb. for this design. At L-band, the pattern is symmetrical. The edge taper is near the optimum value of -15 dB and cross polarization is below -25 dB. Considerable degradation occurs at S-band, however. The corrections were done in two steps. In the first step, the wall thickness t was reduced to the finest achievable value, with w kept fixed. In the second step the number of corrugations was further reduced to half the previous value by increasing w to $\lambda/5$. Figure 5.5-3 shows the radiation patterns for this last case (design #3). The weight is reduced to about 15 lb., calculated based on data provided by a commercial manufacturer. The outside of the horn weighs 3 lb., so that the teeth alone in the original design weighed 50 lb. Since the tooth/gap ratio is much smaller in the newer designs, the weight drops accordingly.

The radiation characteristics of these designs are summarized in Table 5.5-1. The last column in this table indicates the return loss when the horn is fed from the input waveguide at S-band. Although in practice the horn is usually fed via L-band and S-band probes, this quantity can be viewed as a measure of the input match between the horn and input section. These results show that the modified designs are comparable to the original design at L-band, while they perform better at S-band. It is observed that the cross-polarization is considerably decreased in the modified designs.
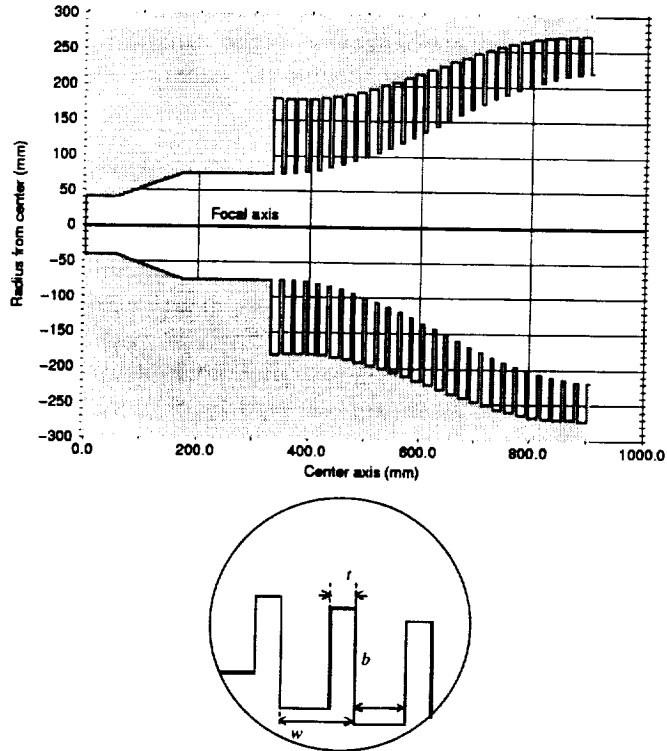
Figure 5.5-1. Geometry of a sine-profiled corrugated horn. (Design #1 from Table 5.5-1.)
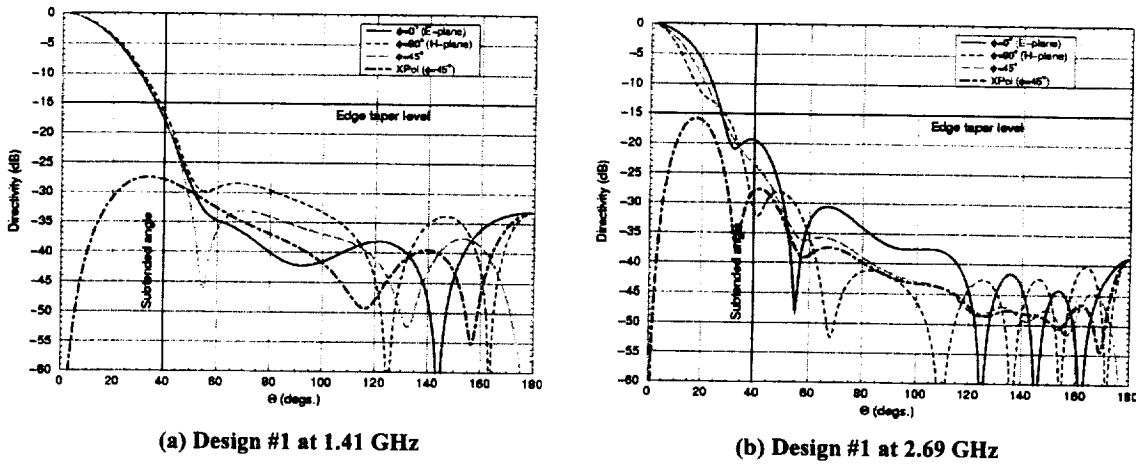
(a) Design #1 at 1.41 GHz

(b) Design #1 at 2.69 GHz

Figure 5.5-2. Radiation patterns of the corrugated feed horn with 10 corr/λ and $r = 0.5$.

Table 5.5-1. Radiation Specifications for Different Designs

Design Geometry			E-Plane				H-Plane				X-Pol. dB φ=45 (deg)		RL (dB)
			10 db-BW (deg)		Edge Tap. (dB)		10 db-BW (deg)		Edge Tap. (dB)				
No	λ/w	R	L	S	L	S	L	S	L	S	L	S	S
1	10	0.5	28	26	18	19	31.5	15	17	31	26	16	24
2	10	0.12	32	22	17	17	32	17	17	34	33	18	24
3	5	0.06	31	21	17	17	31	16	17.5	24	33	21	26

RL = return loss; R = t/w

58

(a) 1.41 GHz　　　　　　　　**(b) 2.69 GHz**
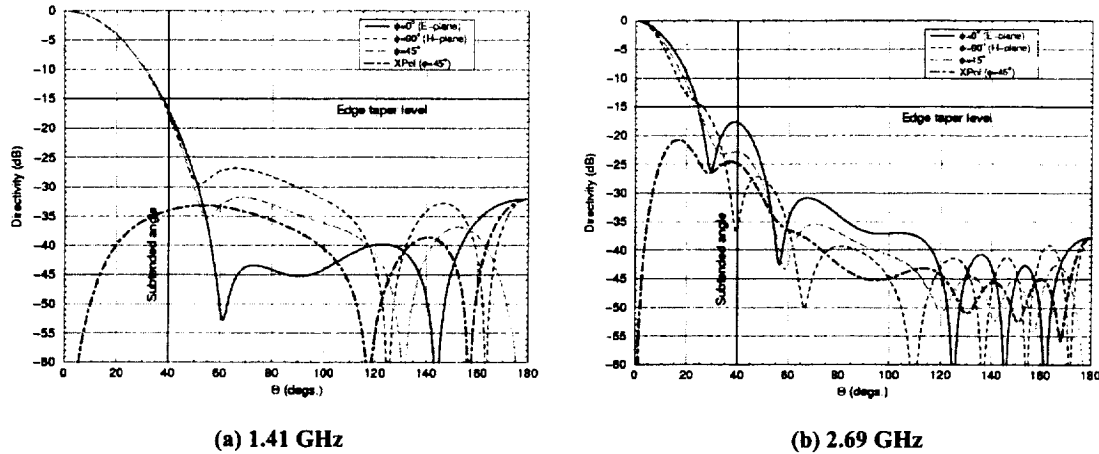
Figure 5.5-3. Radiation patterns of the corrugated feed horn design #3.

Design #3 is a potential candidate for feeding the OSIRIS antenna system. Figures 5.5-4 and 5.5-5 show the calculated radiation patterns of the offset reflector illuminated with the original and modified horn feeds. The reflector system provides a symmetrical pattern in the main lobe region with a 37.4 dBi directivity, 2.8 degrees HPBW in the E and H planes, 95% beam efficiency (feed horn situated at the focus), and below 15 dBi cross-polarization at L-band (cross-polarization isolation better than 22 dB).

5.5.3 Genetic Algorithm Design Results

In Table 5.5-2, results from the brute-force and genetic algorithm (GA) designs are compared. The horn designs are shown in Figures 5.5-6 and 5.5-7. The GA horn design in Figure 5.5-7 was selected out of a sample size of 15 designs over 10 generations. In all, there were 150 designs evaluated.

In the GA procedure a fitness function gives points to each design that meets certain criteria. The design with the most points yields the optimum design. The maximum points awarded for beamwidth was 50. The fitness function was weighted toward finding a target feedhorn 3-dB beamwidth of 34°. This beamwidth provides an approximate edge taper of -15 dB at a subtended angle that is 40° from the center. The closer the beamwidth was to 34° the more points it received. Points given for the reflection loss (S_{11}) were awarded based on the dB level. For example, if one design had a reflection loss of -35 dB, then the design got 35 points. The weight of the horn was divided by two and subtracted from the point total. The cross-polarization level was divided by 5 and added to the overall point total. The weights of the horn designs were calculated using a density of 0.06 lb./cu. in. and a shell thickness of 1 mm. The volume of the horn was calculated using a computer program and multiplied by the density to give the weight of the horn.

Table 5.5-2. Comparison of Brute-Force and Genetic Algorithm Horn Designs

Design	Length (m)	Weight* (lb.)	# of Corr.	Gap Width (mm)	Tooth Width (mm)	# of Corr./λ	Input Section Length (m)
Brute Force	0.57	14.7	14	40.71	2.44	5.00	0.16
GA	0.50	14.6	16	31.25	1.89	6.58	0.16

* Based on a density of 0.06 lb./cu. in. and a 1-mm thick outer shell of the horn

59
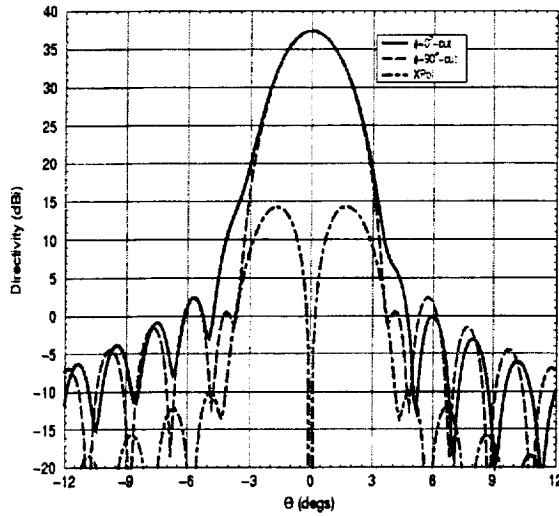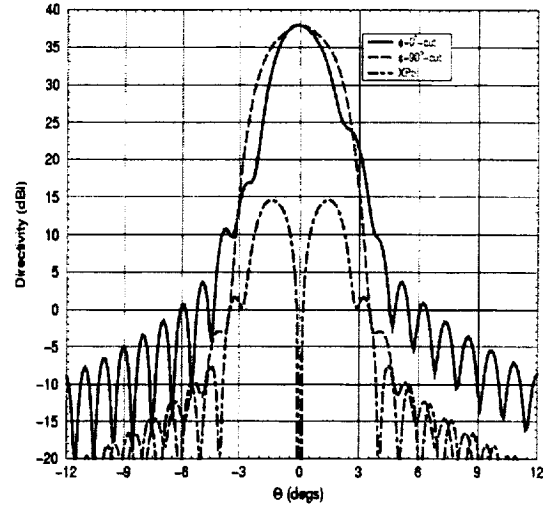
(a) 1.41 GHz   (b) 2.69 GHz

Figure 5.5-4. Far-field antenna reflector pattern, feedhorn design #1.
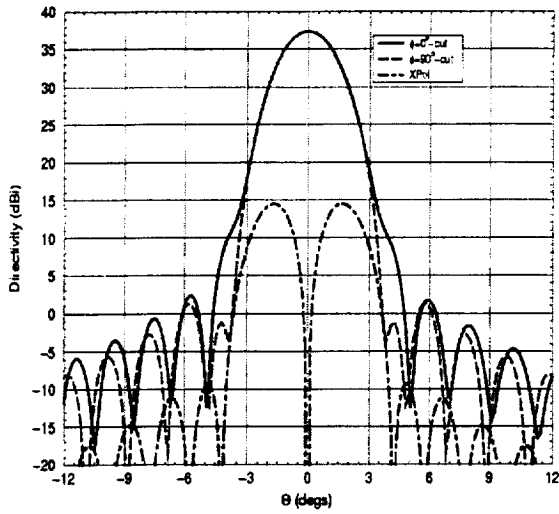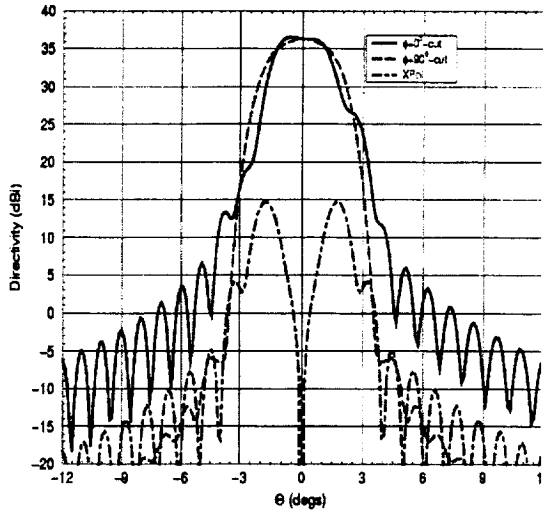
(a) 1.41 GHz   (b) 2.69 GHz

Figure 5.5-5. Far-field antenna reflector pattern, feedhorn design #3.

The horn patterns are shown in Figures 5.5-8 and 5.5-9. The GA horn has a slightly narrower beamwidth than the brute-force horn. However, the difference is very slight and is within the design goal. The cross-polarization level in the GA horn is also higher than the brute-force horn. Again the difference is negligible because the GA horn's cross-polarization level is still very low and should not affect the overall performance. The GA horn is 12.3% shorter than the brute-force horn (the brute-force horn is 0.57 m and the GA horn is 0.50 m); both horns are relatively short. The weight difference of the two horns is very close; the brute-force horn weighed 14.69 lb., while the GA horn weighed 14.57 lb. An advantage of the GA horn is the improvement in reflection loss; the GA horn's reflection loss is 13 dB lower than the brute-force horn (the brute force horn gives a reflection loss of –23.19 dB, while the GA horn has a reflection loss of –36.8 dB). Both designs have good reflection losses, but a lower reflection loss leads to better performance.
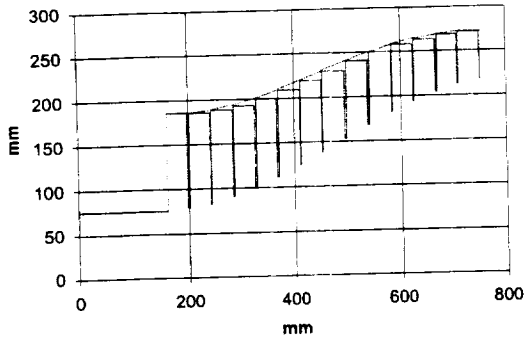
Figure 5.5-6. Profile of brute-force design horn.
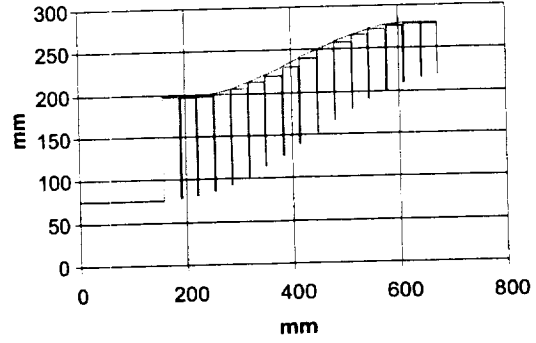
Figure 5.5-7. Profile of the GA design horn.
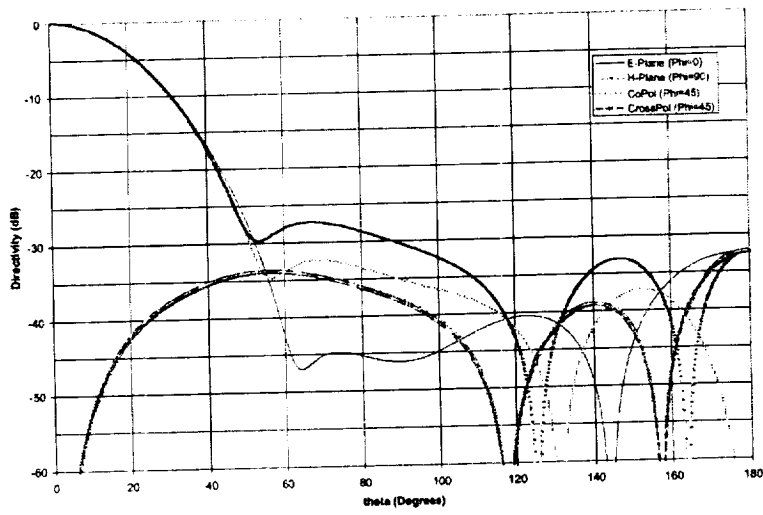
Figure 5.5-8. Brute-force design horn pattern at 1.41 GHz.
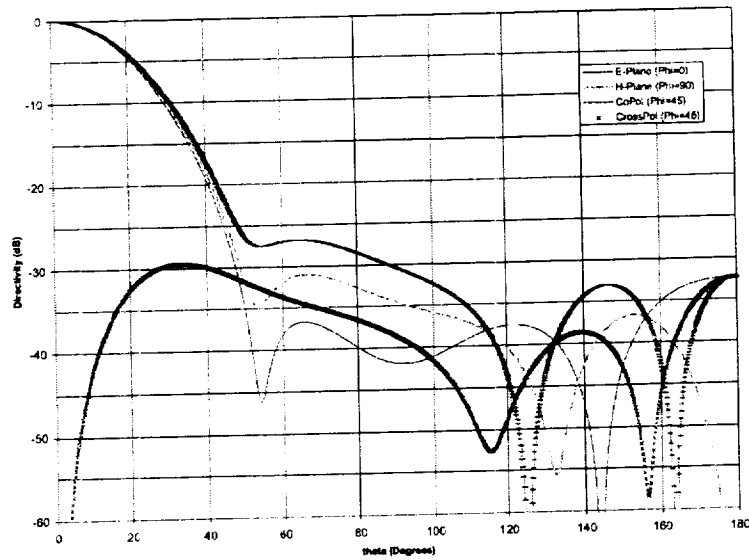
Figure 5.5-9. GA design horn pattern at 1.41 GHz.

61

When the horns are used in the offset reflector system with a 6 m paraboloid reflector, both horns provide very similar performances. Both horns provide a beam efficiency of 96% and a half-power beamwidth of 2.6° when the feed horn is located at the focus of the reflector antenna.

5.6 SUMMARY

In this study a compact, offset-fed, parabolic reflector antenna system (f/D = 0.6) was designed to produce from Earth orbit a dual-beam footprint at the surface for microwave remote sensing applications. A compact (minimum-length) corrugated horn feed was designed, and the effects of feed displacement for the dual-beam application were examined. The radiation performance of the reflector antenna system was studied in detail in terms of key radiation characteristics, including far-field patterns, beam contour patterns, and reflector surface distortions. The effects of random distortions of the reflector surface were included. Taking into account the multifrequency, offset dual-beam requirement, it was shown that the design would provide antenna patterns with good symmetry, sidelobe, and cross-polarization characteristics. The required 90% beam efficiency is met provided the random surface error is below 1.4 mm (imposed at the 2.7-GHz frequency). At 1.4 GHz the required surface error is 3.9 mm. It was assumed that a suitable feeding network would be developed for the horns to separate the signals at the three different operating frequencies and two polarizations. The return loss of this network was not included in the analysis.

The corrugated feedhorn design was optimized for weight reduction using brute-force and genetic algorithm approaches. Significant weight reductions are possible by careful choice of the number and thickness of the corrugations while maintaining good radiation pattern performance. Genetic algorithms are a powerful tool in the optimization of corrugated horns, and in this case proved effective in reducing the horn length by 12.3%. The GA optimized horn also provides superior reflection loss (13-dB improvement) over the brute-force design. The estimated weight of the feedhorn is about 15 lb. The manufacture, testing, and space qualification of the feedhorn design should be carried out as part of a subsequent flight program.

6. MESH RADIOMETRIC PERFORMANCE

Although deployable mesh technology has been used successfully for spaceborne communication applications, its use for microwave radiometer applications is not as well developed. In microwave radiometry the emissivity of the reflector is extremely important, and losses, which would be of little consequence in a communications application, may have serious effects in remote sensing applications. The loss or, equivalently, the emissivity of the reflector as well as the stability of this emissivity are major concerns and must therefore be carefully considered to realize the advantages of mesh technology for remote sensing applications.

As part of the OSIRIS study, the radiometric properties of mesh materials and the consequences of using mesh as a reflector surface for remote sensing applications were investigated. Measurements of mesh emissivity were performed at the NASA Langley Research Center (LaRC). The measurement approach and laboratory setup were designed as improvements on earlier measurements performed at LaRC in the 1980s. Mesh samples were obtained from two vendors: Harris Corp. and TRW Astro.

6.1 MESH MEASUREMENT GOALS

The impact of the reflector surface emissivity on the system radiometric error budget is illustrated in Figure 6.1-1. The measured antenna temperature can be considered as three terms: (1) the received power from the footprint of the antenna on the Earth's surface reduced by the reflectivity of the reflector surface, (2) the power radiated from the reflector surface and received by the feed; and (3) a very small term due to the cosmic background radiation transmitted through the mesh and received by the feed.

The overall OSIRIS error budget must account for variations in the radiometric properties of the mesh reflector. Since the on-orbit radiometric calibration does not include the main reflector, the stability of the radiometric error induced by the reflector is extremely important. The objective of this subtask was to measure and assess the radiometric properties of relevant mesh samples and to determine whether the predicted radiometric performance of the OSIRIS mesh reflector is consistent with the science measurement objectives.

$$T_{ant} = \Gamma_{mesh} T_{scene} + \varepsilon_{mesh} T_{mesh}^{phy} + T_{mesh} T_{cosmic}$$
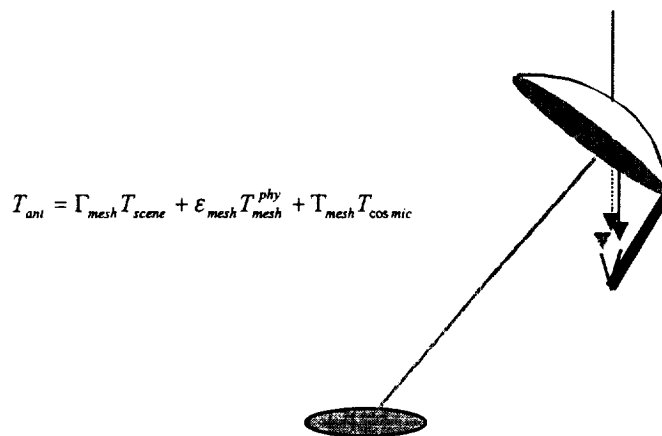
Figure 6.1-1. Effect of radiometric reflector properties.

Measurement goals were developed at the outset to ensure that the performance of the mesh could be adequately characterized in the laboratory. The expression for the antenna brightness temperature in Figure 6.1-1 can be simplified. Since $T_{mesh} = 1 - \Gamma_{mesh} - \varepsilon_{mesh}$ we can write:

$$T_{ant} = \Gamma_{mesh}(T_{scene} - T_{cosmic}) + \varepsilon_{mesh}(T_{mesh}^{phy} - T_{cosmic}) + T_{cosmic}$$

and

$$\Delta T_{ant} = \frac{\partial T_{ant}}{\partial \Gamma_{mesh}} \Delta \Gamma_{mesh} = (T_{scene} - T_{cosmic})\Delta \Gamma_{mesh}$$

$$\Delta T_{ant} = \frac{\partial T_{ant}}{\partial \varepsilon_{mesh}} \Delta \varepsilon_{mesh} = (T_{mesh}^{phy} - T_{cosmic})\Delta \varepsilon_{mesh} \qquad (6\text{-}1)$$

$$\Delta T_{ant} = \frac{\partial T_{ant}}{\partial T_{mesh}^{phy}} \Delta T_{mesh}^{phy} = \varepsilon_{mesh}\Delta T_{mesh}^{phy}$$

Then, an expression for the peak absolute error can be written

$$\Delta T_{ant} = (T_{scene} - T_{cosmic})\Delta \Gamma_{mesh} + (T_{mesh}^{phy} - T_{cosmic})\Delta \varepsilon_{mesh} + \varepsilon_{mesh}\Delta T_{mesh}^{phy} \qquad (6\text{-}2)$$

The following nominal values were assumed: T_{scene} = 100 K (ocean), T_{cosmic} = 3 K, physical temperature of the mesh T_{mesh}^{phy} = 400 K. An error of 0.1 K was allocated for variations in radiometric properties of the reflector, driven mainly by the need for high precision in the measurement of ocean salinity (Section 3). Ignoring for the moment the effect of variations in the mesh physical temperature, and allocating the 0.1 K radiometric error between the emissivity and reflectivity of the mesh, then the following requirements result for measurement accuracy of the reflectivity and emissivity:

$$\Delta \Gamma_{mesh} = \frac{0.03K}{(T_{scene} - T_{cosmic})} = 0.0003$$

$$\Delta \varepsilon_{mesh} = \frac{0.07K}{(T_{mesh}^{Phy} - T_{cosmic})} = 0.0002 \qquad (6\text{-}3)$$

These measurement requirements are very ambitious and may be unnecessary. It is important to consider the goals in terms of the overall system calibration. It is clear that the nominal mesh radiation term will easily exceed 0.1 K. Further, it is unlikely that the mesh can be characterized sufficiently to eliminate the need for an on-orbit evaluation and adjustment of the correction. However, similar non-mesh-related corrections for effects such as beam efficiency and feed spill-over are typically estimated and then verified during the calibration and validation (Cal/Val) phases of the mission. Rather than considering Equation 6-3 as absolute accuracy requirements, it is assumed that nominal values of these offsets will be estimated and evaluated via ground truth calibrations during the satellite Cal/Val operations phase. In this scenario, the issue to be addressed during the mesh characterization is then the stability of the mesh properties. Thus, a realistic approach to developing the performance requirements for the measurement system is to use the values in Equation 6-3 as a stability goal and to provide a more modest absolute accuracy

goal. These measurement goals are delineated in Table 6.1-1. For convenience the approximate antenna brightness temperature (T_{ant}) error associated with each term is included in the table.

Table 6.1-1. Measurement Goals

	Accuracy	Stability	T_{Ant} Bias (K)	T_{Ant} ΔBias (K)
Reflectivity	0.001	0.0003	0.1	0.03
Emissivity	0.001	0.0002	0.4	0.08
Transmissivity	0.01	0.01	0.003	0.003

The error due to emissivity of the reflector has an additional complication due to the variability or uncertainty in the physical temperature of the mesh. Not only must the emissivity be stable but changes in the physical temperature of the mesh must remain small or be known. As shown in Equation 6-2, to estimate the error associated with variation of the physical temperature of the mesh, the emissivity of the mesh must be known. Figure 6.1-2 shows the relationship between mesh emissivity, mesh physical temperature uncertainty, and resulting antenna brightness temperature (T_{ant}) errors. It is important to note that the error shown in Figure 6.1-2 is the uncorrected error due to changes or uncertainty in the mesh temperature. For example, if the nominal emissivity of the mesh is 0.004 and the unknown physical temperature variation or uncertainty on orbit is 5 °C, an uncorrected error of 0.02 K would result. Since our proposed absolute accuracy for emissivity is ±0.001, the uncertainty in prediction of the error is defined by the slope of the lines in Figure 6.1-2, or ±0.005 K for 5 °C physical temperature knowledge. For physical temperature knowledge of 10 °C the uncorrected error would be 0.04 with an uncertainty of ±0.01 K.
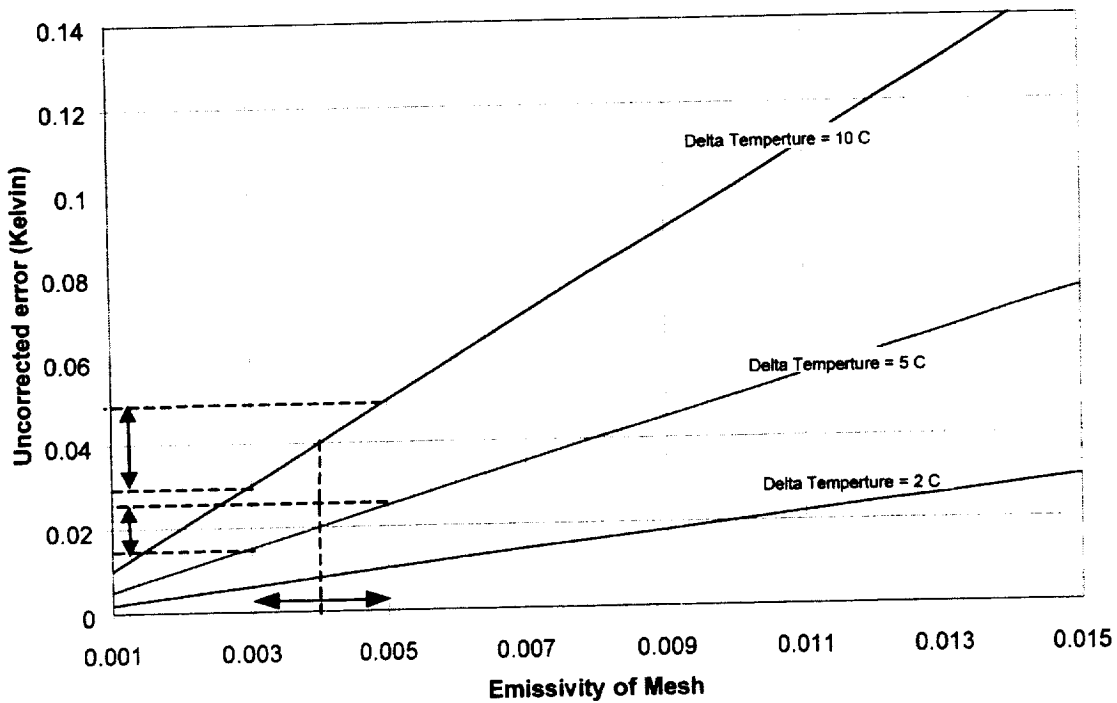
Figure 6.1-2. Effects of mesh physical temperature variations or uncertainty.

6.2 MEASUREMENT APPROACH

6.2.1 Introduction

To be useful for radiometric applications, the emissivity of a reflector surface must be small and the reflectivity near unity. The use of a vector network analyzer (VNA) to measure the scattering parameters (S-parameters), and to thereby infer the surface properties or even the material properties (μ, ε), is well known. However, the measurement of small transmission losses of highly reflective two-ports is very difficult, and typical VNA calibration errors will result in emissivity errors well in excess of the measurement goals of Table 6.1-1. As will be discussed below, a major limitation in the accuracy of such measurements is the effect of source match errors. Earlier efforts to evaluate the emissivity of mesh materials utilized two radiometric approaches to measure the radiation from the sample (Harrington and Blume, 1984). These approaches measure directly the radiation from the sample rather than the portion of a signal reflected and transmitted through a sample. These measurement approaches also fall short of our current goals.

The approach followed here was to improve on the radiometric measurement approach of Harrington and Blume (1984). This represents the principal effort of this study. In addition, an attempt was made to improve the calibration techniques used for VNA measurements.

6.2.2 Radiometric Measurements

In the early 1980's LaRC and the Naval Research Laboratory (NRL) collaborated on an investigation of mesh radiometric properties for a Low Frequency Microwave Radiometer (LFMR) instrument to be flown on the NROSS satellite (later cancelled). This effort developed two approaches that relied on direct measurement of the radiation from the mesh sample. The radiometric measurement approach is fundamentally different from the S-parameter approach in that the former directly measures the microwave emission from the sample.

Some specific error sources must be considered in radiometric measurements. It is desirable to provide a cold background against which to measure the emissions from the sample. This background must be very stable and well characterized (including the reflection coefficient in the case of a cryoload) to ensure that its contribution to the measured brightness temperature can be removed in the data processing/calibration. This background is often provided via a liquid nitrogen cold load (i.e., cryogenically cooled microwave absorber) or by utilizing the cold sky temperature. An additional error source unique to the radiometric approach is that due to the physical temperature of the receiver, the radiometer itself radiates power through the measurement antenna, illuminating the sample. That is, we attempt to measure the power radiating from the sample, corresponding to a nominal brightness temperature on the order of 0.05 to 0.2 K, while the sample is being illuminated at ~3000 times this value by the measurement system. This 'self-radiation' is a major source of error in the radiometric measurement approach and may explain the inconsistencies between the S-parameter and radiometric measurements discussed by Cravey et al. (1995).

One of the techniques developed, the 'Sky Bucket', was an open system that measured a sample placed in front of the radiometer at an incidence angle of 45°. The radiation from the sample was thus measured against the cold sky background. Limitations associated with this concept were the inability to control the physical temperature of the sample, and the correction needed for

diffraction from the sample fixture. A closed system concept to measure emission from the mesh sample was also developed and was used in the mesh testing described by Harrington and Blume (1984). This approach used a flared rectangular horn fitted to a 'test section' that held the sample at an angle of 45° relative to the antenna aperture. The test section was suspended over a cryoload, which consisted of microwave absorber material submerged in liquid nitrogen. This approach basically measured the change in the received power as the physical temperature of the sample was varied. This closed system suffered from variations in the reflection from the cryoload as the nitrogen evaporated as well as the dependence on accurate knowledge of the physical temperature of the sample. A brief discussion of the measurement systems and the results of the LFMR mesh measurement can be found in Harrington and Blume (1984).

The radiometric measurement approach developed here includes modifications to improve the original Sky Bucket approach and add the sample temperature control of the closed system approach. As discussed below, these improvements enhanced the performance of the measurement concept.

6.2.3 Measurement Setup

Since a new radiometer design was used for this application, a thermal electric cooler (TEC) thermal control system was added to improve instrument stability. Internal calibration sources were also provided as well as a separate zenith-viewing antenna that allowed the brightness temperature of the sky to be continuously monitored during a test. The noise power radiated from the radiometer antenna (self-radiation) could also be selected by the user. By changing the noise power radiated from the measurement horn, any changes in the power scattered back into the antenna could be monitored. This capability was very useful as a diagnostic test to verify the proper alignment of the references and sample and to monitor changes in the self-radiation error term. In addition, a lens-corrected antenna was developed to minimize the illumination at the edges of the sample and provide a quasi-uniform phase at the sample to more closely approximate the properties for a transverse electromagnetic (TEM) incident field.

In addition to the improved radiometer, a sample translation unit was designed and fabricated to allow the sample and two calibration/reference plates to be automatically moved in front of the radiometer antenna. This approach provided automated, consistent positioning of the samples and reference plates. Thus, periodic calibration via the reference plates could be performed as often as every 70 seconds at the maximum rate of travel of the positioning system. This sample translation unit included an aluminum reflector 'mask' between the measurement antenna and the translation unit with a single 18 in. × 18 in. aperture through which the samples are viewed. The mask ensured that the measurement antenna was unaffected by changes in the position of the sample translation unit since all measurements took place through the same aperture. The effect of diffraction or scattering from the edge should be the same for the sample and reference plates. This configuration is shown in Figure 6.2-1.

The mask is oriented at 45° and is hinged at the bottom to pivot forward slightly and allow the sample translation unit to move (horizontally and perpendicular to the feedhorn, see Figure 6.2-1). The sample translation unit holds the material sample and two reference plates (nominally aluminum and stainless steel). The sample and reference plates are located behind the mask and are also orientated at 45°. A photograph of the Materials Emissivity Measurement System is shown in Figure 6.2-2 (view from above).

67
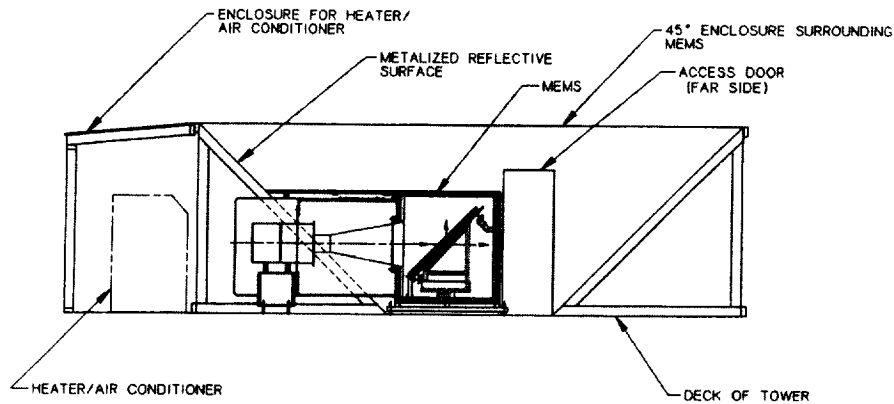
Figure 6.2-1. Schematic of the Materials Emissivity Measurement System.
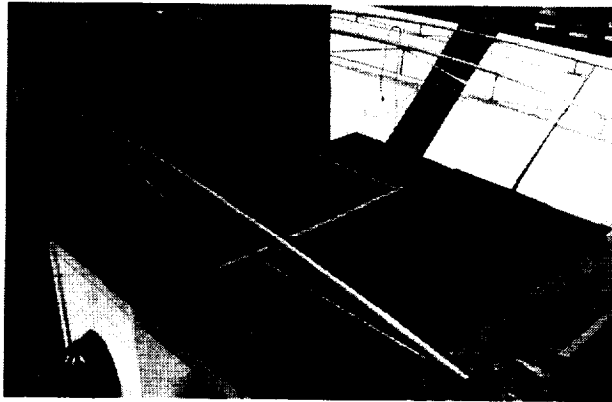
Figure 6.2-2. Photograph of the Materials Emissivity Measurement System (view from top).

Another enhancement was the temperature control system for the samples. The environmental enclosure surrounds the entire sample translation unit (top and front are RF transparent windows). A heating and air conditioning system controls the temperature and humidity within the enclosure. This allowed the emissivity to be measured over a range of physical temperatures.

The general approach was to use the mechanical actuator to insert the sample and reference standards into the beam of the measurement radiometer over time periods short relative to the system stability. This approach allowed differential radiometric measurement to be utilized and eased the stability requirements on the radiometer. The reference plate measurements essentially provided a radiometric calibration at two points very close to the measured brightness temperature of the sample. This calibration not only corrected for radiometer gain and offset but also mitigated the diffraction and scattering errors and the effect of sky temperature variations during the tests. The calibration plates and samples were viewed through the same mask and had similar self-radiation errors. This minimized the effects of the self-radiation error in the final emissivity measurements.

The calibration approach used in the initial measurements assumed that self-radiation and background terms were constant for the calibration reference plates and sample positions. In fact, the apparatus was designed to ensure that the mask edges affected the calibration plate and

68

sample measurements equally and would subtract from the final measurement. However, during the initial testing it was discovered that the variation in the self-radiation and background terms appeared to be due to slight changes in the mask position. The calibration approach was therefore modified to include measurements at the two calibration plates and sample positions with a thin (1/16 in.) aluminum test plate covering the mask aperture. The assumption was then that since the radiometer viewed the test plate for all test positions (i.e., Refl, Ref2, or sample), offset errors due to mask position errors would be measured during this test and could be used to correct subsequent test data.

6.2.4 Vector Network Analyzer Measurements

A vector network analyzer (VNA) is a tool used to measure electromagnetic transmission and reflection characteristics of a device under test (DUT). Here, the DUT is a thin mesh material sample. The transmission and reflection coefficients that are measured by a VNA are also called S-parameters. A brief description of S-parameters is given here (for a more complete discussion, see any standard electromagnetics text). S-parameters are defined as the ratio of transmitted or reflected energy to the incident energy. If the two ports of the VNA are numbered 1 and 2, then S_{11} corresponds to the ratio of the energy reflected back to port 1 from the DUT to the energy that was originally transmitted from that port. S_{21} corresponds to the ratio of energy transmitted through the DUT and received at port 2 to the energy originally transmitted from port 1. S_{22} and S_{12} are called the reverse S-parameters, and are defined similarly for a signal transmitted from port 2 and reflected back into port 2 or transmitted through to port 1.

Using conservation of energy, the amount of energy absorbed in the DUT can be calculated from the reflection and transmission coefficients. Since, for a material in thermal equilibrium, emissivity is equal to the absorptivity, the emissivity of a sample can be found from the S-parameters. Systematic errors inherent in VNA measurements can be eliminated through proper calibration procedures. These procedures differ according to the type of measurement being performed. However, the basic principle is the same, i.e., to measure the system response to a known standard and to account for the difference between the actual response and the ideal response as an error term which must be subtracted from the subsequent measurements of the DUT.

To perform waveguide VNA measurements a sample is mounted on a thin waveguide flange so that the material to be tested occupies the cross section between the waveguide. In this measurement technique, a full two-port waveguide calibration at the measurement plane can correct for the systematic errors associated with directivity, source and load match, and crosstalk. The emissivity E is equal to the absorptivity and is calculated using conservation of energy:

$$E = 1 - (\mid S_{11} \mid^2 + \mid S_{21} \mid^2)$$ (6-4)

A disadvantage of this technique is that a highly reflective DUT contributes to the overall measurement uncertainty because the source match error term is multiplied by S_{11} in the error correction algorithm. Possible errors also result from leakage around the edges of the sample due to uneven thickness in the epoxy used to mount the thin film to the waveguide flange sample holder. These can be reduced by careful sample preparation and by covering the surfaces of the sample holder with conductive tape prior to measurement.

69

6.3 RESULTS

6.3.1 Mesh Samples

The mesh samples used for testing were provided by TRW Astro. Mesh samples of 10 and 20 openings-per-inch (opi) used in existing antenna systems are shown in Figure 6.3-1. Also shown is an 'advanced concept' sample (silver plated spandex) that is being considered for future applications. The plating processes and specific weaves are proprietary to TRW Astro. The mesh samples were prepared with tension fields consistent with nominal tensions of the TRW Astro commercial antenna concept. The advanced concept sample was not tested as part of the current task.

6.3.2 Measurement System Verification

The discussion of the measurement results includes both the evaluation of the system and the actual measured emissivity of the mesh samples. Testing to evaluate the short-term stability of the radiometer and the calibration approach was performed. As discussed earlier, reference plates were viewed intermittently and were used essentially as calibration targets. It is important to characterize the short-term stability of the radiometer to ensure that the minimum time between calibrations is consistent with the radiometer system stability. These calibrations are crucial to the overall measurement precision. Testing and analysis during the initial measurements indicated that the stability of the radiometer receiver was sufficient and the impact of receiver stability error was insignificant compared to the impact of the source match (self-radiation) error.
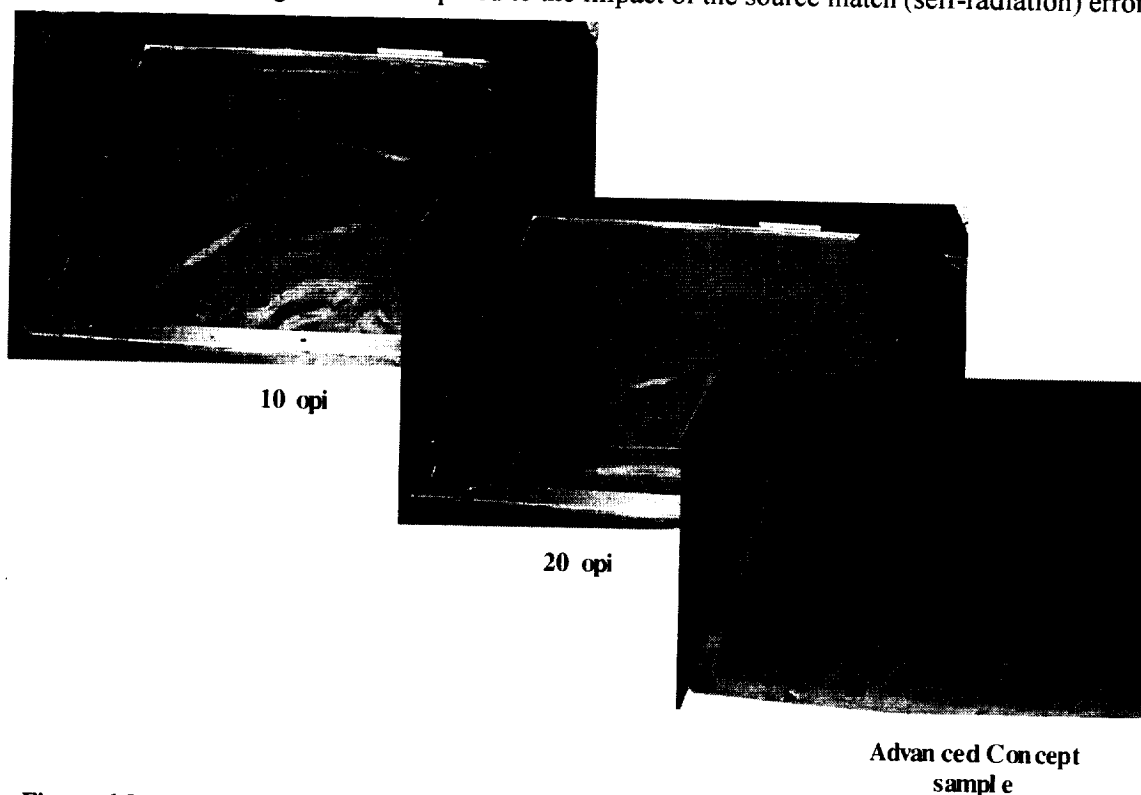
Figure 6.3-1. Mesh samples at 10 and 20 openings per inch (opi), and an advanced concept sample, in mounting frames for testing.

Although the measurement fixture design was intended to minimize the self-radiation error, some differences in this term are expected due to mechanical position errors. One source of this mechanical repeatability error is variation in the mask position as the sample positioner moves between the reference positions and sample position. As discussed earlier, in order to characterize these variations a thin aluminum test-plate was installed to cover the mask as shown in Figure 6.3-2. Any change in the measured brightness temperature between the two calibration positions and the sample position with this test plate in place were assumed to be due to changes in the mechanical position of the mask due to the sample positioner. To assess the impact of these errors and the effectiveness of the calibration/correction approach; the radiometer was calibrated using an external load as shown in Figure 6.3-3.
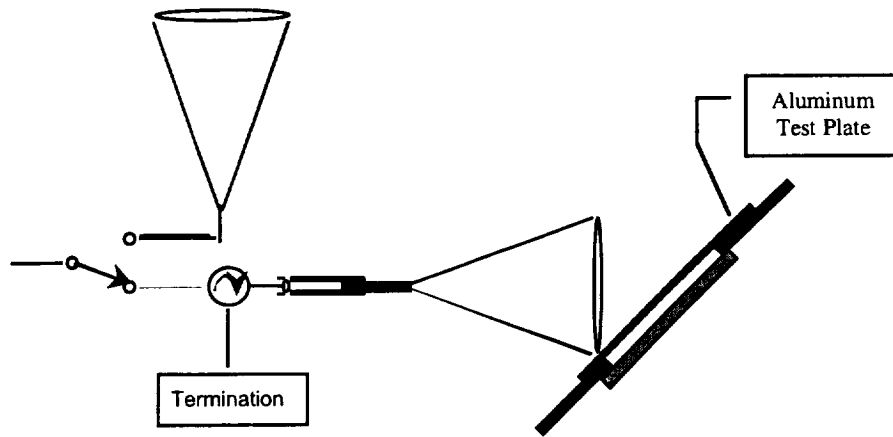
Figure 6.3-2. Test-plate measurement setup.
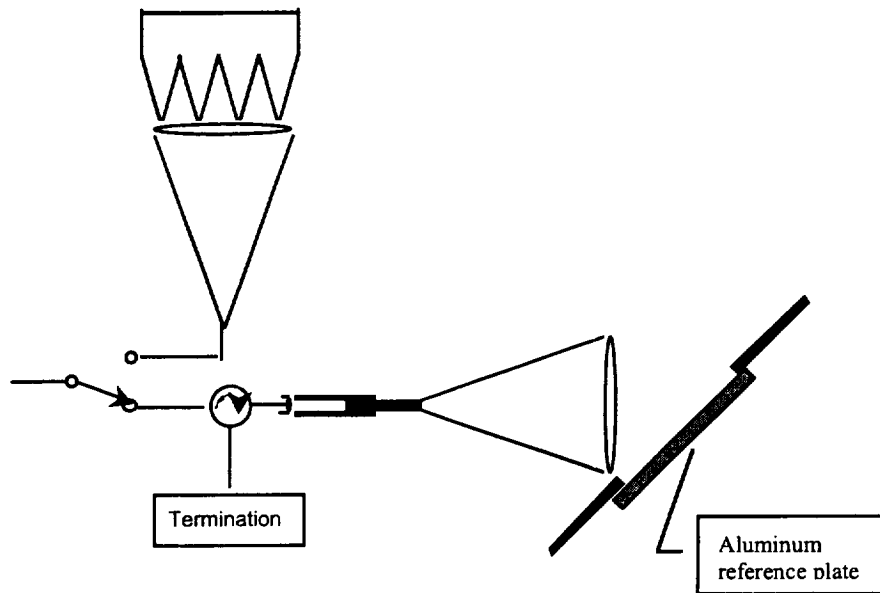
Figure 6.3-3. External warm-load calibration.

71

The warm load used in the external calibration was a section of microwave absorber. Although care was exercised to ensure stability of the absorber temperature, only the surface temperature was recorded. While performance of this load as a calibration target is clearly suspect, the desire was to evaluate the repeatability of the reference plate measurements and the effect of mask position errors rather than an absolute calibration. The radiometer gain was measured by assuming the emissivity of the warm load was unity and that the sky temperature was known. This warm load/sky external gain calibration was performed at the beginning of each evening of testing. The differences between the aluminum reference plate viewed through the mask and the test plate covering the mask are shown in Figure 6.3-4.

The data in Figure 6.3-4 are the offsets from the test plate measurements over several months of testing. The brightness temperatures were found using the gains based on the external calibrations described above, and were assumed to be a worst-case estimate of the error due to mechanical alignment repeatability. Figure 6.3-4 indicates that the radiometric error due to alignment error varied from test to test. This may be due to difficulties of repeatability in installing the samples and variations in the mask position during the tests. In an attempt to characterize the error associated with each test, the aluminum test plate was installed over the mask aperture and repeated sky calibrations were performed at the reference plate and sample positions before and after each measurement. The average measured offset for each reference and sample position were used to provide an estimate of the position-dependent offset in the correction algorithm. Worst case deviations from the average were used to estimate the stability of this correction and were used as error bars for the estimated emissivity.

In order to demonstrate the overall performance of the system, the surface emissivity of the stainless steel reference plate (Ref2) was calculated from the measured data by using the external warm/sky calibration and the difference between the aluminum and stainless steel reference plate data. The results of these reference plate measurements are shown in Figure 6.3-5. The measured emissivity provides an indication of the stability of the measurement system over several months and shows the error bars derived from the test plate characterization of the offset variations discussed above.
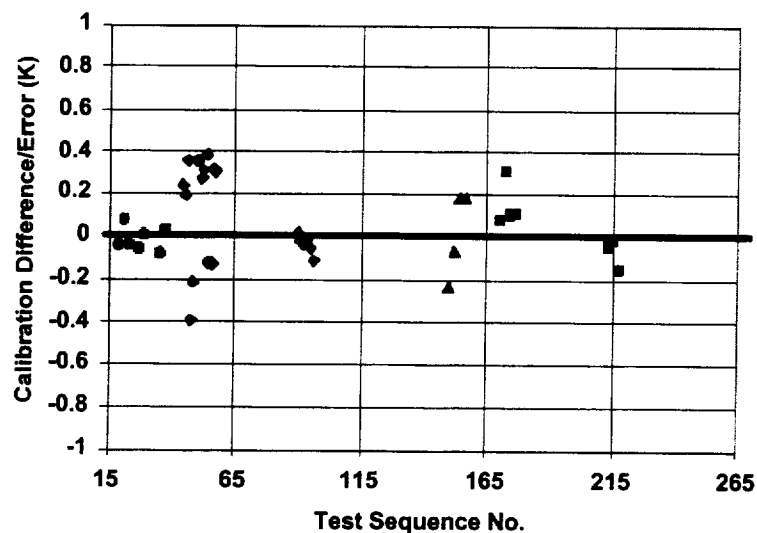
Figure 6.3-4. Effects of mask mechanical position errors.

72
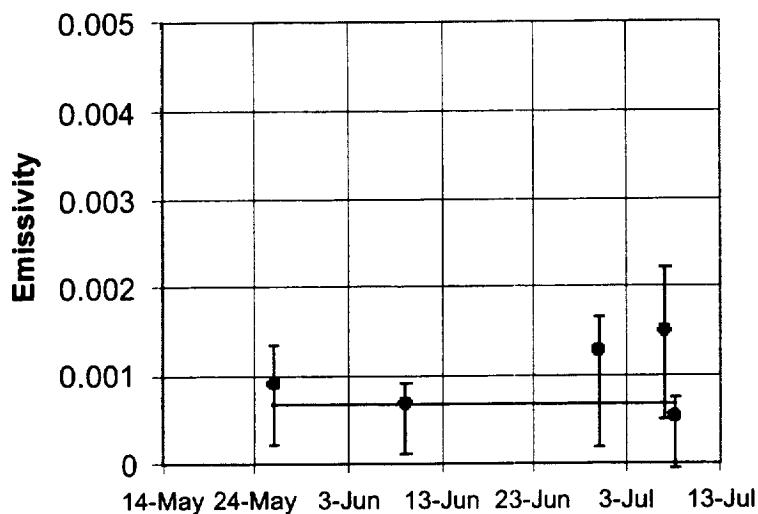
Figure 6.3-5. Reference plate emissivity.

6.3.3 Emissivity Results

VNA measurements were performed using the improved calibration approach discussed earlier. The conventional wisdom was that the VNA measurements would fall well short of the desired accuracy due to source match errors. It was assumed in the error analysis that S_{11} for the measurement was arbitrary. However, for this application S_{11} for the mesh sample measurement and the aluminum reference plate calibration are both very nearly -1. By measuring the emissivity of the mesh relative to the aluminum short, the effect of source-match error is greatly reduced.

Several mesh samples were prepared and mounted in waveguide sample holders. VNA measurements were performed to estimate the emissivity of 10 of these samples. The data shown in Figure 6.3-6 include measurements performed from August through October 2000. While the repeatability was short of the goal, the results far exceeded the estimate for the standard VNA calibration. Except for the results for sample 3, the difference in emissivity between the 10- and 20-openings per inch (opi) samples can be noted. The results for sample 3 are troubling. As can be seen in the figure, the measurements were very repeatable. A physical inspection of the sample did not reveal any noticeable difference in the mesh or bonding of the sample. The boxes superimposed on the data group the results for the 10-opi and 20-opi samples. However, as can be noted in the figure, the test repeatability errors obscured any effect on emissivity due to differences in mesh tension.

The results of the VNA and radiometric measured mesh emissivity are shown in Figure 6.3-7. These data include multiple samples for both the radiometric and VNA measurements performed over several months. The samples for the VNA and radiometric measurements, while the same type of mesh, are different physical samples. The agreement between the radiometric and VNA measurements is quite good and much better than would be expected without the improved VNA calibration approach. These results indicate much closer agreement between the radiometric and VNA results than reported in Cravey et al. (1995), perhaps due to the reduction in errors

73
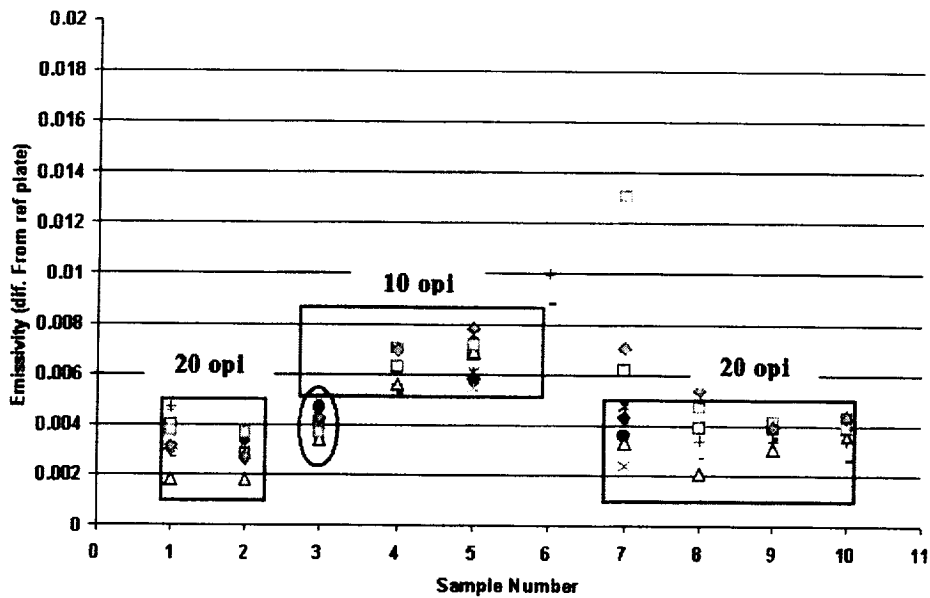
Figure 6.3-6. VNA waveguide mesh measurements.
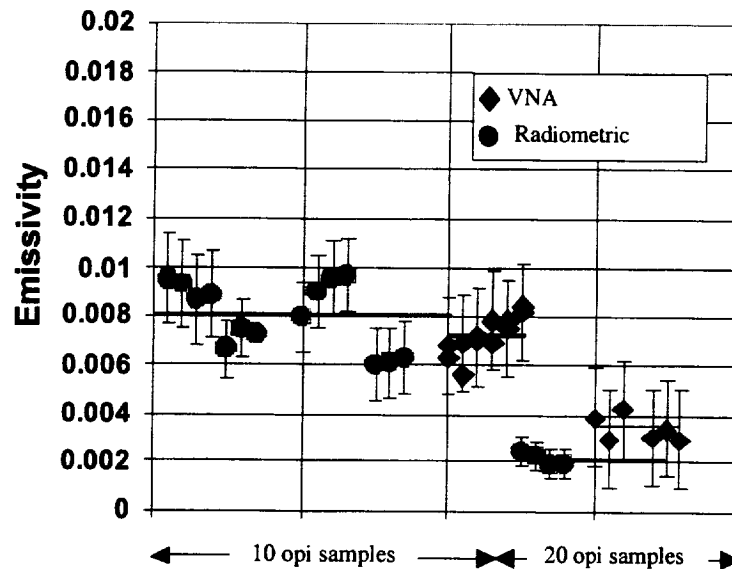
Figure 6.3-7. Radiometric and VNA emissivity results.

associated with self-radiation. Several observations can be made from the data presented in Figure 6.3-7. Most importantly, the data can be used to estimate the nominal emissivity of 10-opi and 20-opi mesh. The measured emissivities for all 20- and 10-opi mesh samples were averaged independently for the radiometric and VNA techniques. These averages are shown in Table 6.3-1. Note these averages include all samples for the density of weave regardless of tension.

74

Table 6.3-1: Averaged Mesh Emissivity Results

Estimated Emissivity	20 opi samples	10 opi samples
Radiometric	0.0022 (+/- 0.0006)	0.0080 (+/- .002)
Waveguide VNA	0.0034 (+/- .002)	0.0072 (+/- .002)

The estimated emissivity uncertainties shown in Table 6.3-1 are the root-mean-square of the standard deviation of the measurements and the average of the error bars for each measurement.

It should be noted that the repeatability of the measurements was insufficient to determine the effects of variations in tension or physical temperature of the mesh. The testing of these effects will depend on implementation of approaches to further improve the repeatability of the measurements. These are being performed as an extension of the present task.

6.3.4 Application to the OSIRIS Instrument

An important question is how the emissivities of mesh materials shown in Table 6.3-1 will impact the performance of the OSIRIS instrument. As discussed earlier, the antenna temperature error due to the finite emissivity of the mesh reflector can be considered as two terms. First, errors in the measured antenna temperature can occur as a result of variations of the properties of the mesh surface; i.e., due to changes in the physical temperature or mesh tension. As discussed above, these effects are small, and are currently below the estimated accuracy of the measurement system. Second, changes in the physical temperature of the mesh will result in changes in the measured antenna temperature. To investigate this it was necessary to have a means for estimating the variability and knowledge uncertainty of the mesh physical temperature in orbit. A thermal analysis was performed by JPL's Team-I (Jeff Hall) to simulate the temperature distribution of the mesh surface in orbit. Results from the Team-I study are presented below.

6.4 MESH THERMAL ANALYSIS

A thermal analysis was performed to obtain predicted temperature distributions and time history of the antenna mesh in order to judge the impact on the overall instrument performance. The analysis consisted of both hand calculations and numerical modelling using a software package called Thermal Desktop. Thermal Desktop features an AutoCad-based graphical user interface, a Monte Carlo strategy for computing radiation view factors, and an interface to a SINDA computational engine for calculating time-dependent nodal temperatures.

The spacecraft was defined to be in a 600-km Sun-synchronous, circular orbit with a 6 am ascending node. The resultant orbital inclination is 98°. Given this orbit, the spacecraft will be continuously illuminated by the Sun except for brief occultation intervals over a 1-month period centered on winter solstice. Consequently, the thermal analysis considered two cases: continuous spacecraft illumination (chosen to be the vernal equinox) and the worst-case occultation (winter solstice).

6.4.1 Model Description and Assumptions

The AstroMesh antenna is a deployable microwave reflector with a nominal diameter of 6 meters. The mesh is comprised of gold coated molybdenum wire stretched into a parabolic shape. The vendor (TRW Astro) reported the alpha-to-epsilon ratio (solar absorptivity to infrared emissivity

75

ratio) of this mesh to be 0.28/0.04 = 7. The parabolic shape is created by a complex truss structure composed of graphite tubes around the perimeter, flat kevlar ribbons forming a top and bottom web, and tension tie assemblies connecting the two kevlar webs at each node. In operation, the perimeter truss anchors the top and bottom web, while the tension ties deform the web into the desired parabolic shape. The mesh itself is stretched across one web, essentially acquiring the shape into which the web has been deformed. In orbit, this antenna assembly is connected to the spacecraft with an articulated tubular arm. The antenna, arm, and top portion of the spacecraft spin at 6 rpm with the nadir direction parallel to the spin axis. The bottom part of the spacecraft is despun.

There are three key questions addressed by this thermal analysis:

(1) What is the mean temperature of the antenna mesh during an orbit?

(2) What is the time variation of the mesh temperature during an orbit?

(3) What mechanical distortions arise from spatial temperature gradients across the antenna?

The mechanical complexity of the antenna motivated a number of simplifying assumptions during the analysis. The approach taken was to ignore the antenna truss structure and model only the microwave reflecting mesh. The justification for this comes in three parts: (1) The truss is highly 'porous' to incoming sunlight and IR radiation. For example, the kevlar webs block only 3–4% of the incoming sunlight in the normal direction, the perimeter truss blocks approximately 4%, and the tension ties block roughly 10–15%; (2) the fast spin rate of the antenna (6 rpm) means that the external heating of the mesh will be 'smeared' out, with no part of the mesh being either continuously in shadow or continuously illuminated (except for the points of contact between mesh and webbing); and (3) TRW Astro reported that ground testing of their prototype antenna demonstrated less than 0.08-mm distortions due to both bulk thermal changes of +150 K and spatial gradients of 300 K from top to bottom. This remarkable performance is due to the use of very low coefficient of thermal expansion (CTE) materials (graphite struts) and clever design. This level of distortion is easily tolerable in the current application, and therefore it was decided not to further pursue the distortion question during this phase of analysis.

The mesh itself was modelled as a continuous thin membrane, rather than as a vast collection of tiny wires, in order to have a more tractable model for analysis. This membrane was given the alpha-to-epsilon ratio of gold-plated molybdenum and assigned a thickness of 0.1 mm, a value that roughly approximates the overall mesh mass and hence the thermal capacity.

Figure 6.4-1 shows this mesh membrane in orbit about the Earth. The mesh was discretized into 361 planar elements for the analysis. Heating inputs include the Sun, Earth IR, and Earth albedo.

6.4.2 Vernal Equinox Analysis (Non-occulting Orbit)

Figure 6.4-2 shows the temperature distribution of the mesh averaged over a single orbit for the vernal equinox. Figure 6.4-3 shows the temperature versus time traces over 3.5 orbits for the three nodes labelled on Figure 6.4-2, which roughly correspond to the bottom, center, and top of the mesh. It can be seen that the bottom of the mesh, near the attachment point with the arm, is the hottest region, averaging approximately 430 K. Conversely, the coldest part is at the opposite end (the top) which has a temperature of approximately 320 K. The difference is due to the fact
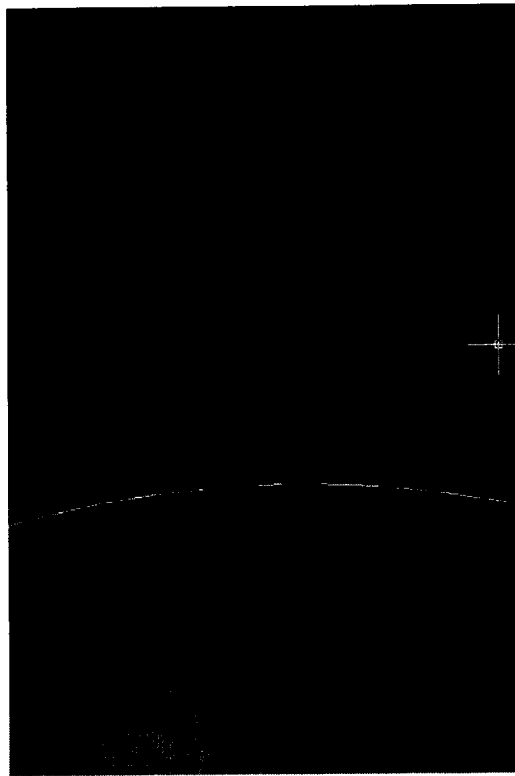
Figure 6.4-1. Antenna mesh shown in orbit.
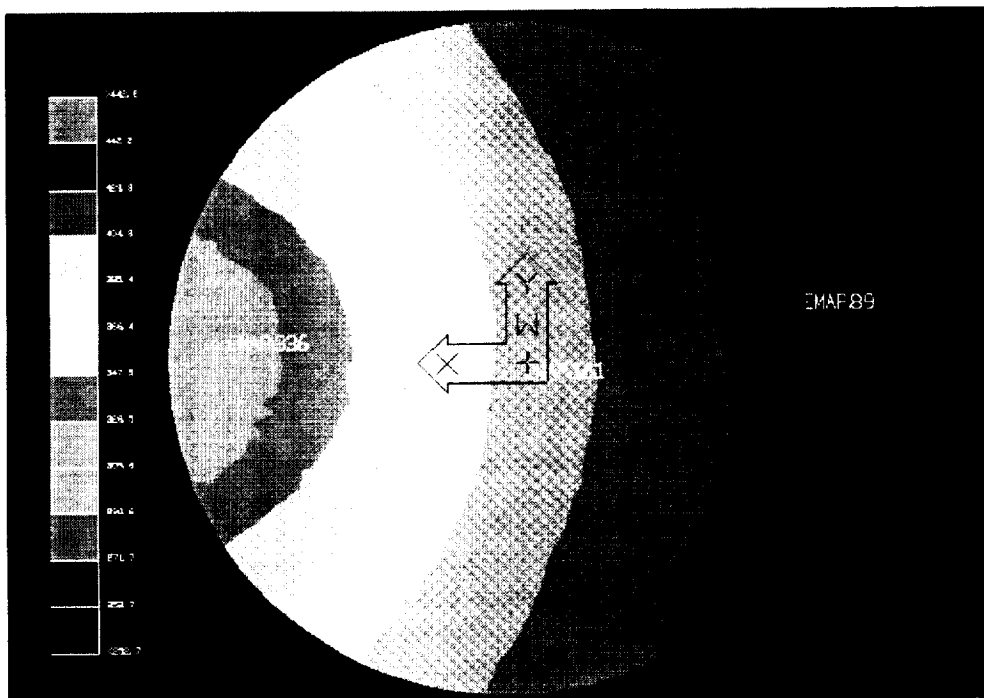
Figure 6.4-2. Vernal equinox average temperatures.
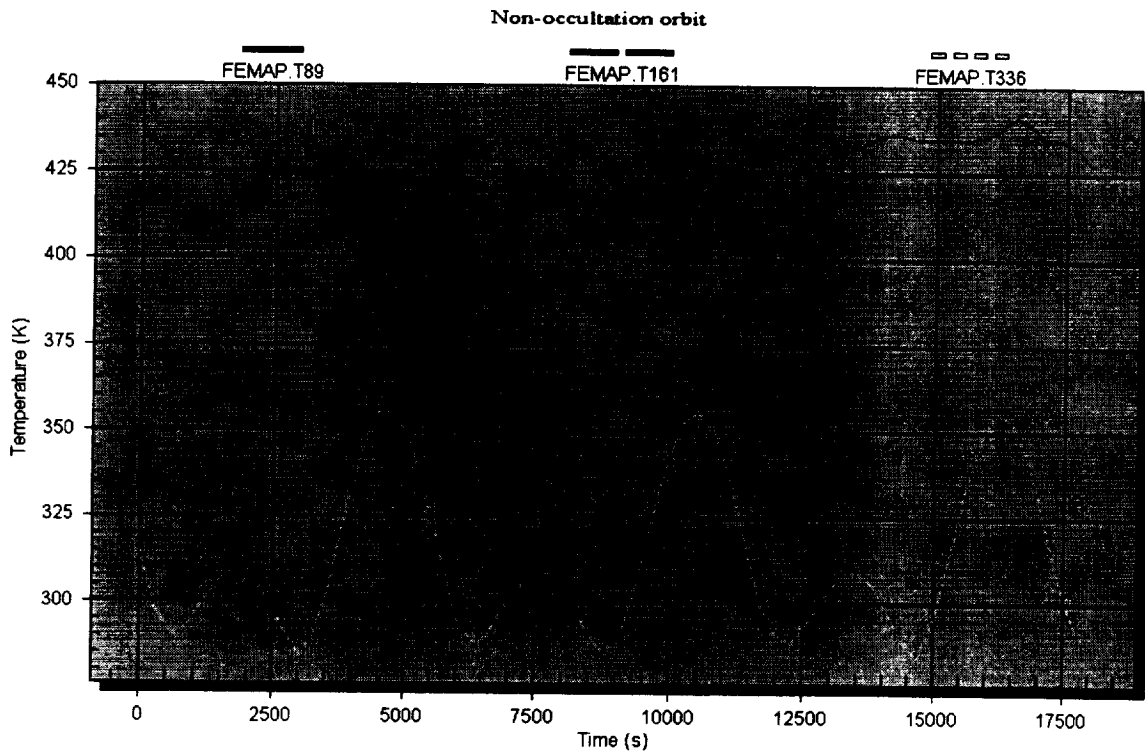
Figure 6.4-3. Vernal equinox T(t) plots.

that with this antenna shape, orbit, and orientation, the sun better illuminates the bottom of the mesh as compared to the top. In particular, the top of the antenna is almost edge-on to the Sun for much of the orbit and receives relatively little solar heat. As a result of oscillating between being nearly edge-on to the Sun and being partially illuminated, the top of the mesh shows the largest temperature variations in orbit, amounting to ±40 K. Conversely, the center and bottom of the mesh experience only ± 5- to 10-K variations.

The above temperatures represent upper bounds on mesh temperatures and temperature variations due to the absence of shading effects from the surrounding structure. Even if shading effects were incorporated, however, these predicted temperatures would not decrease very much given only a ~20% shading factor and a T^4 dependence of heating on temperature $(0.8^{.25} = 0.95)$.

6.4.3 Winter Solstice Analysis (Occulting Orbit)

Figure 6.4-4 shows the temperature distribution on the mesh averaged over a single orbit for the winter solstice. Figure 6.4-5 shows the temperature versus time traces over 3.5 orbits for the three nodes labelled on Figure 6.4-4, which again correspond to the bottom, center, and top of the mesh. In contrast to the vernal equinox case discussed above, illumination of the mesh is more consistent here, leading to more uniform average mesh temperatures. However, although the average temperatures are more uniform, the instantaneous spatial temperature gradients can approach 100 K top to bottom, as seen in Figure 6.4-5, at the time just before occultation (t ~ 3500 s).

78
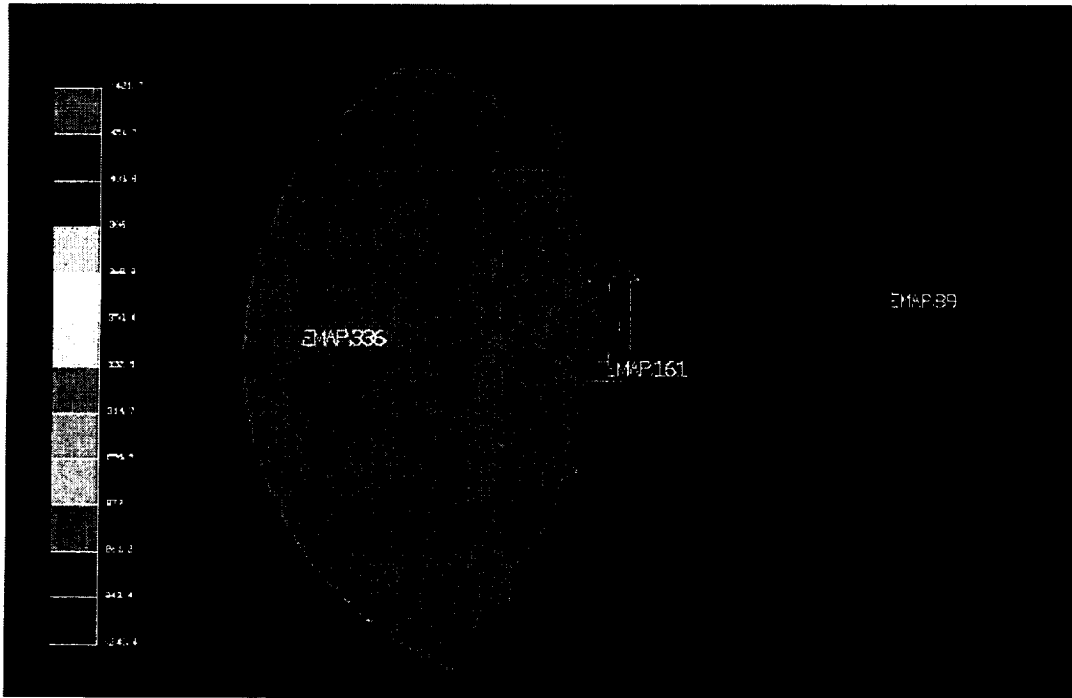
Figure 6.4-4. Winter solstice average temperatures.
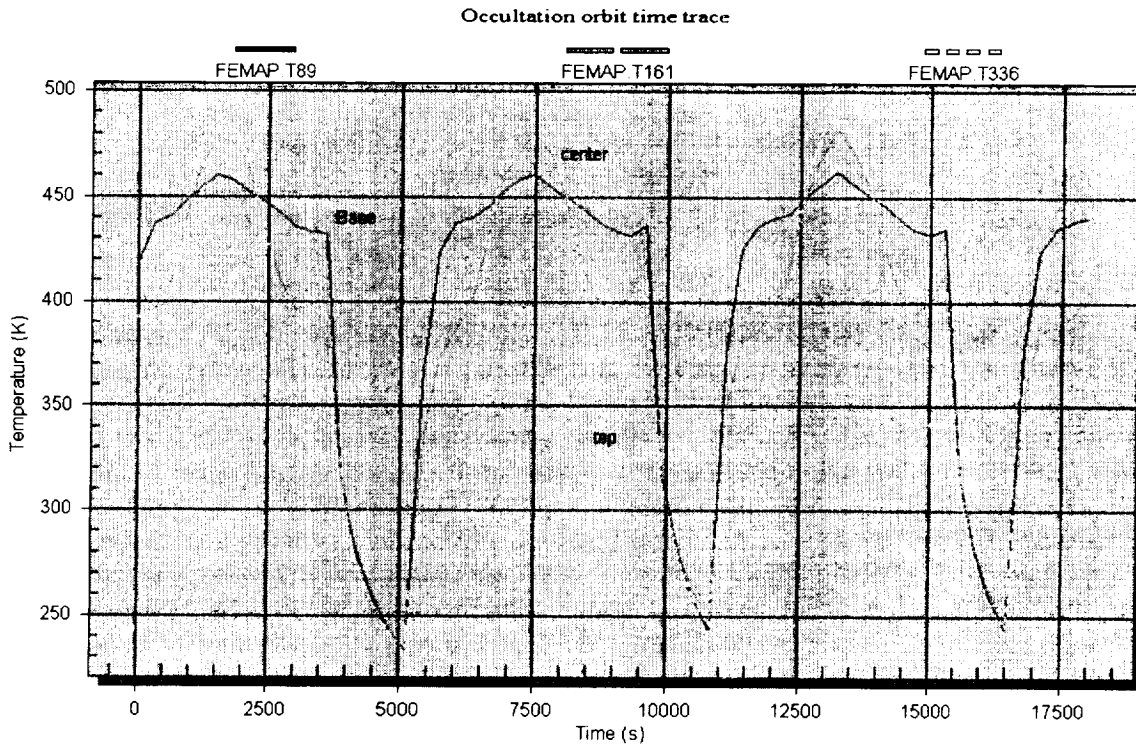
Figure 6.4-5. Winter solstice T(t) plots.

79

Quite noticeable in Figure 6.4-5 are the ~20-minute occultation periods starting at 3700, 9500 and 15300 seconds. The temperature of the entire mesh drops very rapidly, achieving a value of approximately 230 K by the end of the occultation. This ~200 K temperature drop is an upper-bound prediction on the actual device since the higher thermal capacity structure surrounding the mesh will serve to attenuate such large temperature changes.

6.4.4 Antenna Temperature Error

To estimate the antenna brightness temperature error due to changes in the physical temperature of the mesh, the temperatures of the three nodes were averaged to provide a representative 'effective' physical temperature of the reflector surface. This provides a worst-case estimate since the radiation received by the feedhorns weights the temperature variations near the center of the reflector more than at the edge due to the aperture taper, and the largest changes occur at the top edge of the reflector. From Figures 6.4-3 and 6.4-5, an average physical temperature of about 380 K is obtained for both vernal equinox and winter solstice cases, with a peak-to-peak deviation of 40 K for the vernal equinox (non-occultation orbit) and a peak-to-peak deviation of 245 K for the winter solstice (occultation orbit).

From these estimates and the emissivity values shown in Table 6.3-1, a nominal contribution from the mesh of roughly 1 K for the 20-opi and 3 K for the 10-opi mesh would be expected. The peak-to-peak deviations from this nominal value due to physical temperature changes of the mesh reflector are shown in Table 6.4-1 for both the non-occultation and occultation orbit. The values in Table 6.4-1 represent the uncorrected peak-to-peak error due to changes in the physical temperature of the mesh reflector during an orbit. The two values listed in the table for each mesh type and orbit correspond to the waveguide VNA and radiometric emissivity measurements, and can be viewed as an expected range of values (given the uncertainty of the measurements).

Table 6.4-1. Radiometric Peak-to-Peak Error Due to 'Uncorrected' Mesh Temperature Variations

Orbit	20 opi mesh	10 opi mesh
Vernal Equinox	0.09 K $\Rightarrow$ 0.14 K	0.29 K $\Rightarrow$ 0.32 K
Winter Solstice	0.54 K $\Rightarrow$ 0.83 K	1.76 K $\Rightarrow$ 1.96 K

The radiometric peak-to-peak error shown in Table 6.4-1 is the residual temporal variability assuming that the constant bias offset is removed, along with other systematic calibration biases, during the post-launch Cal/Val effort. Given this assumption, several observations can be made. First, dense meshes (20 opi or greater) are desirable for the OSIRIS reflector due to their lower emissivity. Second, the peak-to-peak uncorrected error of ~0.1 K for the vernal equinox using 20-opi mesh is excellent performance for soil moisture applications. Even the worst-case winter solstice results are adequate since the targeted brightness temperature accuracy requirement for said moisture is 0.7 K (Table 3.3-1). With 10-opi mesh the soil moisture retrievals may experience some degradation during portions of the winter solstice orbits. Even for the 20-opi mesh, however, the errors are larger than desired for salinity retrieval.

The discussion above applies to the 'uncorrected' errors. Since the orbit is Sun-synchronous, the mesh physical temperature variations repeat with only slight changes from orbit to orbit and, hence, are to a large extent predictable. Thus, it is quite feasible that the temperature variability on orbit can be modeled or determined empirically using careful on-orbit analysis. If this can be

done to an accuracy of even 20%, then the errors shown in Table 6.4-1 can be reduced by a factor of five as shown in Table 6.4-2. These errors may be acceptable for ocean salinity sensing, although some degradation will still occur at the winter solstice where the largest thermal transients occur during eclipses. It should be noted that an in-orbit calibration bias and variability correction as described above is usually necessary in microwave radiometry. For instance, Wentz et al. (2001) describe the method used for correcting the Tropical Rainfall Measuring Mission Microwave Imager (TRMM/TMI) data. The TMI antenna has an emissivity as high as 0.03, yet the corrections are precise enough to retrieve reliable sea surface temperatures, requiring brightness temperatures of ~0.2 K precision or better.

Table 6.4-2 Potential Radiometric Peak-to-Peak Error Due to 'Corrected'
(20% accurate) Mesh Temperature Variations

Orbit	20 opi mesh	10 opi mesh
Vernal Equinox	0.02 K $\Rightarrow$ 0.03 K	0.06 K $\Rightarrow$ 0.07 K
Winter Solstice	0.11 K $\Rightarrow$ 0.17 K	0.35 K $\Rightarrow$ 0.39 K

6.5 CONCLUSIONS

A Materials Emissivity Measurement System facility was developed at the NASA LaRC to perform precision radiometric and vector network analyzer measurements of the emissivity of commercial mesh samples. The measurement system improved on an earlier system developed at LaRC in the 1980s for similar purposes. The measured emissivities were ~0.003 ($\pm$0.001) and 0.008 ($\pm$0.002) for meshes of 20 and 10 openings per inch, respectively. The denser weave (20 opi) exhibits a lower emissivity. The effects of varying tension or temperature on the mesh emissivity were not measurable within the accuracy of the measurement system.

A thermal analysis of the reflector mesh was performed using a membrane model with appropriate materials characteristics and in-orbit simulated heating inputs (Sun and Earth). The results showed an average mesh temperature of 380 K, and peak-to-peak deviations of $\pm$20 K for the vernal equinox (best case) and $\pm$122 K for the winter solstice (worst case). For the 20-opi mesh these 'uncorrected' temperature variations give rise to peak-to-peak errors of $\pm$0.06 and $\pm$0.37 K for the best and worst cases, respectively. This is acceptable for measurement of soil moisture but not for salinity measurement. For a Sun-synchronous orbit, however, given the repeatability of the mesh temperature variability from orbit to orbit, the variability should be predictable to at least 20% or better. In this case the 'corrected' temperature variations would give rise to peak-to-peak errors of $\pm$0.012 and $\pm$0.074 K, respectively (a factor of five improvement). These errors are acceptable for salinity measurement, particularly since the worst-case (winter solstice) results are due to eclipse periods that are of short duration compared to the annual cycle, such that the measurements are degraded for a limited period of time.

81

7. RADAR ELECTRONICS

7.1 INTRODUCTION

For a mechanical spinning instrument, it is critical to keep the mass low to ease the requirements for spacecraft momentum compensation. This part of the OSIRIS study was conducted to identify radar designs with advanced space-qualified electronics to meet the mass and volume specifications and performance requirements. This section describes in detail the radar parameters, detailed design and layout of the electronics, and power and volume estimates of an L-band radar for an ocean surface salinity and soil moisture mission.

7.2 SPECIFICATIONS

As described earlier, the OSIRIS baseline concept consists of a 6-m diameter conically scanning antenna with a low-frequency microwave radiometer and radar operating at 600-km orbit altitude. For this orbital configuration, a geometric configuration study was conducted with an orbit propagator and antenna geometry to determine the key radar parameters, including transmit power, transmit bandwidth, pulse length, receiver bandwidth and range gate (Table 7.2-1). The transmit power level of 100 W was determined to provide an adequate signal-to-noise ratio (SNR) for the expected radar backscatter level from ocean and soil surfaces at L-band. A study of the radar sensitivity (Kpc), the percentage error of the measurements due to a limited time-bandwidth product and SNR, showed that the selected parameters could meet the 0.2 dB sensitivity requirements determined from the retrieval simulation and error analysis study (Section 3).

Table 7.2-1. Key Radar Parameters

Spacecraft altitude	600 km
Antenna spin rate	6.1 rpm
Antenna diameter	6 m
Antenna peak gain	36 dB
Beamwidth	2.75°
Number of antenna feeds	2
Antenna look angle	36°, 37.9°
Incidence angle	40.1°, 42.3°
Footprint size (3 dB, 1 way)	52 km x 40 km
Polarization	VV, HV, HH, VH
Transmit power	100 W
Transmit frequency	1.25 GHz
Transmit chirp bandwidth	4 MHz
Transmit pulse length	1 ms
Transmit pulse repetition frequency	100 Hz
Receiver bandwidth	1 MHz
Range gate width	1.24 ms
System noise temperature	900 K
Signal-to-noise ratio for −40 dB sigma0	2 dB
Kpc per pulse	< 0.2 dB
Radar calibration stability	0.2 dB
Radar calibration bias accuracy	1 dB
Instantaneous signal bandwidth	933 KHz
ADC	12 bits
Data rate	7 kbps

With the indicated configuration, the two-way 3-dB beam spots for the radar provide complete along-track coverage as shown in Figure 7.2-1. The spacing between adjacent spot centers is about 6 km. Near the edges of the swath, there is more overlap.
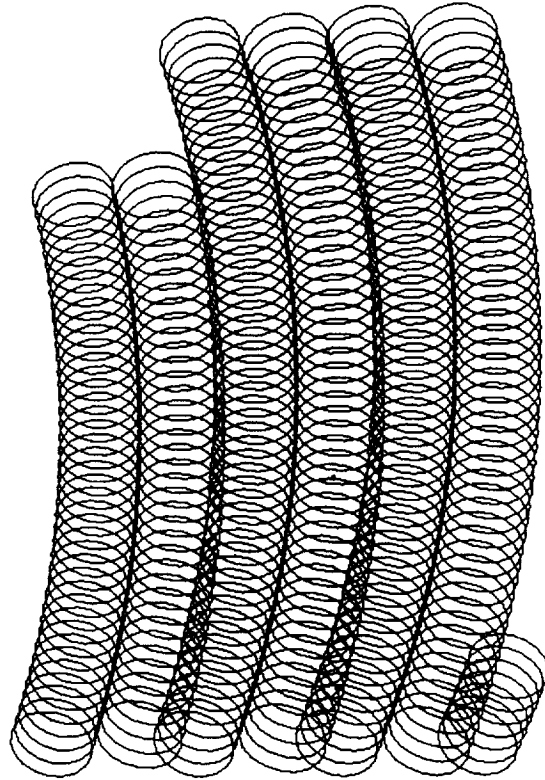
Figure 7.2-1. Radar footprints for inner and outer antenna beams for several antenna scans.

The range for the two beams is 780 km and 800 km respectively, and the round-trip flight time is about 5.2 ms. With a 1-ms pulsewidth, and without resorting to multiple pulses in flight, the maximum pulse repetition rate (PRF) for the radar is 160 Hz. To allow the radiometer a greater fraction of the pulse interval, we show a possible timing chart in Figure 7.2-2 using a PRF of 100 Hz. The extra time after the receive gate is available as integration time for the radiometer, as is the time between the transmit pulse and received echo. These time intervals will also be used to calibrate the noise floor of the radar. The radar duty cycle in this case is about 0.22.

Figure 7.2-3 shows the detailed timing variation around one orbit. The times t1, t2, t3, and t4 are labeled in Figure 7.2-2. They refer to the receive gate with the zero point being the start of the transmit pulse. Scan loss is quite low (-0.02 dB) because of the slow antenna rotation rate. Figure 7.2-4 shows the range gate variation around one orbit for both beams. A fixed value of 1.24 msec will work for both. Figure 7.2-5 shows the orbital variation of the instantaneous signal bandwidth due to the chirp and range variation across the two-way 3-dB spot. From this we see that the sampling rate of the A/D converter will need to be at least 2 MHz. For a fully polarimetric system, I-Q channels will be needed for both H and V polarized receivers. With both I and Q available, the sampling rate can be reduced to 1 MHz.

84
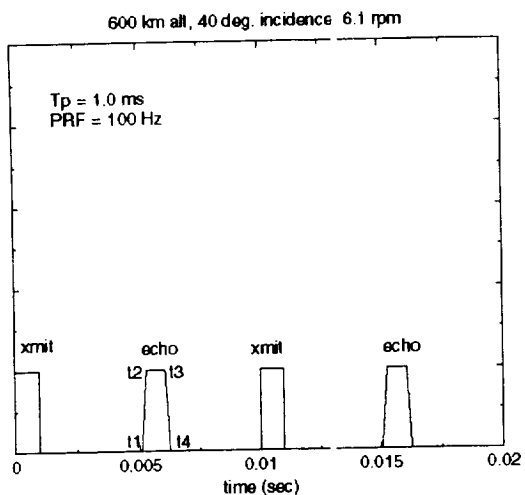
Figure 7.2-2. Radar transmit pulse and echo return times.
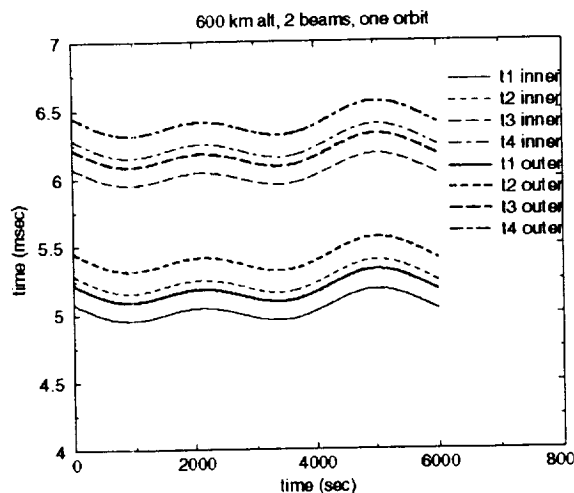
Figure 7.2-3. Variation of the echo return times versus orbit time.
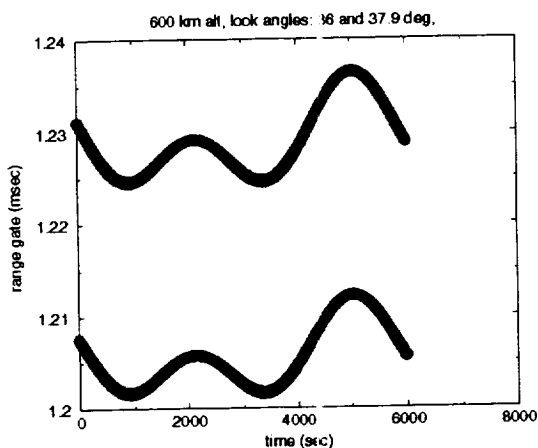
Figure 7.2-4. Optimal range gate versus orbit time.
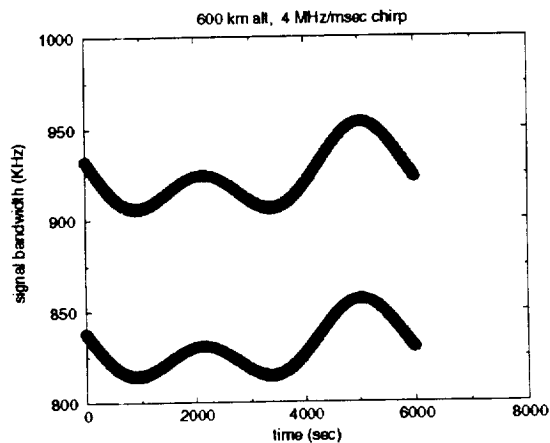
Figure 7.2-5. De-chirped echo bandwidth versus orbit time.

7.3. DESIGN

7.3.1 RF Electronics Design

Design Overview

The RF Electronics Subsystem (RFES) block diagram is shown in Figure 7.3-1. The transmitted waveform is a 4-MHz bandwidth, 1-ms long, linear FM chirp that is generated at a center frequency of 70 MHz by a digital chirp generator (DCG). This signal is then mixed up to the operating frequency, 1.25 GHz, where it is filtered and amplified to a power level of 120 W

85
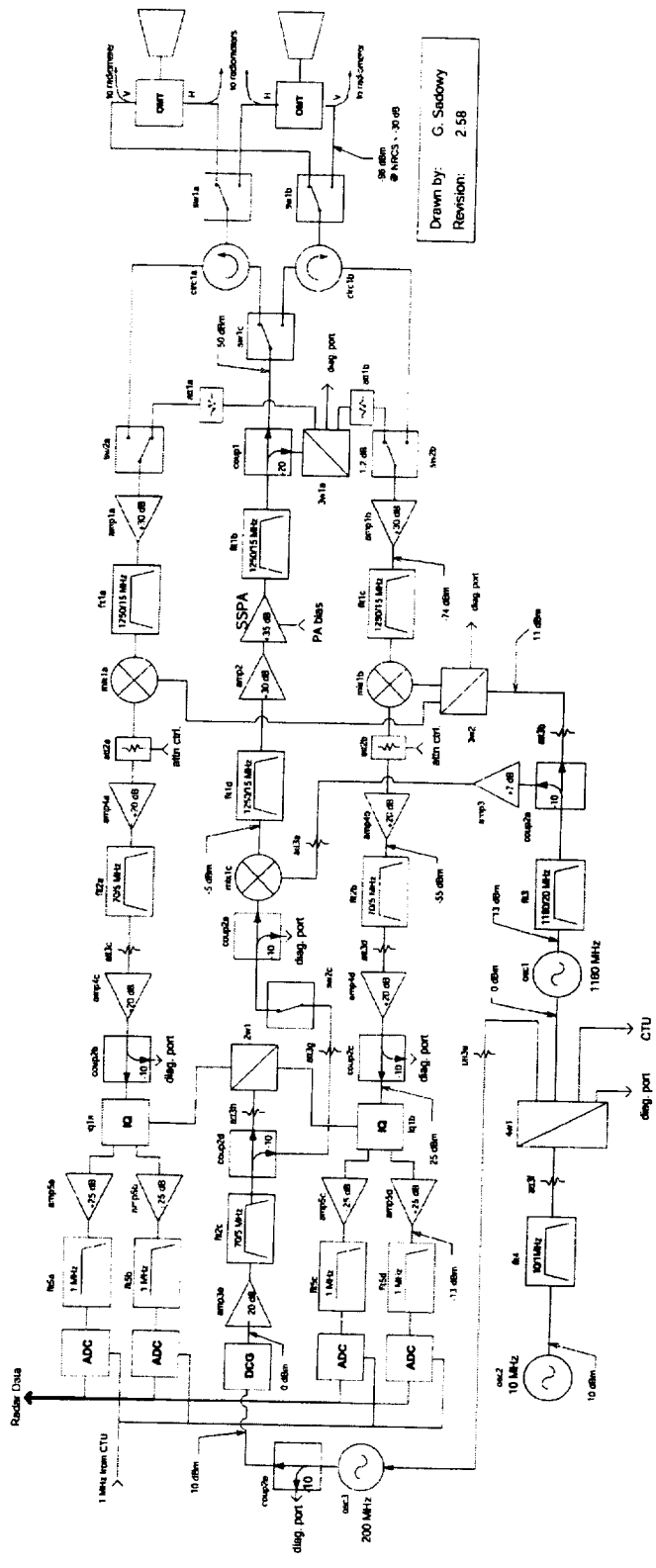
Figure 7.3-1. RFES block diagram.

by a solid state power amplifier (SSPA). Three high-power single pole double throw (SPDT) PIN diode switches are then used to select the transmit polarization and one of two antenna feeds. A small portion of the transmit power is coupled through a calibrated attenuator into each receiver for calibration purposes.

Received signals are routed from both polarization ports on the chosen antenna feed to the receiver channels. The receiver is a single-conversion superheterodyne design with a 70-MHz intermediate frequency (IF). The first down-conversion is accomplished by mixing the received signals with a fixed local oscillator (LO) at 1180 MHz. This LO is phase-locked to the 10-MHz radar master oscillator (MO). The 70-MHz IF signal is amplified and filtered to a 4-MHz bandwidth. The signal is then converted to baseband and deramped by I-Q detectors that are fed with a chirped local oscillator. This chirped LO is generated by the same DCG that generates the transmit signal.

Front-End Electronics

The front-end electronics must route transmitter signals to either polarization port on either antenna feed during the transmit interval and route received power from both ports on either antenna feed to both radar receivers as well as both radiometers during the receive interval. The primary design goal was to accomplish the required signal routing while minimizing loss, particularly in the path from the antenna to the radiometer inputs. Low-loss, high-power PIN diode switches are used to select transmit polarizations as well as the antenna feed because these switches must carry the full transmitter output power. The radiometers are connected to the antenna ports via frequency-selective diplexer filters that are tuned to reject signals at the radar operating frequency. This is preferred over using additional PIN switches for reliability reasons and could potentially offer lower losses. However, if the loss of a sufficiently small diplexer filter is found to be too high, another high-power PIN switch may be used instead.

Transmitter Chain

The transmitter chain begins with the DCG, which creates the chirped waveform. The DCG developed by the JPL Advanced Radar Technology Program (ARTP), shown in Figure 7.3-2, is based on a direct digital synthesizer (DDS) hybrid produced by Stanford Telecom. This board is capable of output frequencies of up to 400 MHz using a 1-GHz clock but, in this implementation, a 200-MHz clock and 70-MHz output frequency were used in order to reduce DC power consumption. The 200-MHz DCG clock is a phase-locked crystal oscillator that is slaved to the 10-MHz MO in order to preserve phase coherency of the system.

The output of the DCG is mixed with an 1180-MHz LO to create the 1.25-GHz transmit frequency. This signal is filtered to remove the opposite sideband and then amplified by MMIC driver amplifiers. The output of the driver amplifiers is fed to the SSPA. There are several available high-efficiency pulsed-power transistors capable of producing sufficient output power. Figure 7.3-3 shows a 200 W SSPA that is 45% efficient and could easily be adapted for operation at 120-W power output.

Receiver

The receiver is connected to the front-end at a PIN diode switch that is used to select the calibration signal during the transmit interval and the antenna signal during the receive interval. The low noise amplifier that follows this switch has sufficient gain to overcome the noise
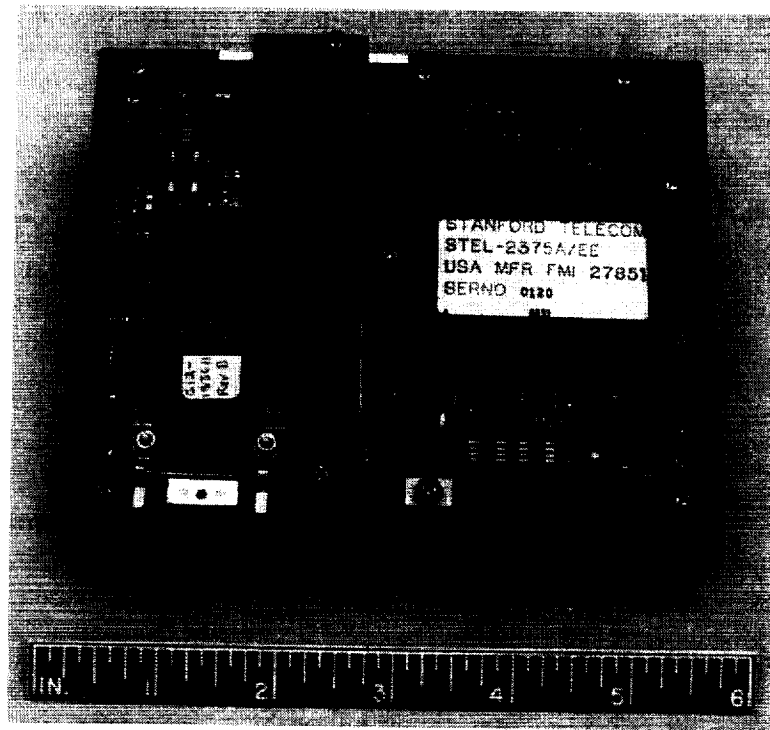
Figure 7.3-2. ARTP digital chirp generator.
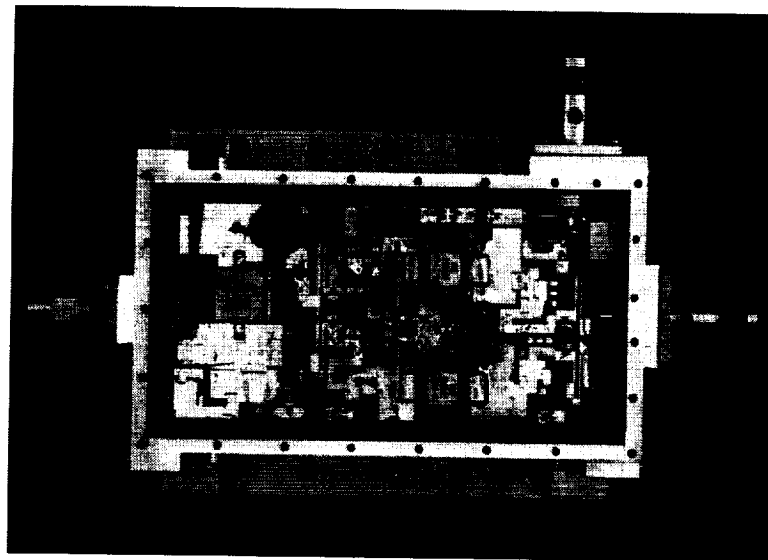
Figure 7.3-3. 200-W solid state power amplifier.

contributions of the remainder of the receiver. After filtering, the signal is downconverted to 70 MHz using a fixed LO. In addition to amplification and filtering, the 70-MHz IF also includes a digitally-controlled step attenuator whose primary purpose is to keep the receiver from saturating during calibration mode. This attenuator can also be used to fine tune the receiver gain for targets of different backscatter cross-section.

After the pulse round-trip time has elapsed, the DCG generates the deramp chirp. A PIN diode switch is used to cut off the input to the transmitter and the SSPA is disabled, assuring that there is no leakage from the transmitter into the receiver. The chirped LO generated by the DCG is mixed with 70-MHz IF signals in a pair of I-Q detectors, which simultaneously deramps the echo signal and converts it to baseband. After deramping, the maximum bandwidth of the received signal is less than 1 MHz. The signal is amplified and low-pass filtered to achieve the final system bandwidth, and then fed to a 12-bit analog-to-digital converter (ADC).

Gain Distribution

Gain distributions were optimized for two different cases that assumed an 8-bit and a 12-bit ADC. Table 7.3-1 shows the gain distribution and cascaded system performance parameters for the baseline design with a 12-bit ADC. This analysis assumes the ADC yields 10.5 effective bits performance and that the noise voltage is uniformly distributed over quantization bins so that ADC noise power contribution is given by:

$$P_n = \frac{\Delta^2}{12Z}$$

where Δ is the ADC quantization step size and Z is the input impedance of the ADC.

Table 7.3-1. Receiver Gain Distribution

ADC Specifications				End-to-End Performance including ADC								
eff.bits	trans.width	noise (dBm)	noise (dBm)	Gain (dB)	NF (dB)	IP3 (dBm)	OIP3 (dBm)	PiMdist (dBm)	Pisat (dBm)	NBW (kHz)	PiN (dBm)	DR (dB)
10.5	1.00	10.00	-54.98	64.60	3.53	-32.17	32.43	-42.17		22.43	1.00	-45.87	68.30

Component Specifications					Cascaded System Performance								
Component	Gain (dB)	NF (dB)	IP3 (dBm)	NBW (kHz)	NBW (kHz)	Gain (dB)	NF (dB)	IP3 (dBm)	OIP3 (dBm)	PiMdist (dBm)	Pisat (dBm)	NBW (kHz)	PiN (dBm)	DR (dB)
sw1	-0.50	0.50	65.00		250.00	-0.50	0.50	65.00	64.50			250.00	-90.02	
circ1	-0.20	0.20			250.00	-0.70	0.70	65.00	64.30			250.00	-90.02	
sw2	-1.50	1.50	25.00		250.00	-2.20	2.20	25.70	23.50	15.70	13.50	250.00	-90.02	
amp1	30.00	0.35		-25.00	250.00	27.80	2.55	-12.80	15.00	-22.80	5.00	250.00	-59.67	64.67
flt1	-3.20	3.20			15.00	20.80	2.57	-18.99	1.81	-28.99	-8.19	15.00	-78.87	70.68
mlx1	-7.00	7.00		0.00	1000.00	17.60	2.59	-18.99	-1.39	-28.99	-11.39	15.00	-82.05	70.66
att1	-4.00	4.00		10.00	500.00	13.60	2.65	-19.02	-5.42	-29.02	-15.42	15.00	-85.99	70.56
amp2	20.00	6.00		-15.00	500.00	33.60	2.95	-21.83	11.77	-31.83	1.77	15.00	-65.69	67.46
flt2	-6.00	6.00			4.00	27.60	2.95	-21.83	5.77	-31.83	-4.23	4.00	-77.43	73.20
amp3	20.00	6.00		0.00	8.00	47.60	2.96	-23.22	24.38	-33.22	14.38	4.00	-57.42	71.80
iq1	-7.00	7.00		13.00	8.00	40.60	2.96	-26.97	13.63	-36.97	3.63	4.00	-64.42	68.04
amp4	25.00	8.00		0.00	8.00	65.60	2.96	-32.17	33.43	-42.17	23.43	4.00	-39.42	62.85
flt3	-1.00	1.00			1.00	64.60	2.96	-32.17	32.43	-42.17	22.43	1.00	-46.44	68.87

To achieve maximum sensitivity, the receiver must provide enough gain to amplify the input noise level to somewhat higher than the ADC noise power. However, if too much gain is included, especially early in the signal chain, the dynamic range of the system suffers. An ideal gain distribution will yield a system noise figure that is not much higher than that of the LNA plus front-end losses and a dynamic range that is only slightly less than that of the ADC. The example distribution favors noise figure but this could easily be adjusted to sacrifice a small amount of sensitivity in order to increase the instantaneous dynamic range.

A design with an 8-bit ADC was also developed. Analysis showed that the 8-bit receiver design requires 20 dB more receiver gain and yields 20 dB less dynamic range than the 12-bit design. Since 12-bit, 1-MHz ADCs are readily available, implementing 12-bit resolution would not

present a technological challenge. The data processor input data rate will increase by a factor of 1.5 over the 8-bit case, but the processor could reduce the final output to either 8-bit linear or logarithmic data in order to keep the downlink data rate the same as the 8-bit design.

Calibration

In order to maintain accurate system calibration, the gain drifts in both the transmitter and receiver must be tracked. This is accomplished by coupling a small part of the transmitted signal through a calibrated attenuator into the receiver, thus measuring the product of the receiver and transmitter gain. Care must be taken to suppress all other signal paths between the transmitter and the receiver so that all power reaching the receiver during the transmit interval passes through the calibrated attenuator.

In the worst case, a leakage signal could arrive 180 degrees out of phase with the calibration signal and coherently subtract. Assuming that half of the 0.1-dB error budget is allocated to this type of error, all leakage signals must be suppressed by over 44 dB. If the calibration power into the receiver is set at a level that is 6 dB below the 1-dB compression point of the receiver, then transmit/receive (T/R) isolation of 125 dB is required.

While it is not impossible to achieve such high isolation, it can be difficult. Fortunately, at operating frequencies as low as 1.25 GHz, it is possible to take a less pessimistic approach. Because the wavelength is relatively long, the leakage path will tend to be phase stable. Hence, the disturbance caused by the leakage can be removed by calibration or by phase trimming. Still, the leakage should be suppressed by at least 20 dB so that this correction is small. This requires a T/R isolation of around 100 dB which can be supplied by the circulator and PIN diode switch if careful attention is paid to circuit layout and shielding.

System Timing

Figure 7.3-4 shows an approximate radar timing diagram for one pulse repetition interval. At the beginning of the transmit interval, the T/R line is raised, configuring the DCG for the transmit chirp and setting the calibration/antenna switch to calibration mode. Simultaneously, the transmit polarization and antenna-fed selection switches are set and the proper attenuation for transmit mode is loaded into the receiver attenuators.

After waiting the appropriate settling time for the above controls (approximately 1 μs), the SSPA and drive switch are enabled. After the SSPA bias stabilizes, a trigger signal is sent to the DCG, causing it to generate a 1 ms chirp. After the end of the chirp, the drive enable and SSPA bias are cut off and the attenuators and the antenna/calibration switches are configured for receive mode. The T/R line drops, configuring the DCG for LO generation. After about 5 ms (the pulse time-of-flight), another trigger is sent to DCG causing it to generate the chirped LO signal.

This sequence will then repeat, except for the values of the polarization and antenna feed select switches which may change from pulse to pulse. Thus, the control and timing unit should be capable of storing a sequence of these values large enough to conduct all required measurements over one complete scan.
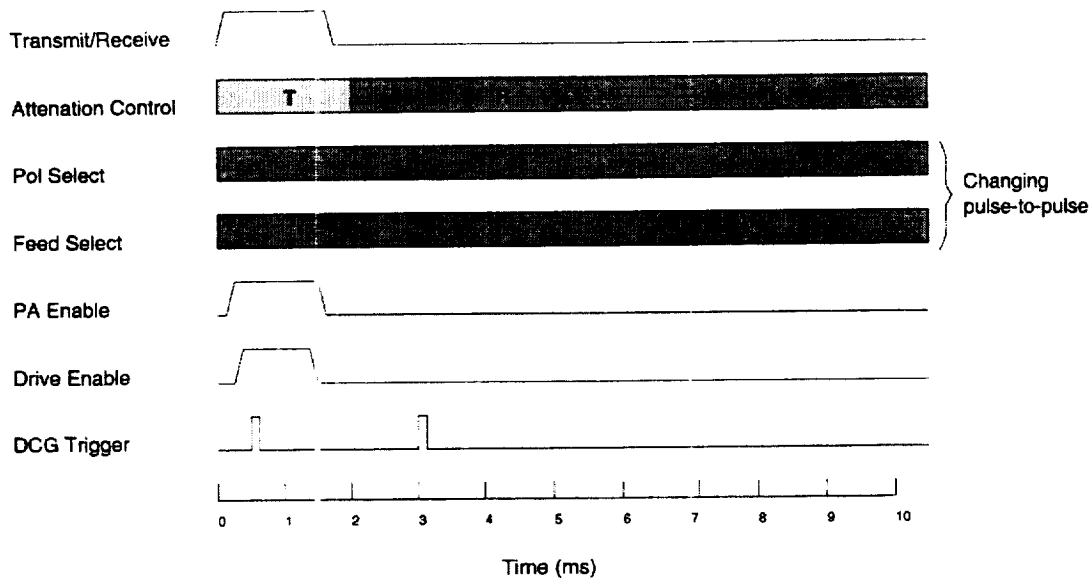
Figure 7.3-4. Radar system timing.

Power Consumption

In order to analyze the power, volume and mass requirements, preliminary component selections were made. At these frequencies, a wide range of components are available, so there is still a great degree of freedom available to substitute other components for the examples chosen below. Wherever possible, components with a proven space heritage were chosen. In cases where no flight-proven parts are readily available, parts utilizing appropriate technologies from vendors experienced in the production of space-qualified parts were chosen.

Table 7.3-2 shows the preliminary component list and the associated required voltages and power consumption. The entire RFES consumes less than 66 W, not including the loss due to power converters and conditioners. The transmitter consumes 27 W, assuming a 45% efficiency. Aside from the SSPA, the components were not selected specifically for low-power operation, so some further reduction in power consumption may be achievable. Current research into class-E amplifiers promises transmitter efficiencies of 70% or greater. The availability of this technology would substantially reduce transmitter power consumption.

Compact, space-qualified DC-DC converters are available from several vendors such as Vicor and Magnitude-3. These units would be used to supply 15 and –28 volts while the other, lower current voltages would be generated by fixed linear regulators. The DC-DC converters have efficiencies of greater than 80%, which yield a total consumption of 81 W from the spacecraft power bus.

Physical Layout

To analyze the mass and volume requirements, a preliminary circuit layout was designed. A 6U VME form factor was chosen because it allows for convenient integration with other system components using a variant of the space-qualified VME chassis developed for SeaWinds. However, the layout is sufficiently generic that it could serve in other configurations that do not utilize a VME chassis.

91

Table 7.3-2. Radar Parts List

Part designator	Description	Manufacturer	Man. Part #	Qty.	V (ea.)	mA (ea)	W (ea)	W (total)
2w1	2-way power divider (SM, 70 MHz)				0		0.00	0.00
3w1	3-way power divider (coaxial, 1250 MHz)	KDI	D364MS	1	0		0.00	0.00
3w2	3-way power divider (SM, 1180 MHz)	Synergy		1	0		0.00	0.00
4w1	4-way power divider (SM, 10 MHz+B12)	Synergy	SDL140	1	0		0.00	0.00
amp1	1.25 GHz LNA, 0.35 dB NF	Miteq	AFSM2-01200140-04-10P	2	15	90	1.35	2.70
amp2	1.25 GHz driver, 23 dBm P1dB	Miteq	AFSM2-01200140-40-23P	1	15	200	3.00	3.00
amp3	1180 MHz, +7 dB gain, +7 dBm P1dB	Watkins-Johnson	SMA39	1	15	90	1.35	1.35
amp4	70 MHz 20 dB gain, +20 dBm P1dB	Watkins-Johnson	SMA82	5	15	50	0.75	3.75
amp5	Video amp	Analog Devices	AD524	4	15	20	0.30	1.20
				4	-15	20	0.30	1.20
att1	fixed attenuator	Narda	Series 4779	4	0		0.00	0.00
att2	digital attenuator	M/A-Com	AT-263	4	5	5	0.03	0.10
				4	-6	1	0.01	0.02
att3	fixed attenuator (surface mount)	KDI	PCA series	8	0		0.00	0.00
circ1	T/R circulator, 0.15 dB loss 30 dB iso.	EMS, M/A-com		2	0		0.00	0.00
coup1	20 dB coupler (coax, 1250 MHz)	Narda	4012C-20	1	0		0.00	0.00
coup2	10 dB coupler (SM, 70-200 MHz)	Trak	CP/10AF-01	5	0		0.00	0.00
dcg	Digital Chirp Generator	JPL	special	1			8.00	8.00
flt1	1250 MHz bandpass 15 MHz BW	K&L	3DR35-1250/T15-1.6	3	0		0.00	0.00
flt2	70 MHz bandpass 5 MHz BW	K&L	3SMT-70/T5-P	3	0		0.00	0.00
flt3	1180 MHz bandpass MHz 15 BW	K&L	3DR35-1180/T15-1.6	1	0		0.00	0.00
flt4	10 MHz bandpass 1 MHz BW	K&L	3SMT-10/T1-P	1	0		0.00	0.00
flt5	1 MHz lowpass	K&L	3LSMT-1/T1.5-P	4	0		0.00	0.00
iq1	I&Q demodulators 70 MHz, 1 deg. Phase	Merrimac	IQP-20R	2	0		0.00	0.00
mix1	Mixer, 10-1500 MHz RF, +7 dBm LO	Watkins-Johnson	SM4A	3	0		0.00	0.00
osc1	1180 MHz PLCRO	CTI	PCMP series	1	15	80	1.20	1.20
				1	5	40	0.20	0.20
osc2	200 MHz PLXO	CTI	PXS series	1	15	250	3.75	3.75
osc3	10 MHz OCXO	Vectron	CO-718SD50-L2	1	15		2.00	2.00
sspa	120 W power amp	Remec, EMS, others	special	1	28		27.00	27.00
sw1	120 W SPDT PIN switch, low-loss	Hill Engineering	M22-0	3	5	300	1.50	4.50
				3	-28	40	1.12	3.36
sw2	SPDT 80 dB iso.	KDI	XN-33-HA	3	5	70	0.35	1.05
				3	-5	70	0.35	1.05
							Total:	65.43

The RFES is composed of two 6U-sized VME modules that are 232 mm square, including the VME bus connectors which may or may not be used. Each module may be milled from a solid billet of aluminum, creating separate chambers for the subcircuits. Each chamber has an individual cover in addition to the single piece cover over the entire module. This construction technique provides excellent isolation between the various subcircuits. The subcircuits are then interconnected with coaxial feedthroughs that pass through the chamber walls or coaxial connections via SMA connectors on the front and rear of the modules. These ports also provide a place to connect diagnostic equipment during testing.

The first module, pictured in Figure 7.3-5, is 20-mm thick and occupies a single VME slot. This module contains all of the front-end components including the circulators, antenna and polarization switches, calibration loops and SSPA. The main design criteria for this module was high isolation between the transmitter and the receiver. The coaxial components used in this module are bulkier and heavier than the microstrip components that are used in the other modules but they offer much greater isolation. The front panel has four coaxial connections to the antenna feeds and one to the transmitter driver in the RF/LO module. The rear panel has connections from the transmit sampler to the calibration attenuators and to the receiver inputs. The front and rear connectors can also be used to measure front-end losses, transmit power, and calibration loop loss.

The second module, shown in Figure 7.3-6, is 40-mm thick and occupies two slots in the VME chassis. This module, which contains the receiver, transmit chain, and all of the local oscillators including the chirp generator, has subcircuit chambers milled into both sides. One side contains both receiver channels, the transmit chain and the DCG while the other side contains power
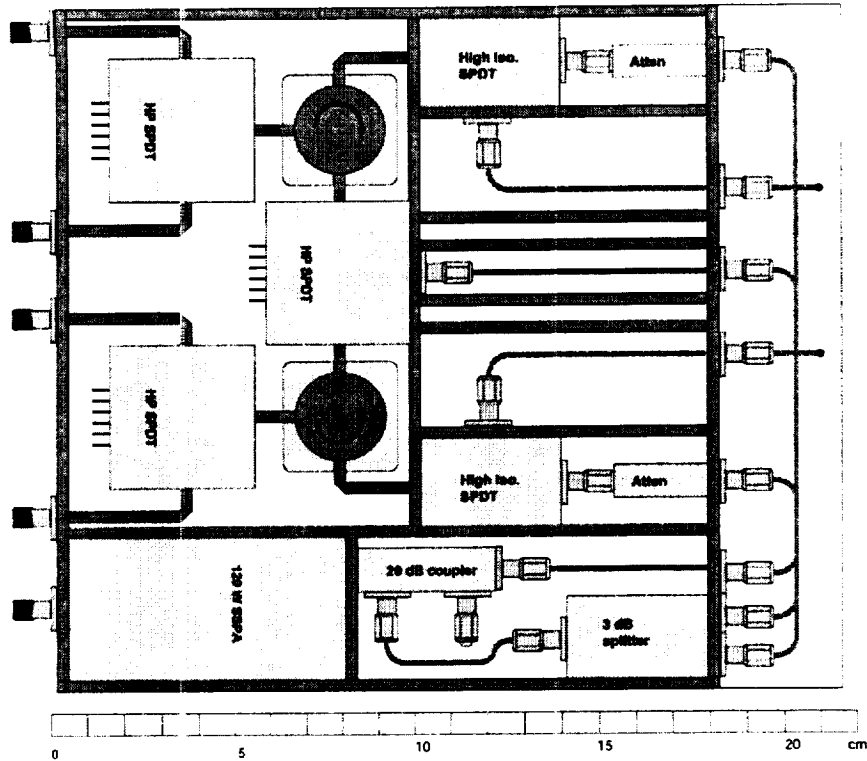
Figure 7.3-5. Front end module layout.

conversion and conditioning units and oscillators. The ovenized 10-MHz master oscillator requires the full thickness of both sides.

The receiver and transmitter chains use miniature surface-mounted microstrip components. Each part is encased in either a metal or ceramic package that is epoxy mounted to the substrate and soldered directly to a minimal length of 50 Ω microstrip line. Since microstrip lines have a tendency to radiate or couple to each other, separate shielded chambers are provided where isolation between subcircuits is required. The subcircuit chambers are connected with coaxial feedthroughs both within one side of the module and between the two sides. This technique allows distribution of the local oscillators without crossing microstrip lines. Diagnostic couplers routed to front and rear panel SMA connectors facilitate testing and characterization of the subcircuits.

The major contributor to the mass of this assembly is the aluminum structure. Assuming that the divisions between chambers are 3.2-mm thick and all the covers are 1.6-mm thick, the mass of the aluminum structure is approximately 1.75 kg. The mass allowances are given in Table 7.3-3.

93
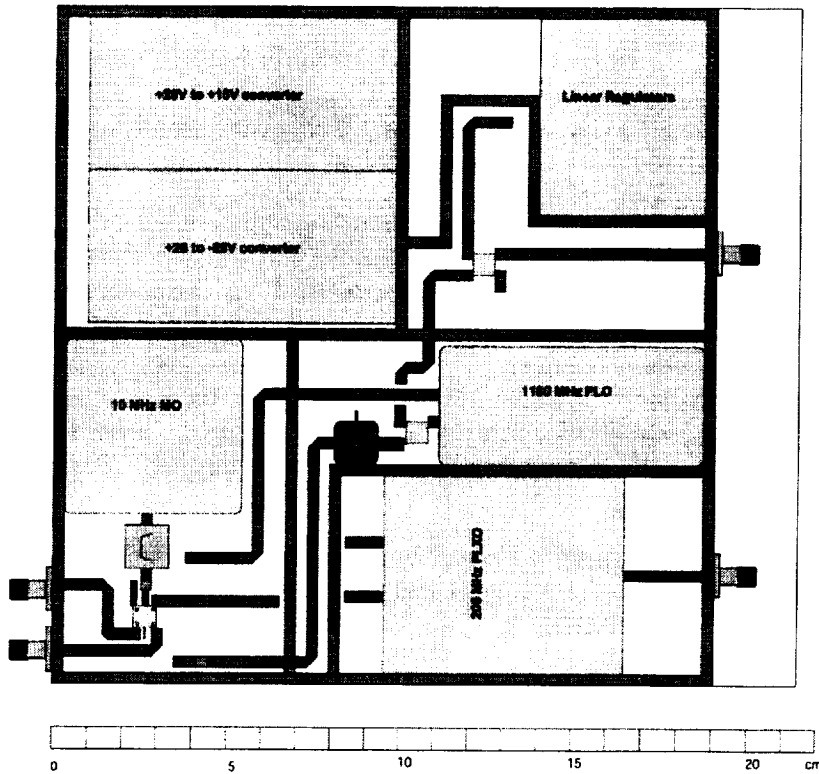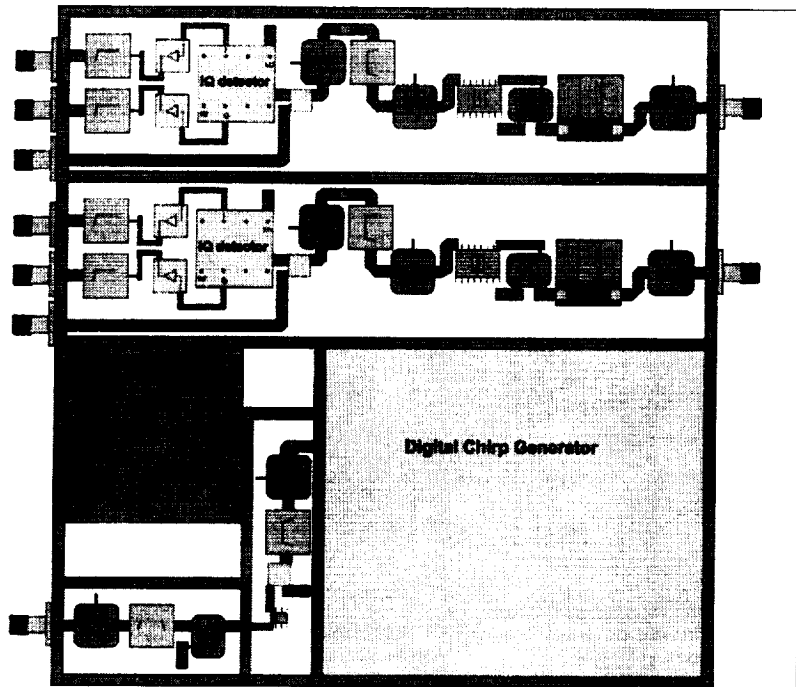
Figure 7.3-6. RF/LO module layout.

94

Table 7.3-3. RFES Mass Allowances

	Mass (kg)
Al Milled structure	1.00
Al covers	0.75
Coaxial components	0.50
Microstrip components	0.50
Cables and connectors	1.00
Total	4.25

7.3.2 Digital Subsystem Design

The design goal for the digital subsystem of the OSIRIS concept is to reduce programmatic risk and cost by using previously-proven flight hardware and designs whenever possible. The inherited JPL flight hardware information is based on JPL Team-X files.

The digital subsystem requirements are to (1) provide physical enclosures for the digital and RFES subsystems with regulated DC power to the digital subsystem electronics, (2) provide filtered spacecraft voltages to the RFES subsystem, (3) provide a spacecraft interface to the OSIRIS radar, including command, control and timing, (4) convert four video channels to four 12-bit digital channels, and reduce the digital data, and (5) output the results to the spacecraft for downlink. In addition, the digital subsystem provides the software and documentation necessary for flight operations and control of the radar to the spacecraft host. The digital subsystem is also required to establish and document the physical and electrical interfaces between the radar electronics and the spacecraft, including radar subassembly interconnection cabling.

Digital Design Overview

As shown in Figure 7.3-7, the digital subsystem consists of two subassemblies; one located on the rotating canister with the antenna and RFES subsystems (upper unit) and the other with the spacecraft electronics on the stationary section of the platform (lower unit). Each subassembly consists of a 6U VME chassis, digital and RFES modules, EMI power filters, and DC/DC converters. The chassis heaters are assumed to be provided and controlled by the spacecraft bus host. All radar electronics boards (upper unit) conform to the standard 6U VME footprint, but may not provide a VME interface. It is assumed that all the digital boards use conductive cooling methods and that no heat load will be dumped to the spacecraft frame. The heat load is dumped to space by means of conventional spacecraft radiators and louvers. The lower unit consists of a 1553 interface, power converter, and processor boards that are shared with another instrument. Otherwise, the spacecraft processor could communicate directly with the upper unit radar electronics by means of the 1553 interface. The upper unit consists of a single module to provide a four-channel ADC and data processor with both control and timing functions and interface to the payload interface unit (PIU) and the RFES subsystem (2–3 slots).

1553 and Processor Boards

These boards are already in production at JPL and have been successfully flown on previous space missions, both Earth-bound and interplanetary. The boards and their non-flight counterparts will be procured and used in support and checkout of the digital subsystem. In addition, the software development will use the boards in the ground support test equipment

95

Radar Electronics

The power converter board will use Mag-3 DC/DC power converters.

Power Converters

Antenna Array

RFES

Radar electronics enclosure will be VME based and inherit either a WindSat or a modified SeaWinds chassis design.

ADC w/data processing

The ADC unit is composed of four 8-bit CMOS ADC. The ADC design will be inherited from the Cassini program. The raw data processing will be done in hardware using a FPGA.

Control and Timing Unit

The control and timing unit will be FPGA based, using a RS-422 command and data communication link to the Radar processor located on the stationary deck.

Rotating Canister

Stationary Deck

S/C slip ring interface

Payload Interface Unit

The payload interface electronics enclosure will be VME based and inherit either a WindSat or a modified SeaWinds chassis design.

Payload Processor

The payload processor will be inherited from previous JPL flight programs.

EEPROM

The EEPROM board will be inherited from previous JPL flight programs.

Power Converters

The power converter board will use Mag-3 DC/DC power converters.

1553 I/F

The 1553 Interface board will be inherited from previous JPL flight programs.

The processed radar data will be collected and stored by the PIU processor. The data will be given to the S/C processor for downlink.

1553 I/F

S/C Processor

Spacecraft Bus

GPS antenna

Down link antenna

Spacecraft power management unit

spacecraft interfaces

spacecraft telemetry

Telemetry

Power Converters

Figure 7.3-7. Digital subsystem.

configuration to develop the code for the spacecraft interface and command and control of the radar. The control and timing field programmable gate array (FPGA) in the upper unit collects and formats all telemetry data and acts upon the commands and control instructions provided from the payload processor located on the lower unit. It is assumed that the spacecraft processor will have monitor and control responsibilities over the heater operations on both upper and lower radar chassis of the spacecraft.

Control and Timing (C&T) FPGA

The control and timing FPGA is required to take a system clock provided by the RFES subsystem and convert that clock into synchronous timing signals for use by both the digital and RFES subsystems. The C&T is a new design effort. The C&T FPGA serves as a data reference clock, counting at a 32-Hz rate and providing that clock count value to the data compression board. The counter value is encoded into the output data along with the range line header and sync word. The 32-Hz-based 16-bit counter is reset by command at the equatorial crossing per orbit. The C&T is controlled by a series of serial registers, written to by the processor. These registers provide the C&T board with timing and RFES attenuation values, which are used in the generation of all the radar timing signals. The C&T can provide command register feedback within the radar range line header to ensure that the proper command was received and to identify the radar operational parameters used in the range line collection.

Analog-to-Digital Converter (ADC) Array

This module consists of four CMOS 12-bit ADC units with the necessary input signal conditioning (DC block and impedance matching). The ADC array board provides additional power filtering and regulation as required to perform the necessary video-to-digital conversion. There is more than one radiation-hardened 12-bit ADC on the market currently that can meet the OSIRIS program requirements; the one chosen for this design was used by the Cassini program. The design will be inherited from the Cassini program to reduce risk, schedule, power, mass, and cost. The array will perform the analog telemetry function for the upper radar electronics during the period in which raw radar data are not being collected.

Raw Data Processor (FPGA)

The real time raw data processor is a new design. The 12-bit digital data from the each ADC are processed by the digital hardware. This is accomplished by using a radiation-tolerant/hardened FPGA configured as four arithmetic logic units (ALUs) operating in a parallel pipeline fashion. At an 18-MHz clock rate, each data sample is processed within 18 clock cycles, at the end of 100 samples producing four 16-bit output words for downlink via the C&T and payload processor interface. The estimated gate count to implement the design is 3,000 gates. The Actel 1280RH FPGA and other FPGA manufacturers exceed these requirements. The assumed radiation exposure for the mission life of 2 years is 6 to 9 KRads behind 100 mils of aluminum. The raw data processor provides telemetry formatting during the periods when raw data are not being processed. The telemetry data will be passed to the C&T FPGA where it will be sent to the payload interface unit.

Mass and Power

The mass and power estimates are summarized in Table 7.3-4. The payload interface unit refers to the lower stationary section. Table 7.3-5 summarizes the combined mass and power estimates for the radar system.

97

Table 7.3-4. Digital Subsystem Mass and Power Summary

Flight hardware	Unit mass (Kg)	Unit power (W)	Flight quantity	Spare	Description
Payload Interface Unit					
EEPROM_256K	1	1.2	1	1	EEPROM module to hold flight software
RS/6000	0.9	12.6	1	1	RAD 6000 processor module
Serial I/O	0.9	2.4	1	1	Serial interface module
1553 I/O	0.9	3	1	1	1553 interface module
VME chassis	5	0	1	1	Flight chassis
VX works S/W	0	0	1	0	Operating system for processor
Power module	1.5	10	1	1	No information on actuals
					Assumes cables provided by spacecraft
Total	10.2	29.2			
Digital Hardware on Rotating Platform					
Flight chassis	5	0	1	1	VME chassis supports RFES and digital
ADC with C&T	1.5	8	1	1	All in one module
Power module	1.5	10	1	1	Est. only, no information on actuals
Flight cables	0.5	0	4	4	Cables provided by digital
Total	10	18			Does not include RFES

Table 7.3-5. Radar Mass and Power Summary Estimates

	Mass (kg)	Power (W)
RF Electronics	5	81
Radar Digital Processor and C&DH	10	18
Payload Interface Unit	10	30
Total	25	129

7.4 LABORATORY BREADBOARD AND TESTS

As part of the study task, a laboratory breadboard was built to test the radar design. The objectives were to demonstrate the calibration stability of the transmit power and receiver gain product and to acquire test data for the design, layout optimization, RF leakage, noise figure, polarization isolation, and phase stability. Additional funding was subsequently provided by a NASA RTOP, the JPL Scatterometer project office, and the JPL Director's Research and Discretionary Fund, to upgrade the laboratory radar breadboard to an aircraft polarimetric radar system for field tests in summer 2000. The objectives of the contributing projects were (1) to support the development of ocean salinity measurement technology, and (2) to demonstrate polarimetric wind scatterometer technology with the aim of extending/improving the SeaWinds swath performance and integrating the radar approach with the planned National Polar Orbiting Environmental Satellite System (NPOESS) passive microwave system.

Figure 7.4-1 shows components of the laboratory breadboard. The breadboard development and testing enabled the correction of a number of design flaws including adjustments of the calibration loop gain setting and radar front-end isolation.
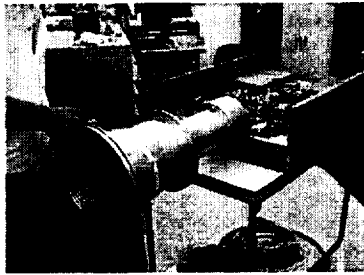
Ant+RF Front End
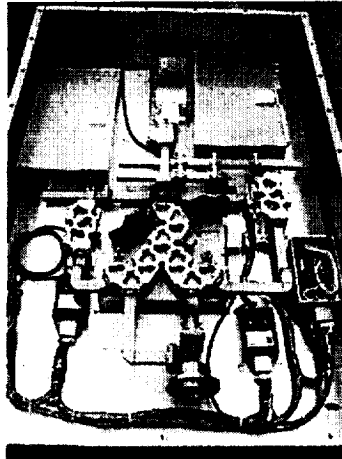
RF Front End
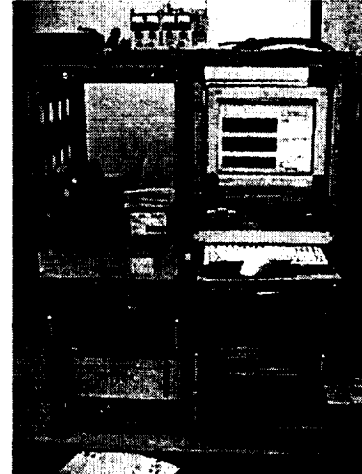
Rack
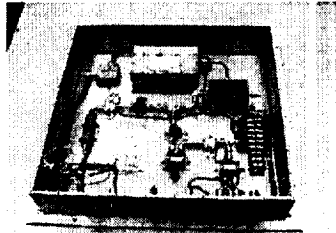
LO Box
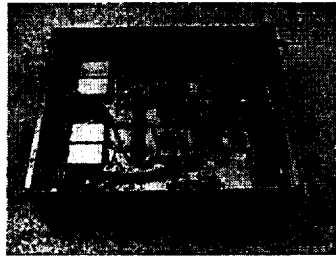
Radar Back End

Figure 7.4-1. Radar breadboard components.

Laboratory stability tests for gain and phase were conducted (Figures 7.4-2 and 7.4-3). These tests showed that the radar gain stability is better than 0.1 dB, and the relative phase change between horizontal and vertical polarization channels is less than 5 degrees, over several hours under ambient conditions. An outdoor calibration test was conducted prior to deployment of the instrument in flight tests. This was done to ensure correct echo detection in the range gate and to verify the stability of the calibration loop (Figure 7.4-4).

This system was deployed on the National Center for Atmospheric Research (NCAR) C-130 aircraft for a set of open water test flights over the Monterey Bay Aquarium Research Institute (MBARI) moorings in August 2000. The results demonstrated the gain and phase stability performance of the radar breadboard.

7.5 SUMMARY

A lightweight radar design, including RF electronics and digital subsystems, was completed. The key radar design parameters were derived from the science requirements, and the design performance has been verified against those requirements. A detailed RF electronics layout and parts selection was performed, and reliable estimates of mass and power were generated. A laboratory breadboard polarimetric radar for ocean wind and salinity sensing was built and tested using contributed funding. The breadboard system demonstrated the required gain and phase stability and performance of the radar-calibration loop.
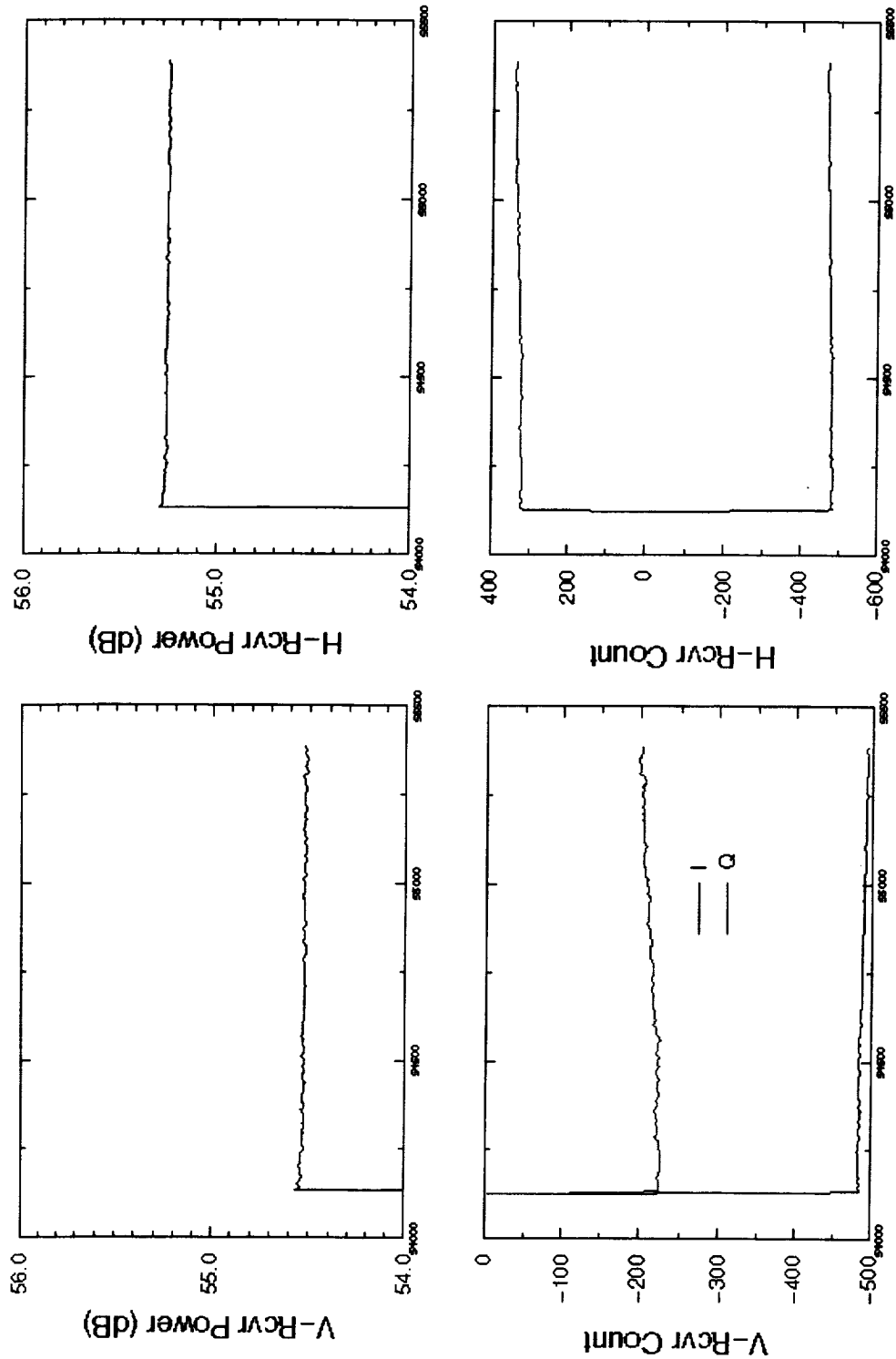
Figure 7.4-2 Laboratory gain stability test.
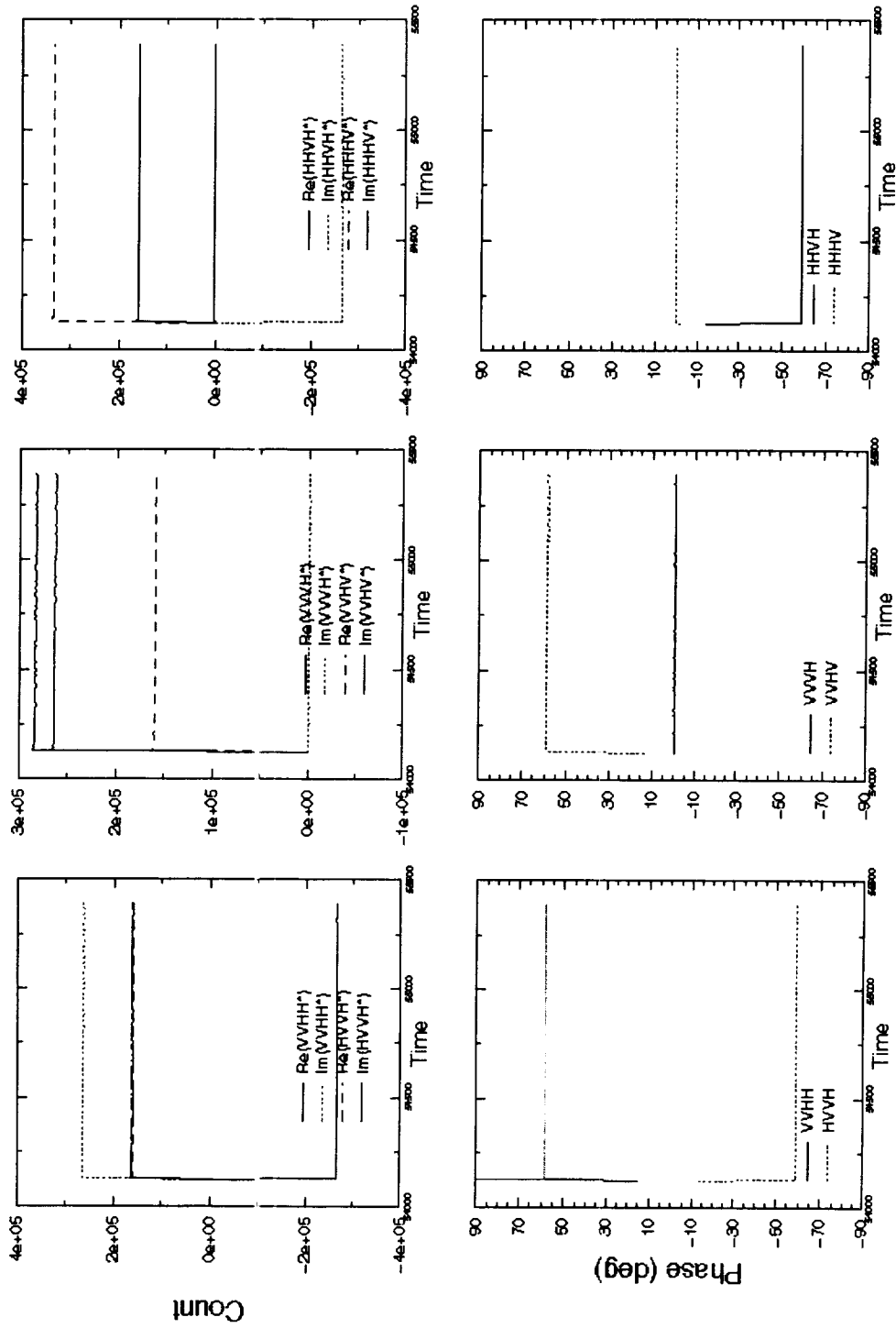
Figure 7.4-3 Laboratory phase stability test.
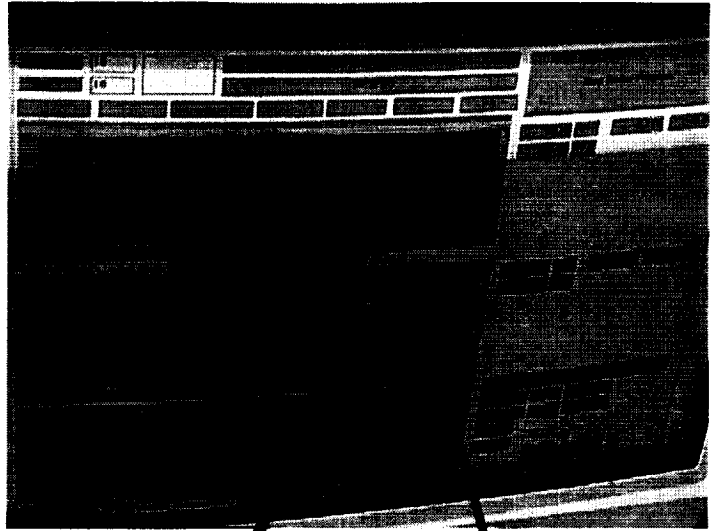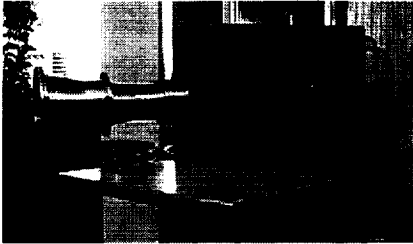
Radar Echo   Absorber on horn

Figure 7.4-4. Outdoor tests.

8. ANTENNA, SPACECRAFT AND LAUNCH VEHICLE CONFIGURATION

8.1 INTRODUCTION

The OSIRIS system configuration and design study included the objective of developing a low-cost, low-risk design for the spacecraft that would satisfy the control and pointing requirements imposed by the instrument while also meeting the mass, volume and cost constraints imposed by a limited mission budget. Meeting this objective would require a series of carefully considered design decisions regarding the choice of key system elements such as the deployable antenna, boom, spacecraft bus and launch vehicle, as well as the determination of a preferred overall system configuration. The OSIRIS design was intended to be suitable for ESSP and post-2002 EOS missions.

A two-phase technical approach was taken to implement this task. Science Applications International Corporation (SAIC) was contracted to assist in the first phase of this work, which consisted of a preliminary assessment of candidate antennas, spacecraft, launch vehicles and system configurations, and the development of recommended system options based on guidelines related to science/measurement compatibility, volumetric limitations and cost constraints. This first phase of work was reported in Section 4.

Recommendations arising from the first study phase led to selection of a preferred antenna and launch vehicle and two candidate spacecraft configurations based on off-the-shelf bus designs produced by two spacecraft/hardware manufacturers. The recommended antenna was a 6-meter diameter AstroMesh design, developed and produced by TRW Astro. The selected launch vehicle was a Taurus with a 92-inch fairing. The two spacecraft configurations included a rigid body spinner from TRW and a three-axis-stabilized bus from Spectrum Astro. Both spacecraft configurations were considered as candidates since, without further investigation, it was not possible to choose a preferred configuration.

Based on recommendations resulting from the OSIRIS Phase 1 effort, two parallel design approaches for the OSIRIS spacecraft were pursued in Phase 2. One design would focus on a rigid body spinner spacecraft, while the second design was based on a three-axis-stabilized spacecraft. Also, in accordance with the Phase 1 recommendations, the designs were to be based on low-cost, previously flown spacecraft from TRW and Spectrum Astro, respectively, and were to accommodate a 6-meter diameter AstroMesh antenna along with the other OSIRIS payload requirements. To carry out the design analyses needed to determine the performance and cost feasibility of both design options, JPL procured the services of the spacecraft vendors, TRW S&EG and Spectrum Astro, as well as the antenna manufacturer, TRW Astro. TRW Astro was directed to work with both vendors to provide them the structural data on the AstroMesh antenna and the interface information needed to incorporate the antenna system in their designs.

8.2 OBJECTIVES

The OSIRIS Phase 2 study objectives were spelled out explicitly in the statements of work prepared for both contractors. Some of the key elements of each contractor's SOW are summarized below.

8.2.1 TRW Objectives and Deliverables

There were two major tasks associated with the TRW Statement of Work. Task 1 called for TRW Astro to work directly with Spectrum Astro to develop a structural configuration design to interface the AstroMesh antenna with a Spectrum Astro Coriolis type spacecraft for the OSIRIS system. The objective for this structural configuration design was to maximize the structural stiffness of the mechanical system when the antenna is in the deployed configuration and at the same time minimize the size of the stowed antenna/spacecraft configuration. This deployable interface structure between the antenna and spacecraft is the key for enabling an efficient stowed "system package" while maintaining the appropriate stiffness support for the deployed reflector. System definition was to be provided with sufficient fidelity to analytically demonstrate satisfaction of these key requirements. Deliverables under Task 1 included: (1) antenna subsystem description; (2) stowed and deployed design configuration layout; and (3) top level performance summary; mass stiffness, and fundamental modes.

In Task 2, TRW Astro was to work directly with TRW S&EG to develop a spacecraft configuration, which integrated the AstroMesh antenna with the T-200 TRW spacecraft to satisfy the OSIRIS mission requirements. The objective for this configuration design was to fully satisfy the system control, structural stiffness, and stowage envelope requirements of the integrated and spinning AstroMesh T200 spacecraft concept. Again, the system was to be designed with sufficient fidelity to analytically demonstrate satisfaction of these key requirements. Deliverables under Task 2 included: (1) system description (including antenna subsystem description); (2) overall configuration trades, assessment and recommendations; (3) requirements vs. capabilities; (4) configuration drawings; (5) mass and power summary; (6) integrated control analysis assessment; and (7) integrated spacecraft and antenna structure/dynamic assessment.

8.2.2 Spectrum Astro Objectives and Deliverables

The statement of work provided to Spectrum Astro included six specific tasks, all related to investigating the feasibility of using a modified version of their Coriolis spacecraft equipped with a 6-meter AstroMesh antenna, to perform the OSIRIS mission. The objectives of each of the six tasks correlate directly with the contract deliverables and can be summarized as follows: (1) Identify the changes and modifications to the existing Coriolis spacecraft design that are specifically needed to accommodate the OSIRIS mission. (2) Using a structural Finite Element Model (FEM) of the AstroMesh antenna supplied by TRW Astro, provide a simplified Coriolis FEM that reflects the specific design configuration for the OSIRIS spacecraft bus. (3) Assess the attitude determination and control subsystem (ADCS) design trades, modifications, and impacts necessary to accommodate the attitude determination and control requirements of the OSIRIS payload. (4) Provide a full set of spacecraft system metrics including margins, where applicable, for mass, power, dimensions, pointing, knowledge, configuration, data rate, data storage, and radiation susceptibility. (5) Provide configuration-level drawings (i.e., Pro-E models) of the stowed and deployed OSIRIS spacecraft, including both bus and payload as well as the stowed configuration within the Taurus launch vehicle shroud.

8.3 CONTRACTOR REPORTS

Reports provided by the two OSIRIS contractors at the conclusion of their efforts contained all the deliverables identified above. Due to the proprietary nature of some of the report contents,

only those portions approved for release by TRW and Spectrum Astro have been included here (Appendices I and II). Based on these reports, the recommended configurations and designs were evaluated to assess the overall feasibility of the OSIRIS concept from a performance standpoint. While cost is also a major factor in determining the ultimate viability of the concept, the cost uncertainties that exist at the present time kept a discussion of costs outside the scope of the review.

8.3.1 Antenna Concept Development (TRW Astro)

TRW Astro worked with both Spectrum Astro and TRW S&EG to develop a concept and structural design to interface the 6-meter diameter AstroMesh reflector subsystem with both the Spectrum Astro Coriolis and TRW T-200 candidate spacecraft. Diagrams depicting the antenna in the stowed and deployed configurations for both spacecraft were provided. Stowed configurations for both spacecraft were shown to fit within the fairing constraints of the Taurus launch vehicle. In fact, the TRW configuration can fit within the 63-inch Taurus fairing.

An antenna subsystem mass statement was generated. Configuration structural designs were developed for the full complement of necessary structural and mechanical elements including the reflector, boom (struts, actuators, deployment drive, balance mass), and tie-downs. A structural analysis was done using the AstroMesh antenna finite element model to determine the dynamic characteristics of the deployed antenna, and the quasi-static deflection of the antenna/boom was determined. These analyses showed that the 6-meter AstroMesh antenna and support boom could be made sufficiently stiff and dynamically balanced to satisfy the OSIRIS mission requirements. Moreover, the successful first flight and deployment of the AstroMesh antenna on the Thuraya mission in November 2000, further strengthened the antenna recommendation of Phase 1. A careful team review of the antenna and spacecraft interface design did not identify any major issues requiring further study. The TRW Astro antenna report is provided in Appendix I (presentation made at the NASA Land Surface Hydrology Program Soil Moisture Mission Workshop, Las Vegas, NV, September 2000).

8.3.2 Rigid Body Spinner Spacecraft (TRW S&EG)

The rigid body spinner proposed by TRW for the OSIRIS mission is based on the TRW T-200 bus, and differs substantially from the rigid spinner configuration suggested in Phase 1. The antenna feedhorns are mounted on the side of the spacecraft rather than the top. This accommodates the launch loads, since the TRW launch configuration orients the spacecraft so that its spin axis is perpendicular to the launch axis. Several advantages are derived from this launch orientation and spacecraft configuration including simplified ACS accommodation, simplified deployments of antenna and solar array, and reduced volume requirements. Issues associated with this configuration include the need for an inertial product adjustment device to fine tune the spacecraft center of gravity on orbit, a root damper or higher frequency design of the solar panels to eliminate potential problems related to their rotation at rates near their natural frequency, and augmentation of the power subsystem to accommodate the payload requirements. Two minor issues resulting from the launch orientation were the mounting of the feedhorns slightly off the spin axis and a requirement for pulsed propulsion operation.

8.3.3 Three-Axis-Stabilized Spacecraft (Spectrum Astro)

The OSIRIS spacecraft configuration proposed by Spectrum Astro is based on a three-axis-stabilized bus used in the Coriolis program. Like OSIRIS, the Coriolis mission requires a rotating antenna (smaller, but with a much higher rotation rate) mounted to a spin table atop a nadir pointing, three-axis-stabilized spacecraft in Sun-synchronous orbit. Starting with the Coriolis spacecraft and the antenna design data and finite element model (FEM) provided by TRW Astro, Spectrum Astro produced a preliminary design for a spacecraft capable of performing the OSIRIS mission. Documentation of the Spectrum Astro effort was reported in a set of reports including: (1) a technical summary, identifying the needed changes and modifications to the Coriolis spacecraft and providing the required set of spacecraft metrics; (2) results of the FEM analyses; (3) an attitude control study addressing the ACS design and spacecraft control issues; and (4) a set of spacecraft configuration drawings.

The results of the Spectrum Astro study support the conclusion that the spacecraft design has substantial margins and, based on their previous experience with Coriolis, represents a feasible, low risk approach. Non-proprietary sections of the Spectrum Astro reports are provided in Appendix II.

9. REFERENCES

Balanis, C. A. (1997): *Antenna Theory: Analysis and Design*, John Wiley and Sons, New York.

Caldecott, R., C. A. Mentzer, and L. Peters, Jr. (1973): The corrugated horn as an antenna range standard, *IEEE Trans. Antenna and Propagation, 21*, 562-564.

Clarricoats, P. J. B. and A. D. Olver (1984): *Corrugated Horns for Microwave Antennas*, IEE Electromagnetic Waves Series, Vol. 18, Peter Peregrinus Ltd., London, UK.

Cravey, R. L., H.-J. C. Blume, C. P. Hearn, L. C. Schroeder, and R. F. Harrington, (1995): Electromagnetic losses in metallized thin films for inflatable radiometer applications, *AIAA Space Programs and Technologies Conference, AIAA 95-3741, Huntsville, Alabama, September 26-28, 1995.*

Duan, D. W. and Y. Rahmat-Samii (1995): A generalized diffraction synthesis technique for high performance reflector antennas, *IEEE Trans. Antennas and Propagation, 43*, 27-40.

Harrington, R. F. and H.-J. C. Blume (1984): Determination of electromagnetic properties of mesh material using advanced radiometer techniques, *Proceedings of the Large Space Antenna Technology Symposium, December 1984.*

Imbriale, W., V. Galindo-Israel, and Y. Rahmat-Samii (1991): On the reflectivity of complex mesh surfaces, *IEEE Trans. Antennas and Propagat., AP-39*, 1352-1365.

Jackson, T. J. (Ed.) (1999): NASA post-2002 land surface hydrology mission (EX-4), *Report of the NASA Post-2002 Land Surface Hydrology Planning Workshop, Irvine, CA, April 12-14, 1999*, (http://lshp.gsfc.nasa.gov/missdrft.html).

Lagerloef, G. S., C. T. Swift, and D. M. LeVine (1995): Sea surface salinity: The next remote sensing challenge, *Oceanography, 8*, 44-50.

Lagerloef, G. S. (Ed.) (1998): Preliminary assessment of the scientific and technical merits for salinity remote sensing from satellite, *Final report of the first workshop, Salinity Sea Ice Working Group (SSIWG), La Jolla, CA, 7-8 February 1998*, (http://www.esr.org), Earth and Space Research, Seattle, WA.

Lawrence, R. W. and T. G. Campbell (2000): Radiometric characterization of mesh reflector material for deployable real aperture remote sensing applications, *Proceedings of the 2000 IEEE Geoscience and Remote Sensing Symposium (IGARSS 2000)*, Honolulu, Hawaii, 24-28 July, 2000.

Love, A. W. (1976): *Electromagnetic Horn Antennas*, IEEE Press, New York.

Mentzer, C. A. and L. Peters, Jr. (1973): Properties of cutoff corrugated surfaces for corrugated horns, *IEEE Trans. Antenna and Propagation, 22*, 191-196.

Miller, B. (1998): Satellites free the mobile phone, *IEEE Spectrum, 35*, 26-35.

NASA (2000): *Exploring Our Home Planet: Earth Science Enterprise Strategic Plan*, National Aeronautics and Space Administration, Washington, D.C., November 2000.

Njoku, E. G. and D. Entekhabi (1996): Passive microwave remote sensing of soil moisture, *J. Hydrology, 184,* 101-129.

Njoku, E. G., Y. Rahmat-Samii, J. Sercel, W. Wilson, and M. Moghaddam (1999): Evaluation of an inflatable antenna concept for microwave sensing of soil moisture and ocean salinity, *IEEE Trans. Geosci. Rem. Sens., 37,* 63-78.

Njoku, E. G., W. J. Wilson, S. H. Yueh, and Y. Rahmat-Samii (2000a): A large-antenna microwave radiometer-scatterometer concept for ocean salinity and soil moisture sensing, *IEEE Trans. Geosci. Rem. Sens., 38,* 2645-2655.

Njoku, E. G., W. Wilson, S. Yueh, R. Freeland, R. Helms, K. Oxnevad, T. Campbell, W. Lawrence, Y. Rahmat-Samii, H. Feingold, G. Didinsky, and J. Rauwulf (2000b): Large deployable-mesh antenna system for ocean salinity and soil moisture sensing, *Proc. 2000 IEEE Aerospace Conference, March 18-25, 2000,* Big Sky, MT.

Njoku, E. G., Y. Kim, M. Spencer, W.-Y. Tsai, W. Wilson, S. Yueh, J. van Zyl, Y. Rahmat-Samii, and M. Thomson (2001): A spaceborne L-band radiometer-radar concept for land and ocean surface monitoring, *Proc. 2001 IEEE Aerospace Conference, March 10-17, 2001,* Big Sky, MT.

Olver, A. D., P. J. B. Clarricoats, A. A. Kishk, and L. Shafai (Eds.) (1994): *Microwave Horns and Feeds,* IEE Electromagnetic Waves Series, Vol. 39, IEEE, New York.

Rahmat-Samii, Y. (1985): Effects of deterministic surface distortions on reflector antenna performance, *Annales de Telecommunication, 40,* 350-360.

Rahmat-Samii, Y. and S. W. Lee (1985): Vector diffraction analysis of reflector antennas with mesh surfaces, *IEEE Trans. Antennas and Propagat., AP-33,* 76-90.

Rahmat-Samii, Y. (1993): Reflector antennas, in: *Antenna Handbook, Volume II, Chapter 15 (Y. T. Lo and S. W. Lee, Eds.),* Van Nostrand Reinhold, New York.

Rahmat-Samii, Y., R. A. Hoferer, and H. Mosallei (1998): Beam efficiency for reflector antennas: The simple formula, *IEEE Antennas and Propagation Magazine, 40,* 82-87.

Rahmat-Samii, Y. and E. Michielssen (1999): *Electromagnetic Optimization by Genetic Algorithms,* John Wiley and Sons, New York.

Ruze, J. (1966): Antenna tolerance theory, *Proc. IEEE, 54,* 633-640.

Schroeder, L. C., M. C. Bailey, R. F. Harrington, B. M. Kendall, and T. G. Campbell (1994): Design studies of large aperture, high-resolution Earth science microwave radiometers compatible with small launch vehicles, *NASA Tech. Rep. 3469,* NASA Langley Research Center, Hampton, VA.

Shen, B. and W. L. Stutzman (1995): Performance evaluation of high-gain radiometer antennas, *Radio Science, 30,* 1767-1776.

Simmons, A. J. and A. F. Kay (1966): The scalar feed: A high performance feed for large paraboloid reflectors, *IEE Conference Publication, 21,* 213-217.

Swift, C. T. (1980): Passive microwave remote sensing of the ocean – A review, *Boundary-Layer Meteorol., 18,* 25-54.

Wentz, F. J., P. Ashcroft, and C. Gentemann (2001): Post-launch calibration of the TRMM Microwave Imager, *IEEE Trans. Geosci. Rem. Sens. 39*, 415-422.

Wilson, W. J., E. G. Njoku, and S. H. Yueh (2000): Active/passive microwave system with deployable mesh antenna for spaceborne ocean salinity measurements, *Proceedings of the 2000 IEEE Geoscience and Remote Sensing Symposium (IGARSS 2000)*, Honolulu, Hawaii, 24–28 July, 2000.

Yueh, S. H. (2000): Estimates of Faraday rotation with passive microwave polarimetry for microwave remote sensing of Earth surfaces, *IEEE Trans. Geosci. Rem. Sens. 38*, 2434-2438.

Yueh, S. H., R. West, W. J. Wilson, F. K. Li, E. G. Njoku, and Y. Rahmat-Samii (2001): Error sources and feasibility for microwave remote sensing of ocean surface salinity, *IEEE Trans. Geosci. Rem. Sens. 39*, 1049-1060.

Zimmermann, M. L. (1991): Computation and optimization of beam efficiency for reflector antennas, *Electromagnetics, 11*, 235-254.

APPENDIX I.

IIP OSIRIS ANTENNA CONCEPT

(TRW Astro Aerospace)

TRW

TRW Astro Aerospace

IIP OSIRIS
Antenna Concept

Presented to
NASA Earth Science Enterprise
Soil Moisture Mission Workshop
PR-1059

September 13, 2000

AstroMech is a patented design of TRW Astro Aerospace (U.S. Patent No. 5,space,space.140)

The AstroMesh™ Reflector

TRW

- For space satellite antennas
  - Large, offset apertures
  - High accuracy and reflectivity for up to 40 GHz
  - High stiffness
  - Low weight
  - Reliable deployments
  - Low cost
  - Ease of manufacture and ground test
  - PIM free
  - Shaped surfaces
- U.S. Patent No. 5,680,145

AstroMesh is a patented design of TRW Astro Aerospace (U.S. Patent No. 5,680,145).

The AstroMesh™ Reflector, Continued

TRW

- Culmination of 30 years of lessons learned
  - Advantages of mesh reflectors
    - Mesh density starts at 0.02 kg/m^2
    - Efficient truss structures with filamentary shaping networks
    - High aerodynamic and solar transmissivity
  - Disadvantages of heritage ribbed designs
    - Mesh management
    - Highly redundant mesh shaping networks
    - Ribs
    - Explosive deployments or low kinematic authority
    - Ground test limitations
    - Passive Intermodulation (PIM)

AstroMesh is a patented design of TRW Astro Aerospace (U.S. Patent No. 5,680,145)

A-4

The AstroMesh™ Reflector, Continued

TRW

- Advantages of rings with shells
- Inflatables possess qualities of a statically determinate structure
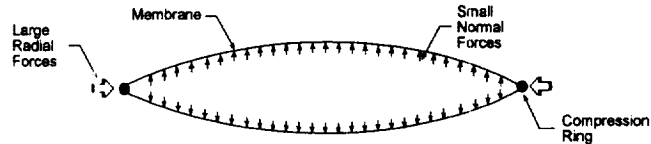
- Drawbacks associated with materials, inflation systems, solar and atmospheric transmissivity, compression ring

8711

Astromesh is a patented design of TRW Astro Aerospace (U.S. Patent No. 5,680,145).

The AstroMesh™ Reflector, Continued

TRW

- Goal was to emulate an inflatable structure with a mechanically deployable design
  - Available materials have longevity, are ≥20 times stiffer, have <1/200 the CTE
  - Diaphanous mesh, efficient ring truss and geodesic shell combination is lighter, stiffer, and more accurate
  - Statically determinate structure is possible

Astromesh is a patented design of TRW Astro Aerospace (U.S. Patent No. 5,680,145).

Reflector Structure

TRW

- Geodesic Trusses (nets) tensioned back-to-back across a deep deployable ring truss
- Gold-plated, molybdenum knitted mesh, tensioned behind net for flat, reflective facets
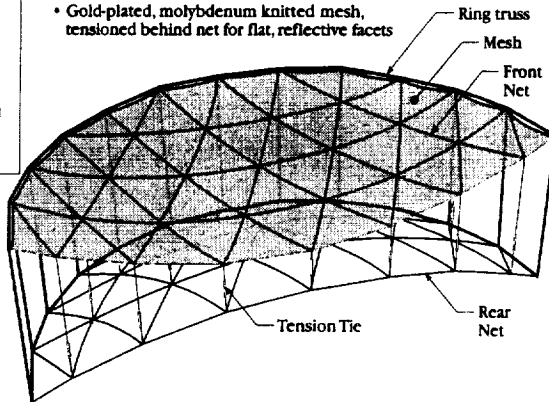
Ring truss

Mesh

Front Net

Tension Tie

Rear Net

AstroMesh is a patented design of TRW Astro Aerospace (U.S. Patent No. 5,680,145).

AstroMesh™ Nomenclature
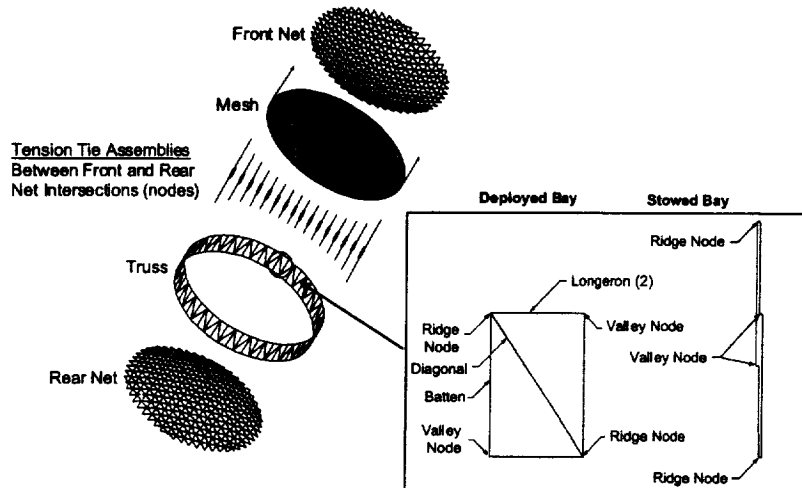
TRW

Front Net

Mesh

Tension Tie Assemblies Between Front and Rear Net Intersections (nodes)

Truss

Rear Net

Deployed Bay

Stowed Bay

Ridge Node

Longeron (2)

Valley Node

Ridge Node

Valley Node

Diagonal

Batten

Valley Node

Ridge Node

Ridge Node

AstroMesh is a patented design of TRW Astro Aerospace (U.S. Patent No. 5,680,145).

A-6

AstroMesh™ Reflector Development (1 of 3)

TRW
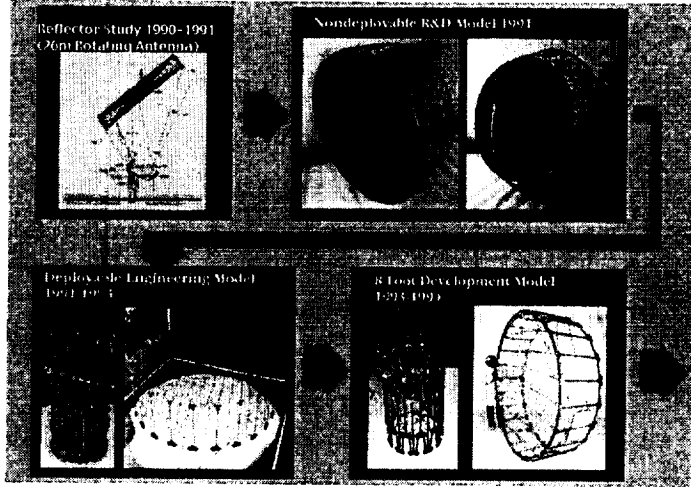
Astromesh is a patented design of TRW Astro Aerospace (U.S. Patent No. 5,680,145).

AstroMesh™ Reflector Development (2 of 3)
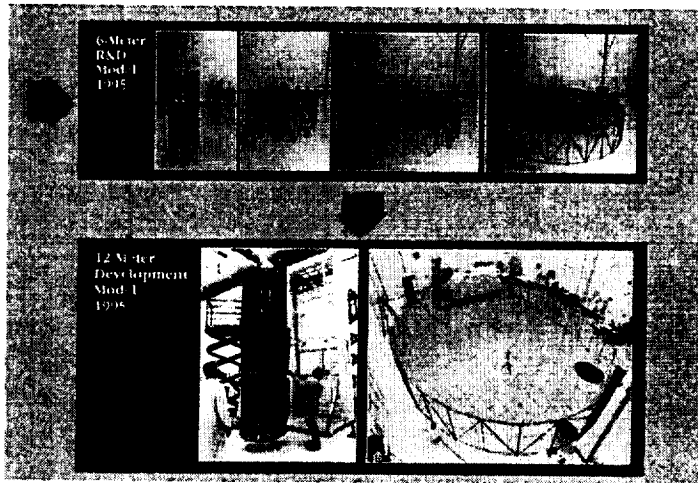
TRW

Astromesh is a patented design of TRW Astro Aerospace (U.S. Patent No. 5,680,145).

AstroMesh™ Reflector Development (3 of 3)
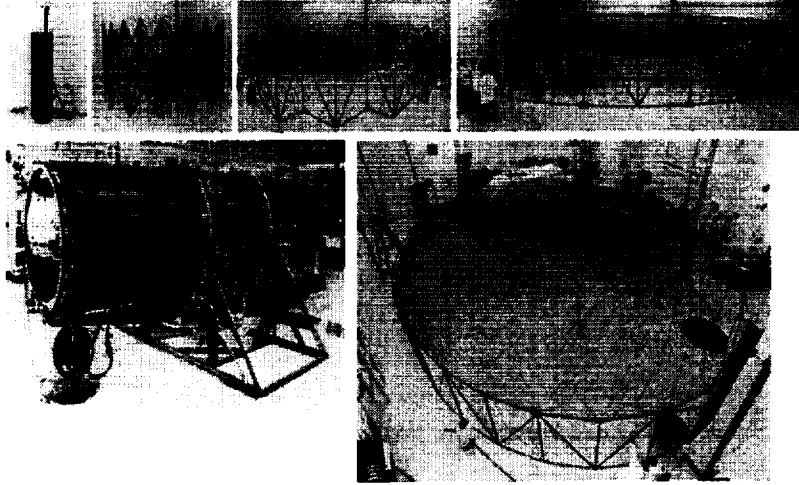
AstroMesh is a patented design of TRW Astro Aerospace (U.S. Patent No. 5,680,145).

AstroMesh™ Reflector Qualification   **TRW**

Test	6-Meter	12.25-Meter Flight
Deployments	55	36
Surface Accuracy		
Photogrammetry Cup Up	0.41 mm RMS	0.4 mm RMS
Photogrammetry Cup Down	<±0.07 mm ΔRMS	<±0.1 mm ΔRMS
Contour Repeatability	<0.07 mm ΔRMS	<0.07 mm ΔRMS
Moisture Susceptibility		<±0.1 mm ΔRMS
Thermal Cycling	-140°C to +135°C	-137°C to +93°C
Launch Sine and Acoustic Vibration	3 axis sweeps to 50-g peak response	Sea Launch Ariane 5
PIM 5th and 7th Order, two tone	-165 dBm maximum; thermal extremes and vibration	7th Order Testing < -150 dBm
Deployment with Spacecraft ACS Loads	Qualitative	Qualitative
Deployed Frequency	2.0 Hz cantilever; fixed boom	> 0.53 Hz; fixed boom
Single-Point Failure Modes	Yes	Yes
Transportation	Yes	Yes
1 g Offloader Sensitivity, Maximum Accel 0.1 g	Qualitative	Qualitative
ESD Electrical Testing Including Grounding	Some materials and components	Stowed and Deployed Ground Paths Verified

AstroMesh is a patented design of TRW Astro Aerospace (U.S. Patent No. 5,680,145)

AstroMesh™ Reflector Qualification, Continued   **TRW**

Test	6-Meter	12.25-Meter Flight
Boom Thermal Distortion with 278°C Gradient	<0.07-mm ΔRMS	< 0.03° Antenna Beam Pointing Error relative to boresight axis
Thermal Life Cycling 1600 Cycles; -139°C to +96°C and -190°C to +150°C		Life Cycle testing on Bonded Assemblies, Nonstandard Bonds
Thermal Life Deployment Cycling -139°C to +96°C and -190°C to +150°C		Life Cycle testing on Bonded Assemblies, Material Samples
Thermal Cycling and Release at Temperature Testing of Secondary Vectran Restraint Cycling: -137°C to +110°C Release: -56°C, +102°C		Successful Releases at temperature extremes.
Secondary Vectran Restraint, Long Term Creep during Ambient Storage		Storable > 5 yrs
Secondary Vectran Restraint, Creep at Temperature -137°C to +110°C		Minimum required tension maintained at completion of thermal cycling.
Deployment Cable Pulley Friction at Load and Temperature Boom Tip Pulley (lubed and not lubed): -70°C to +100°C Diagonal Pulley: -100°C to +100°C		No significant increase in friction over temperature range.

AstroMesh is a patented design of TRW Astro Aerospace (U.S. Patent No. 5,680,145).

Deployment and Mesh Management **TRW**

- Robust reflector deployment and mesh management characteristics
  - Over 250 successful ground deployments, 60 with flight units
  - Deployment cable has high mechanical advantage over deployment kinematics
  - All joints have free-running fits at all thermal extremes
  - All joints preloaded when deployed
  - Mesh fully contained when stowed
  - Mesh and nets deploy independently of truss

AstroMesh is a patented design of TRW Astro Aerospace (U.S. Patent No. 5,680,145).

2.5-Meter AstroMesh™ Engineering Model RF Measurements **TRW**
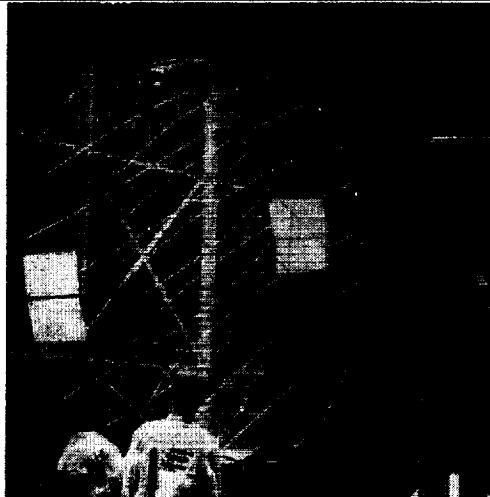
- Antenna patterns as predicted
  - Tested at 1.6 GHz through 11.0 GHz
- Over 140 deployments

AstroMesh is a patented design of TRW Astro Aerospace (U.S. Patent No. 5,680,145).

AstroMesh Flight Programs

TRW

Thuraya
- 12.25 m
- Completed; 5 units delivered
- Launch October 2000

INMARSAT 4
- 9.0 m
- ATP September 2000
- Launch 2003

AstroMesh is a patented design of TRW Astro Aerospace (U.S. Patent No. 5,680,145).

Thuraya

TRW

7510-145-000

AstroMesh is a patented design of TRW Astro Aerospace (U.S. Patent No. 5,680,145).

INMARSAT 4

TRW

7510-385D-001

AstroMesh is a patented design of TRW Astro Aerospace (U.S. Patent No. 5,680,145).

TRW

**IIP OSIRIS
Antenna Concept**

Astro Mesh is a patented design of TRW Astro Aerospace (U.S. Patent No. 5,680,145).

Project Goals

TRW

- TRW Astro (Astro) is working with Spectrum Astro and TRW S&EG to develop a structural design that interfaces an AstroMesh reflector antenna subsystem with two candidate spacecraft:

  - Simple spinner; TRW S&EG

  - Three-axis stabilized; Spectrum Astro (Coriolis)

- The objective is to maximize the structural stiffness and balance of the antenna while minimizing the size of the antenna/spacecraft configurations. The system shall have enough fidelity to analytically demonstrate satisfaction of key OSIRIS requirements

Astro Mesh is a patented design of TRW Astro Aerospace (U.S. Patent No. 5,680,145).

TRW Astro Aerospace, PR-1059

OSIRIS Antenna Subsystem
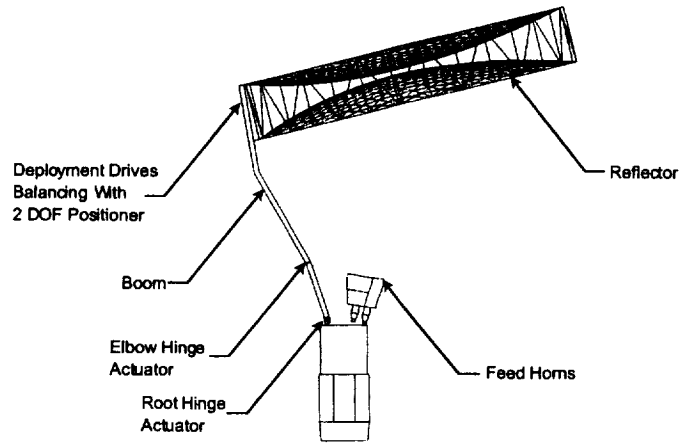
Deployment Drives Balancing With 2 DOF Positioner

Reflector

Boom

Elbow Hinge Actuator

Root Hinge Actuator

Feed Horns

TRW Astro Aerospace, PR-1059

OSIRIS Antenna Geometry
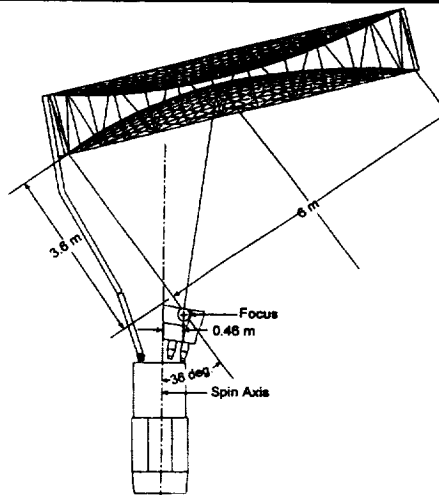
Focus
0.46 m

-36 deg

Spin Axis

6-Meter AstroMesh™ Reflector
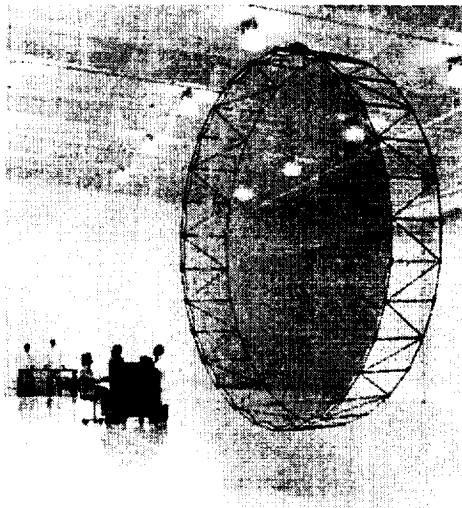
AstroMesh is a patented design (TRW Astro Aerospace (U.S. Patent No. 5,680,145)

TRW Astro Aerospace, PR-1059

OSIRIS Stowed Configuration

- Taurus launch vehicle
- Coriolis bus shown
  - Simple spinner would be smaller
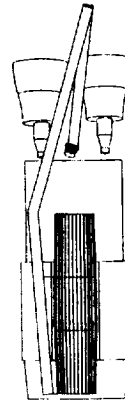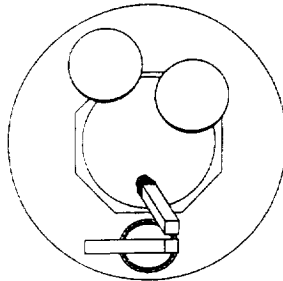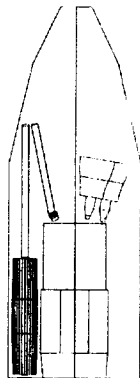
AstroMesh is a patented design of RW Astro Aerospace (U.S. Patent No. 5,680,145)

OSIRIS Deployment Sequence

TRW

Astromesh is a patented design of TRW Astro Aerospace (U.S. Patent No. 5,680,145).

Mass Breakdown

TRW
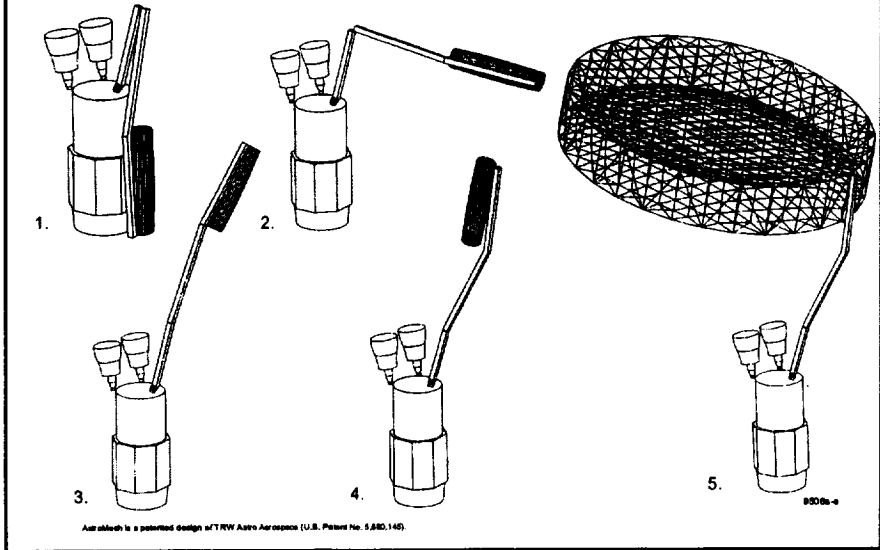
	Kg
Reflector	15.1
Boom (subtotal)	23.7
Struts	(12.2)
Actuators	(5.0)
Deployment Drive	(2.7)
Balance Mass	(4.7)
Feedthroughs	8.4
Radiometer and Radar Electronics	23.0
Total Spun Mass	71.2
Tie-downs	5.9

- 15 percent contingency added

Astromesh is a patented design of TRW Astro Aerospace (U.S. Patent No. 5,680,145).

TRW Astro Aerospace, PR-1059

First Five Vibration Modes

TRW
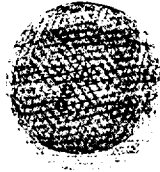
Mode = 1   0.89 Hz   Mode = 2   1.0 Hz   Mode = 3   1.9 Hz

Mode = 4   2.6 Hz   Mode = 5   5.9 Hz

Astromesh is a patented design of TRW Astro Aerospace (U.S. Patent No. 5,680,145)

TRW Astro Aerospace, PR-1059

Quasi-Static Deflection

TRW

- From centripetal acceleration
- 6 rpm = 0.628 Rad/sec
- 4 mm at far end of major axis
  - Would be corrected by
    the boom design

4 mm
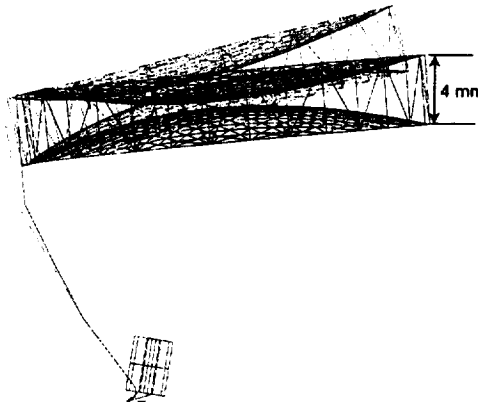
Astromesh is a patented design of TRW Astro Aerospace (U.S. Patent No. 5,680,145)

Conclusions

TRW

- IIP Preliminary antenna design is promising

  - Stiff

  - Balanced

    - 2 DOF balance mass trim actuator required

  - No problems with pointing or stability on stable spun platform/bus

- Spacecraft-Level Analytical results are required to complete the evaluation

APPENDIX II.

OSIRIS TECHNICAL SUMMARY,
CONFIGURATION DRAWINGS, AND
ATTITUDE CONTROL SUMMARY

(Spectrum Astro)

SPECTRUMASTRO

OSIRIS

TECHNICAL SUMMARY

CONFIGURATION DRAWINGS

ATTITUDE CONTROL SUMMARY

This chart provides a top-level summary of our OSIRIS spacecraft design. The mission is designed for a 3-year life requirement with a goal of 5 years. The OSIRIS nominal orbit is 600 km circular sun-synchronous with a 6 am ascending node local time (ANLT). Launch is assumed to take place in mid-2004.

Our attitude control configuration is a wheel-based zero-momentum bias (ZMB) system. Star trackers are used for attitude determination. Attitude control and knowledge capability is 0.05 degrees (3-axis 3σ). The attitude stability is estimated at 0.05 degrees over an interval of 0.71 seconds. Magnetic torquers and a three-axis magnetometer are used for momentum management (thrusters can also be used). The propulsion system is a simple hydrazine blowdown system consisting of a single 22-inch spherical titanium tank with four 5N thrusters and four 1N thrusters. The system has a propellant capacity of 68 kg. The propulsion system is used primarily for insertion error correction and orbit maintenance (drag make-up).

The electrical power system consists of a single-wing solar array, batteries, and power control electronics. Constructed of three panels, the deployed fixed array can generate 605 W at EOL. Two 23 Ahr common pressure vessel (CPV) nickel hydrogen batteries provide energy storage.

The total payload mass is estimated at 218.3 kg (including the spin table) and the bus dry mass is 325.9 kg (which includes 11.9 kg of growth contingency). The propellant load is 29.9 kg resulting in a total launch mass of 586.2 kg. A Taurus 2210 launch vehicle provides a launch capability of 680 kg to the OSIRIS orbit.

The structure is fabricated using aluminum honeycomb panels in a design that is essentially unchanged from Coriolis. The C&DH is Spectrum's standard VME architecture using the RAD6000 processor. Due to the low data volume specified, mass memory is provided by a single 2 Gbit memory board. The S-band telecom subsystem provides STDN downlink at a 2 Mbps rate with uplink at 2 kbps. It is envisioned that there would nominally be two to three contacts per day with the ground station.

1154-EB-R21498

Tech Sum.ppt

**OSIRIS SPACECRAFT CONFIGURATION
(FULL REDUNDANCY)**

OSIRIS

SPECTRUMASTRO

Mission
- Support OSIRIS Requirements & Reliably Return Data
- 3-Year Mission Lifetime
- 600 km Sun Sync Orbit (6am / 6pm nodal crossing)
- Launch Mid-2004

Attitude Control
- 3-Axis Stabilized, ZMB
- <±0.05 deg Control (3σ)
- <±0.05 deg Knowledge (3σ)
- Stability <0.05 deg/0.71 sec
- Autogenerated Flight Software

Propulsion
- Hydrazine 2:1 Blowdown System
- One 22-inch Spherical Tank
- Four 5 N Thrusters and Four 1N Thrusters
- 68 kg Propellant Capacity

Observatory Mass

Payload	117.4 kg
Spin Table	100.9 kg
S/C Bus	325.9 kg (dry)
Uncertainty (RSS)	12.1 kg
Propellant	29.9 kg
Observatory	586.2 kg

Electrical Power
- Three Panel Deployable Fixed Single-Wing GaAs Solar Array
- 605 W Solar Array Output at EOL
- 23 Ahr Nickel-Hydrogen Batteries
- Unreg 28 V ± 6 V Power Bus

Launch Vehicle
- Taurus 2210 (92-inch Fairing)
- 38" Marmon Band Sep System

Structure & Thermal
- Aluminum Honeycomb Design
- Cold-biased Thermal with MLI, Heaters, & Passive Radiators

Command & Data Handling
- VME Architecture
- R6000 CPU Operating at 20 MIPs
- 2 Gbit Mass Memory
- Standard Interfaces (1553, RS-432)
- C++ Flight Software

Telecommunications
- STDN Downlink at 2 Mbps (S-band)
- STDN Uplink at 2 kbps (S-band)
- CCSDS Protocols
- Nominally Two Contacts Per Day

1154-EB-R21498

Tech Sum.ppt

B-4

This is a list of the initial OSIRIS requirements provided by JPL for the OSIRIS study. Critical parameters for the spacecraft design are the orbit (600 km, sun sync, 6 am / 6 pm), pointing control and knowledge (1.3 and 0.· degrees 3σ respectively), payload data rate (25 kbps), launch vehicle (Taurus-class), mission duration (3 years).

Radiometer frequencies	1.41 and 2.69 GHz
Radiometer polarizations	H, V; (1.4 GHz polarimetric)
Radar frequency	1.26 GHz
Radar polarizations	VV, HH, VH, HV
Antenna type	Off-set fed, parabolic, deployable, mesh reflector
Aperture diameter	6 m
Nadir offset angle	36 degrees
Number of feedhorns	2 (each L/S band, V/H polarization)
Beamwidths	2.6 degrees (approximately equal in all channels)
Antenna gain	35 dB
Beam efficiency	>90%
Cross-polarization	< -18 dB
Orbit type	Polar, sun synchronous, 6 am / 6 pm
Altitude	600 km
Spatial resolution	35 x 45 km
Swath width	900 km
Rotation rate	6 rpm
Global coverage	2-3 days
Pointing control/knowledge	1.3 degrees / 0.1 degrees (3 sigma)
Radiometer precision/stability	0.2 K
Radar precision/stability	0.2 dB
Data rate	25 kbps
Launch vehicle	Taurus-class
Mission duration	3 years

This chart lists the modifications made to our SA-200HP catalog design that are specific to OSIRIS. The point of departure is the fully redundant Option 1 variant of the SA-200HP (which is essentially the Coriolis design in terms of avionics).

The catalog structure has been replaced with the Coriolis structure given the high degree of similarity between that mission and OSIRIS. There is a minor mod to the Coriolis structure for compatibility with the 38-inch Taurus separation system. There is no change to the mechanisms (now that the spin table is provided as part of the payload).

There are four changes to the ADCS. The first is the replacement of the ROSI Star Tracker with the Ball CT-633. This minimizes changes to the Coriolis configuration since it also uses the Ball tracker. Second, the fine sun sensor assembly (FSSA) of the catalog bus is deleted as it is not required for this mission. Third, the four Ithaco B-wheels in the catalog design are replaced with smaller Ithaco A-wheels. This is also to preserve as much of the Coriolis design as possible and the larger wheels are not required. Finally, the last change is the swap out of the redundant SIRUs with a lower cost set of two Litton LN-200 fiber optic gyros. The gyros are used primarily during maneuvers and the high accuracy SIRUs are not required in this application. The LN-200 gyros offer considerable cost savings and are also used in the Coriolis design.

There are no changes to the catalog propulsion system design (which is essentially the Coriolis design).

The 80 Mbps X-band downlink of the catalog design is deleted for OSIRIS since the data volume is quite low (25 kbps continuous which implies just 2.1 Gbits per day). The standard 2 Mbps S-band downlink is more than sufficient to downlink all of the instrument data in two or three contacts per day.

The C&DH system has three relatively minor modifications. First, the Gimbal Drive Electronics (GDE) board is not need since the solar arrays and antennas are all fixed (no gimbals). So the GDE board of the catalog design is deleted. Second, the Payload and Attitude Control Interface (PACI) board may require a minor modification to control the spin table (this is TBD depending on whether this function is performed by the payload processor or the spacecraft bus). Finally, given the low OSIRIS data rate, the 100 Gbit Solid State Recorder (SSR) of the catalog design is deleted. It is replaced by a 2 Gbit Solid State Memory (SSM) board that is contained within the VME card cage. When combined with the 1 Gbit DRAM located on the CPU board, there is ample memory available for all instrument science and spacecraft state-of-health (SOH) telemetry.

The power system is modified by the replacement of the catalog biaxial gimballed solar array wings with a single 3-panel wing similar to the Coriolis design. However, the cells are upgraded to triple junction GaAs to provide increased power capability for the same available surface area (the Coriolis array uses double junction GaAs; the 200HP catalog design uses triple junction GaAs cells). The biaxial solar array gimbals are deleted. The redundant 50 Ahr single pressure vessel (SPV) batteries are downsized to 23 Ahr common pressure vessel (CPV) versions to reduce mass.

The catalog bus assumed integration and test at commercial (or government) facilities. With the planned completion of Spectrum's new Factory of the Future (FoF) in March 2002, such integration and environmental test activities will now take place in-house resulting in considerable cost savings.

B-6

ATTITUDE DETERMINATION & CONTROL SUBSYSTEM

OSIRIS

The attitude determination and control subsystem (ADCS) is a zero-momentum-bias (ZMB) configuration that uses four reaction wheels for control and stability. The four wheels are oriented in a tetrahedral configuration such that any single wheel can fail without impact to the overall ADCS performance. The primary disturbance torques are expected to be residual torque errors from the spin table (a large wheel is assumed to be included in the payload for momentum compensation) and aerotorques due to the solar array configuration (which causes a cp-cg offset).

Wheel momentum management is performed using magnetic torque rods and a magnetometer. The torque rods are autonomously fired (typically for 20 minutes every orbit or two) to unload the wheels. Thrusters can also be used for momentum management. A star tracker provides attitude determination. The gyros are only used during acquisition, delta V maneuvers, and other non-standard operations. This approach minimizes power and increases ADCS reliability. Coarse sun sensors are used for initial acquisition. The GPS receiver provides real-time onboard ephemeris knowledge to better than 100m accuracy. All of the ADCS software exists from the Coriolis mission which minimizes both risk and cost. In addition, the 0.05 degree (3-axis, 3σ) performance estimate is conservative as Coriolis simulations indicate much better performance. However, such improved performance is not required for OSIRIS.

ATTITUDE DETERMINATION & CONTROL SUBSYSTEM

OSIRIS

- ZMB Architecture Using 4 A-size Wheels For Redundancy (4:3) And Control Of Disturbances (Residual Spin Table Momentum, Unbalanced Torques Due to Single-Wing Array)

- Magnetic Wheel Momentum Control Using Torqrod Actuators and Magnetometer Field Sensing

- Star Tracker For Attitude Determination (Nominally Operate In Gyroless Mode)

- Fiber Optic Gyro (IFOG) Used for Rate Determination Only During Maneuvers To Reduce Power and Prolong Gyro Lifetime

- Coarse Sun Sensors Used for Acquisition and Safe Mode

- 100-m Accuracy Ephemeris and Microsecond-Precision Time Obtained Via GPS

- Attitude Control Accuracy Significantly Better Than 0.05 Deg Per Axis Provides Large Control Margin

- Attitude Knowledge Accuracy Significantly Better Than 0.05 Deg Per Axis Provides Large Knowledge Margin

B-7

The telecom subsystem is very simple as it consists only of redundant transponders and two S-band patch antennas. The science data is downlinked at a 2 Mbps rate using direct modulation of the carrier. S/C state-of-health (SOH) telemetry is downlinked at a 64 kbps rate using a subcarrier. Both real-time and stored SOH data are downlinked simultaneously. The uplink is standard 2 kbps S-band. All links are CCSDS compatible.

The two antennas are combined to provide full omni receive capability in the event of loss of attitude (or for sun pointing safe mode).

The science data downlink time is 7.2 minutes per contact assuming an instrument data rate of 25 kbps, three contacts per day, and 20% CCSDS overhead. Link margins exceed 3 dB at 5 degree elevation angle assuming a typical 11m ground station.

- **Redundant STDN Transponders From Core**
    - **Science Data:** 2 Mbps Downlink
    - **SOH Telemetry:** 64 kbps
    - **Commands:** 2 kbps Uplink
- **Full Omni Coverage For Safe Hold (If Loss of Attitude)**
- **Science Data Downlink Time Would Be 7.2 min Per Contact (3 Contacts/Day With 20% Overhead)**
- **Link Margins Greater Than 3 dB Even At 5 deg Minimum Elevation (Assuming 11m GS)**

PROPULSION SIZING ASSUMPTIONS   *OSIRIS*

This chart lists the assumptions that were made in the propulsion system sizing trade for OSIRIS. A five-year maximum mission life was assumed (consistent with the three year mission life requirement and five year mission life goal). Launch was assumed to occur on 1 July 2004 on a Taurus 2210 launch vehicle. The launch date is important for solar activity and the launch vehicle type determines the required insertion error correction delta V. Note that the Taurus capability to the 600 km sun synchronous OSIRIS orbit is given as 680 kg in the Taurus User's Guide. However, the NASA guideline stated in the NAS10-99005 SELVS document is only 659 kg. It should be noted that ESSP bidders may be constrained to the NASA guidelines.

The initial S/C mass is estimated to be 586 kg (after separation but before correction of insertion errors). The average S/C projected area (relative to the velocity vector) is estimated at 8.0 m^2. This is very conservative as it basically assumes a solid OSIRIS antenna (in reality, it is a mesh antenna providing much less area for drag). The S/C drag coefficient is assumed to be 2.2 (slightly conservative as 2.0 is typical).

The latest NASA MSFC solar activity predictions were used and 2 sigma high solar activity was assumed throughout the mission. Since solar max is projected to occur in 2011, most of the OSIRIS mission will take place near the time of solar min. The worst case low injection is assumed. For Taurus, this is -10 km perigee and -50 km apogee with an inclination error of -0.15 degrees.

Orbit maintenance burns are assumed to be performed as often as necessary (on the order of once per week). It is assumed that altitude is actively maintained but that inclination is permitted to drift (I.e., inclination maintenance burns are not performed). Inclination drifts over time due to solar perturbations. The need for inclination maintenance depends on the nature of the science mission and the desire to maintain an exact repeating ground trace. The propulsion system has an effective Isp of 210 seconds after all system losses are included (e.g., thruster misalignment, plume impingement, gravity losses, etc.). There is a 10% growth contingency included on the propellant estimate.

The resulting required propellant load is 29.9 kg for a 5 year mission (including 0.45 kg of pressurant).

PROPULSION SIZING ASSUMPTIONS   *OSIRIS*

- 5 Year Mission Life (for Consumables)
- Launch 1 July 2004 on Taurus 2210
- Taurus Capability Is Only 680 kg (Per Taurus User's Guide; NASA Number Is 659 kg)
- Orbit Altitude Is 600 km Sun Synchronous
- Initial S/C Mass Approximately 586 kg
- Average S/C Projected Area Is 8.0 m^2 (Dominated By Payload; This Is Conservative)
- S/C Drag Coefficient Is 2.2
- 2σ High Solar Activity (F10.7 Cm Solar Flux) Assumed Throughout Mission
- Solar Max Occurs In January 2011 (Mission Takes Places Near Solar Min)
- 3σ Low Taurus Worst Case Injection Assumed
    (-10 km Perigee, -50 km Apogee, -0.15 Deg Inclination Based on Most Recent Data)
- Orbit Maintenance Burns Performed As Often As Necessary
- Altitude Maintained As Required, Inclination Allowed to Drift
- Propulsion System Effective Isp Is 210 sec
- 10% Propellant Contingency Included in Propellant Estimates
- Propellant Load of 29.9 kg Required (Sized For Five Year Mission Goal & Includes Pressurant)

PROPULSION SIZING

OSIRIS

The ΔV required for insertion error correction and orbit maintenance is shown in the table. Orbit maintenance is broken out in 6-month intervals. After the initial insertion error correction, inclination is allowed to drift. For each phase, the initial and final spacecraft mass is reported along with the mass of the propellant.

The plot at bottom is a bar chart showing how the delta V varies over the mission life. Delta V is broken out into altitude and inclination correction/maintenance. After the insertion error correction, very little propellant is required for orbit maintenance over the first three years of the mission (up through solar min). Then the orbit maintenance propellant begins increasing as indicated in Year 4 and beyond.

The altitude and inclination error correction ΔVs are 37 and 26 m/s respectively for the worst-case Taurus injection. Since we are injecting directly into the final orbit, there is no orbit-raising ΔV. Inclination and altitude are shown over the 5 years of the mission. Inclination is not actively maintained. Altitude maintenance is required to make up for altitude lost due to drag. The ΔV required varies with solar activity peaking at just under 12 m/s per 6 month period at the end of the mission life. We carry a 10% ΔV contingency across the board for propulsion system sizing.

Note that a targeted de-orbit burn may be required to satisfy NASA debris policy. A debris assessment has not yet been performed and the propulsion system has not been sized for such a de-orbit maneuver.

PROPULSION SIZING

OSIRIS

Mission Phase	Alt ΔV (m/s)	Incl ΔV (m/s)	Initial Mass (kg)	Final Mass (kg)	Propellant (kg)	
Insertion Error	37.09	26.00	586.50	568.82	17.68	
Year 0.5	2.03	0.00	568.82	568.26	0.56	
Year 1	1.56	0.00	568.26	567.82	0.43	
Year 1.5	1.30	0.00	567.82	567.47	0.36	
Year 2	1.16	0.00	567.47	567.14	0.32	
Year 2.5	1.08	0.00	567.14	566.85	0.30	Solar Min
Year 3	1.22	0.00	566.85	566.51	0.34	
Year 3.5	1.88	0.00	566.51	566.00	0.52	
Year 4	3.53	0.00	566.00	565.03	0.97	
Year 4.5	7.36	0.00	565.03	563.01	2.02	
Year 5	12.28	0.00	563.01	559.67	3.34	
10% Contingency	9.86	0.00	566.00	583.35	2.64	
Pressurant	—	—	563.35	562.90	0.45	
Totals	88.17	26.00			28.93	

B-10
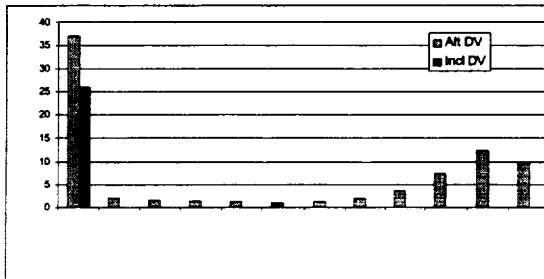
Presented in this table are the key system performance margins. There are good system design margins across the board. The total launch mass must be less than the launch vehicle capability of 680 kg (Taurus 2210). Our estimated mass is 586 kg yielding a total (or wet) mass margin of 16%. The required spacecraft mission life is 5 years with a reliability of 0.913.

System power and battery margins are 23% and 44%, respectively, assuming worst-case, end-of-life conditions. Attitude control is 13 times better than the requirement and attitude knowledge is twice as good as required.

0.72 Gbits of data storage is required and we have provided >2 Gbits (BOL) exceeding the requirement by a factor of 2.8. The science data transfer rate is 25 kbps and the 1553 I/F can handle in excess of 300 kbps provided a margin of a factor of 12. Link margin is over 3 dB even under worst case conditions (5 deg elevation angle). The total radiation dose at 100 mil equivalent aluminum shielding is 7.2 krad. Our softest component (DRAM) is radiation tolerant to 26 krad, providing at least a 3.7X design margin.

Parameter	Margin	Requirement	Capability
Mass (Taurus Direct 600 km)	16% [1]	< 680 kg	586 kg
Mission Reliability (@ 3 Yrs)	N/A	Not Specified	0.913 [2]
Power	23% [*]	< 605 W OAP	490 WOAP [3]
Battery	44%	< 16.0 A-hr	23 A-hr
Attitude Control	13X	< 1.3 deg	<0.1 deg (3σ)
Attitude Knowledge	2X	< 0.1 deg	<0.05 deg (3σ)
Memory	2.8X	0.72 Gbit [4]	2 Gbit
Science Data Transfer Rate	12X	25 kbps	>300 kbps
Link Margin STDN (2 Mbps)	N/A	N/A	3.0 dB [5]
Radiation Dose	3.7X	> 7.1 krad	≥ 26 krad

Notes:
[1] Includes S/C Bus Contingency
[2] Includes Spin Table Reliability
[3] For Worst-Case EOL at 3 Years
[4] For 8 Hours of Data Storage
[5] For 5 deg Elevation Angle

B-11

CONCLUSION

OSIRIS

The SA-200HP catalog bus was originally flown on Deep Space 1 (DS1). This was a deep space mission that was largely single string. Option 1 to the SA-200HP provides full system redundancy. This version is currently in development and production for Coriolis (Dec 01 launch) and Swift (Sep 03 launch). OSIRIS is extremely similar to Coriolis and the data presented here has attempted to maximize that similarity as the Windsat payload of Coriolis is very much like the OSIRIS payload.

Our design as configured provides high bus reliability at 5 years consistent with the mission life goal. This package provided details on the modifications between the SA-200HP Option 1 catalog bus and our OSIRIS design.

There are good systems margins in all areas although mass margin could use additional work. The design would need to be updated to reflect requirements for a future mission.

The high degree of similarity to previous and current Spectrum Astro spacecraft designs ensures that our OSIRIS design is a low risk approach. The performance, cost, and schedule of Coriolis is very well documented.

1154-EB-R21498   Tech Sum.ppt

SPECTRUMASTRO

CONCLUSION

OSIRIS

- A Coriolis-like Derivative of Our SA-200HP Catalog Bus Has Been Adapted For the OSIRIS Mission

- There Is High Degree of Similarity Between Coriolis Payload (Windsat) and OSIRIS Payload

- A Fully Redundant Vehicle With a Design Life of 5-years Was Provided

- Catalog Modifications Presented (Most Modifications Are To Get to Coriolis Configuration)

- There Are Good System Margins Across the Board; Mass Is Only Area of Concern at Present

- Need to Tailor This Design For Specific Future Mission

- This Is a Low Risk Approach (Technical, Schedule, Cost) Given Coriolis and DS1 Heritage

1154-EB-R21498   Tech Sum.ppt

The slide illustrates the observatory configuration. It includes the elements of the payload (antenna, boom, and feed horns), the spun platform and the spacecraft bus. Both the bus and payload elements are shown in the metallic color while the reddish-brown color illustrates the spun platform. The break in the spun platform marks the division between the stationary and rotating segments. The stowed payload CAD model is provided by TRW Astro while the spacecraft bus and spun platform were provided by Spectrum Astro. For the next phase, JPL will be providing the spun platform. The royal blue rectangles represent the deployed solar array.

For this exercise, the spun platform is designed around the Bearing and Power Transfer Assembly (BAPTA) from the Coriolis payload, WindSat. These BAPTA capabilities are a close match for the OSIRIS needs. The spun structure is of the same type as the bus, an all Aluminum frame and Aluminum honeycomb panels. For this configuration, the attitude control system bench that includes the Inertial Reference Units (2) and the Star Trackers (2) is placed in the spun platform. As an alternative, this bench could be placed on the bus.
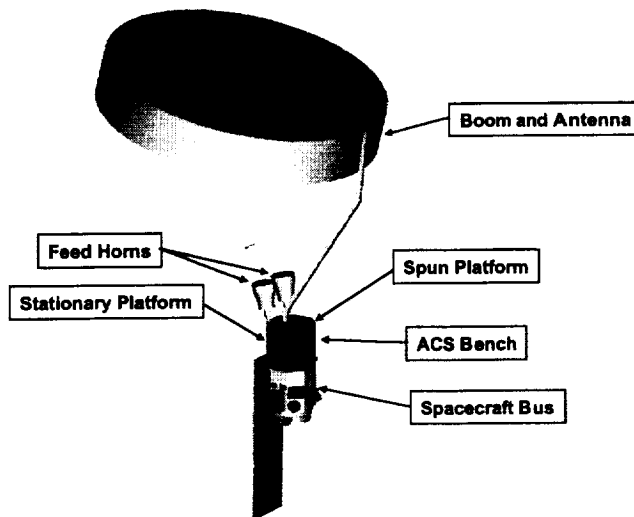
Boom and Antenna

Feed Horns

Stationary Platform

Spun Platform

ACS Bench

Spacecraft Bus

1154-EB-R21496   CONFIG DWGS.ppt

B-14

As indicated, the approximate size of the observatory is 6.1 meters by 11.3 meters. The spacecraft / launch vehicle separation plane is the reference for the vertical dimensions. The antenna / spun platform interface is at 2.37 meters and solar arrays hang down 2.41 meters. For illustration purposes, the subsequent slide shows the shaded images.

1154-EB-R21498   CONFIG DWGS.ppt
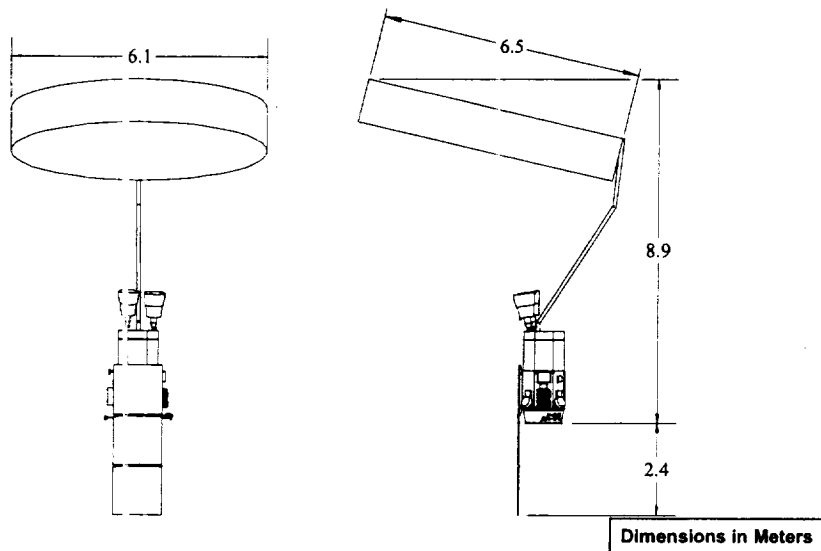
6.1

6.5

8.9

2.4

Dimensions in Meters

1154-EB-R21498   CONFIG DWGS.ppt

The picture is intended to display the stowed observatory inside the Taurus Launch Vehicle Fairing. Again, the bus, payload and spun platform are included. The antenna folds up on the side of the spacecraft as shown.

The top view displays the approximate radial dimensions of the observatory maximum extremities and the dynamic envelope of the launch vehicle fairing. The minimum fairing clearance is just under 5 cm. This provides more than adequate room for dynamic displacements. The boom to fairing clearance is just over 5.3 cm.

1154-EB-R21498

CONFIG DWGS.ppt

R 1.03

Fairing Envelope (Bottom Portion)

R 0.97

R 0.98

Minimum Boom to Fairing Clearance is 5.3 CM

3.90

2.37

1.50

1.35

1.27

1.27

Dimensions in Meters

1154-EB-R21498

CONFIG DWGS.ppt

STOWED MODEL

OSIRIS

SPECTRUMASTRO
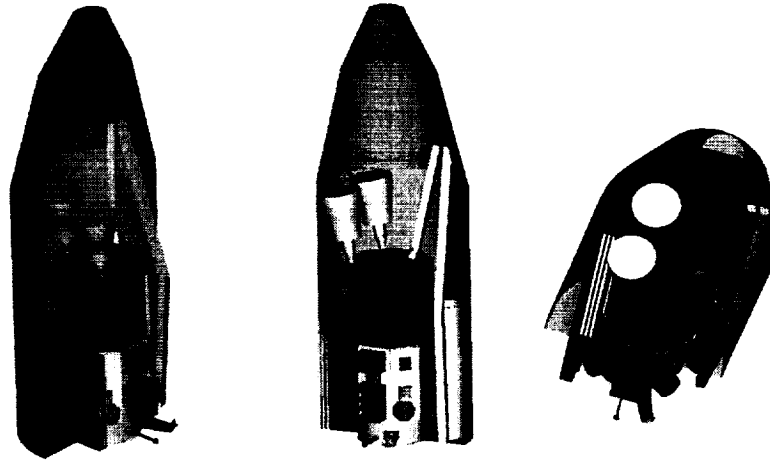
1154-EB-R21408

CONFIG DWGS.ppt

ACS STUDY - SUMMARY

OSIRIS

SPECTRUMASTRO

The Coriolis Bus ACS System Can Accommodate the OSIRIS Payload and Meet the Attitude Knowledge and Control Requirements

*   Current Equipment can be used, except for GPS Receiver Compatibility Issues with the Payload
*   Antenna Pointing Control Performance Is better than Requirement, could be Improved by Reconfiguring the Coriolis Thruster Layout
*   Antenna Pointing Knowledge Is Better than Requirement, Depending on Platform Imbalance Effects

1154-EB-R21498   ACS STUDY.ppt

ACS STUDY - AREAS OF ANALYSIS

OSIRIS

SPECTRUMASTRO

The Following Analysis / Activities Were Included in This Study Effort:

*   ACS Equipment Sizing, Field-of-View Analysis and Compatibility Assessment
*   Estimate of Mass Properties
*   Estimate of Environmental Torques
*   Estimate of Attitude Determination Performance
*   Estimate of Rigid Body Attitude Control Performance
*   Torque Rod Sizing / Momentum Storage Sizing
*   Estimate of Disturbance Forces and Torques
*   Estimate of Rigid / Flex Body Pointing Errors

1154-EB-R21498   ACS STUDY.ppt

Based on This Analysis, the Spectrum Astro Coriolis Bus Can Meet the Attitude Control Requirements of the OSIRIS Payload

The Following Items Represent Areas of Concern Which Should Be Investigated Further:

- **GPS Receiver Operation (Satellite Visibility and Payload Interference)**

- **Star Trackers Will Require Larger Light Shade to Reduce Sun-exclusion Angle to 30 Degrees**

- **Current Coriolis Thruster Layout Could Be Modified to Reduce Disturbance Torques From Stationkeeping Burns**

- **Payload Platform Imbalance Effects Will Limit Overall Pointing Knowledge at the Antenna Boresight - Especially Principal Axis Misalignment. Recommend Managing the Misalignment to Below 0.03 deg**

B-20

APPENDIX III.

TECHNOLOGY READINESS LEVELS (TRLs)

APPENDIX III. TECHNOLOGY READINESS LEVELS (TRLs)

System Test, Launch & Operations	TRL 9	Actual system "flight proven" through successful mission operations
System/Subsystem Development	TRL 8	Actual system completed and "flight qualified" through test and demonstration (Ground or Flight)
	TRL 7	System prototype demonstration in a space environment
Technology Demonstration		System/subsystem model or prototype demonstration in a relevant environment (Ground or Space)
Technology Development		Component and/or breadboard validation in relevant environment
	TRL 4	Component and/or breadboard validation in laboratory environment
Research to Prove Feasibility	TRL 3	Analytical and experimental critical function and/or characteristic proof-of-concept
Basic Technology Research	TRL 2	Technology concept and/or application formulated
	TRL 1	Basic principles observed and reported

APPENDIX IV.

ACRONYMS

APPENDIX V. ACRONYMS

A/D	Analog/Digital
ACS	Attitude Control System
ADC	Analog to Digital Converter
ADCS	Attitude Determination and Control System
ADEOS-II	Advanced Earth Observation Satellite-II
ALU	Arithmetic Logic Unit
AMSR	Advanced Microwave Scanning Radiometer
ARTP	Advanced Radar Technology Program
C&DH	Command & Data Handling
C&T	Control & Timing
CAD	Computer Aided Design
CDTS	Command, Data, Timing Subsystem
CMOS	Complementary Metal Oxide Semiconductor
CTE	Coefficient of Thermal Expansion
DCG	Digital Chirp Generator
DDS	Direct Digital Synthesizer
DMSP	Defense Meteorological Satellite Program
DUT	Device Under Test
ECMWF	European Center for Medium-range Weather Forecasting
EM	Electromagnetic
EMI	Electromagnetic Interference
ENSO	El Nino Southern Oscillation
EOS	Earth Observing System
ESE	Earth Science Enterprise
ESTO	Earth Science Technology Office
FEM	Finite Element Model
FPGA	Field Programmable Gate Array
GA	Genetic Algorithm
GPS	Global Positioning System
HPBW	Half Power Beam Width
IF	Intermediate Frequency
IIP	Instrument Incubator Program
IR	Infrared
JPL	Jet Propulsion Laboratory
LaRC	Langley Research Center
LFMR	Low Frequency Microwave Radiometer
LO	Local Oscillator
MBARI	Monterey Bay Aquarium Research Institute

MEMS	Materials Emissivity Measurement System
MMIC	Monolithic Microwave Integrated Circuit
MO	Master Oscillator
NASA	National Aeronautics and Space Administration
NCAR	National Center for Atmospheric Research
NPOESS	National Polar Orbiting Environmental Satellite System
NRL	Naval Research Laboratory
NROSS	Navy Remote Observing Satellite System
NSCAT	NASA Scatterometer
OPI	Openings Per Inch
OSIRIS	Ocean salinity Soil moisture Integrated Radiometer-radar Imaging System
PEC	Perfect Electric Semiconductor
PIU	Payload Interface Unit
PO	Physical Optics
PRF	Pulse Repetition Frequency
RF	Radio Frequency
RFES	RF Electronics Subsystem
RFI	Radio Frequency Interference
RFS	Radio Frequency Subsystem
RMS	Root Mean Squared
RSDO	Rapid Spacecraft Deployment Office
RSS	Root Sum Squared
SA	Spectrum Astro
SAIC	Science Applications International Corporation
SMA	Sub Miniature A
S&EG	Space & Electronics Group
SMMR	Scanning Multichannel Microwave Radiometer
SNR	Signal to Noise Ratio
SPDT	Single Pole Double Throw
SSM/I	Special Sensor Microwave/Imager
SSPA	Solid State Power Amplifier
SSR	Solid State Recorder
SSS	Sea Surface Salinity
SST	Sea Surface Temperature
T/R	Transmit/Receive
TAA	TRW Astro Aerospace
TDRSS	Tracking and Data Relay Satellite System
TEC	Thermal Electric Cooler
TEM	Transverse Electromagnetic
TM	Transverse Magnetic

TMI	TRMM Microwave Imager
TOPEX	Topography Experiment
TRL	Technology Readiness Level
TRMM	Tropical Rainfall Measuring Mission
UCLA	University of California Los Angeles
USN	Universal Space Network
VME	Versa Module Europa
VNA	Vector Network Analyzer
VSWR	Voltage Standing Wave Ratio

REPORT DOCUMENTATION PAGE

Form Approved
OMB No. 0704-0188

1. AGENCY USE ONLY (Leave blank)	2. REPORT DATE September 2001	3. REPORT TYPE AND DATES COVERED JPL Publication

4. TITLE AND SUBTITLE

Spaceborne Microwave Instrument for High Resolution Remote Sensing of the Earth's Surface Using a Large-Aperture Mesh Antenna

5. FUNDING NUMBERS

C.- NAS7-1407

6. AUTHOR(S)

E. Njoku, W. Wilson, S. Yueh, R. Freeland, R. Helms, et al.

7. PERFORMING ORGANIZATION NAME(S) AND ADDRESS(ES)

Jet Propulsion Laboratory
California Institute of Technology
4800 Oak Grove Drive
Pasadena, CA 91109-8099

8. PERFORMING ORGANIZATION REPORT NUMBER

JPL Publication 01-09

9. SPONSORING / MONITORING AGENCY NAME(S) AND ADDRESS(ES)

National Aeronautics and Space Administration
Washington, DC 20546-0001

10. SPONSORING / MONITORING AGENCY REPORT NUMBER

11. SUPPLEMENTARY NOTES

12a. DISTRIBUTION / AVAILABILITY STATEMENT

SUBJECT CATEGORY: 19   DISTRIBUTION: Nonstandard

AVAILABILITY: NASA CASI (301) 621-0390

12b. DISTRIBUTION CODE

13. ABSTRACT (Maximum 200 words)

This report describes a two-year study of a large-aperture, lightweight, deployable mesh antenna system for radiometer and radar remote sensing of the Earth from space. The study focused specifically on an instrument to measure ocean salinity and soil moisture. Measurements of ocean salinity and soil moisture are of critical importance in improving knowledge and prediction of key ocean and land surface processes, but are not currently obtainable from space. A mission using this instrument would be the first demonstration of deployable mesh antenna technology for remote sensing and could lead to potential applications in other remote sensing disciplines that require high spatial resolution measurements. The study concept features a rotating 6-m-diameter deployable-mesh antenna, with radiometer and radar sensors, to measure microwave emission and backscatter from the Earth's surface. The sensors operate at L and S bands, with multiple polarizations and a constant look angle, scanning across a wide swath. The study included detailed analyses of science requirements, reflector and feedhorn design and performance, microwave emissivity measurements of mesh samples, design and test of lightweight radar electronics, launch vehicle accommodations, rotational dynamics simulations, and an analysis of attitude control issues associated with the antenna and spacecraft, The goal of the study was to advance the technology readiness of the overall concep to a level appropriate for an Earth science emission.

14. SUBJECT TERMS

remote sensing, mesh antenna, radiometer, radar   ocean salinity, soil moisture Earth science

15. NUMBER OF PAGES

170

16. PRICE CODE

17. SECURITY CLASSIFICATION OF REPORT	18. SECURITY CLASSIFICATION OF THIS PAGE	19. SECURITY CLASSIFICATION OF ABSTRACT	20. LIMITATION OF ABSTRACT
Unclassified	Unclassified	Unclassified	Unlimited